PREDICTIONS OF INDUCED BRITTLE FAILURE IN CONVENTIONAL AND UNCONVENTIONAL RESERVOIRS

A Dissertation

by

ROBERT CHARLES CHOENS II

Submitted to the Office of Graduate and Professional Studies of
Texas A&M University
in partial fulfillment of the requirements for the degree of

DOCTOR OF PHILOSOPHY

Chair of Committee,	Frederick Chester
Committee Members,	Benchun Duan
	Richard Gibson
	Andrew Hajash
	Marcelo Sanchez
Head of Department,	Michael Pope

December 2015

Major Subject: Geophysics

ABSTRACT

Knowledge of the mechanical behavior of rocks is necessary to predict the response of reservoirs and basins to naturogenic and anthropogenic changes. Applications with significant economic and environmental impacts include petroleum reservoirs, geothermal systems, CO_2 sequestration systems and fault behavior. This work addresses two types of poorly understood brittle failure. The behavior of rocks in tension and low mean stresses applied to hydraulic fracture in the subsurface, and the behavior of granular, porous materials in chemically reactive environments over long time periods applied to porosity development in sedimentary basins and petroleum withdrawal or CO_2 injections in reservoirs.

The behavior of an induced hydraulic fracture is difficult to predict a priori due to great uncertainty in fracture geometry, kinematics, and induced damage as a function of stress state. Previous experiments have shown that the conventional failure criteria for tensile and low mean stresses are inadequate. Experiments were conducted on four rock types with different mechanical properties and mineralogic compositions: Berea sandstone, Carrara marble, Indiana limestone, and Kansas chalk. The results are used to develop a universal failure criterion for low mean stress states occurring in hydraulic fracturing and other high-fluid pressure regimes. The criterion defines mechanical properties as well as fracture characteristics as a function of stress state. The failure criterion may be easily applied to all rock types as it scales with the uniaxial extensional strength of the rock.

The consolidation of porous, granular materials occurs at strain rates as low as 10^{-9} and 10^{-15} seconds^{-1} for reservoirs and sedimentary basins. Previous work has shown fluid saturated granular materials, such as quartz sand in water, consolidate with time by subcritical crack processes. Consolidation experiments and creep experiments were conducted on quartz sand to test the applicability of soil mechanics principles to time-dependent consolidation of granular porous rock. Results show that the effect of strain rate and temperature can be used in the framework of parallel lines of consolidation to predict the critical pressure for crushing, P^*, for quartz sand at in situ conditions. Accordingly, consolidation of rocks can be predicted because shear-enhanced compaction depends on P^*.

DEDICATION

I dedicate this dissertation to the loved ones in my life, my parents, my girlfriend/fiancée/wife Megan, and our dog Ruby. Their love, support, and patience (I don't think I can stress patience enough) has sustained me during this long journey.

ACKNOWLEDGEMENTS

I would like to thank my committee chair, Dr. Chester, for his guidance and support throughout the course of this research. I would also like to thank my committee members, Dr. Duan, Dr. Gibson, Dr. Hajash, and Dr. Sanchez, for their contributions to this dissertation. I would also like to acknowledge former committee members for their contributions: Dr. Ghassemi, and Dr. Biscontin.

I would like to thank Clayton Powell for his technical assistance in the laboratory during his tenure. Thanks also go to my friends and colleagues in the Center for Tectonophysics and the department faculty and staff of the department of Geology and Geophysics for making my time at Texas A&M University a great experience. I thank fellow Tectonophysists for stimulating conversations, whether over coffee or beer. Running long experiments can raise logistical problems, and I would like to acknowledge Margaret Smoot, Dr. Melodie French, and Dr. Hiroko Kitajima, and Dr. Caleb Holyoke for shouldering experiment babysitting duties and allowing me the freedom to travel as necessary. I would also like to thank Margaret Smoot and her mother for a guest room in times of need.

I would also like to acknowledge the previous work of former Center students, most of whom I have not had the opportunity to meet, for their hard work in developing techniques that made my path much easier. I have benefitted greatly from the fruits of their labor.

I would like to thank Dr. Nigel Higgs for recommending the Menterey and Willam, 1995 failure model.

I owe the ability to turn in a finished dissertation to the people and facilities of Sandia National Laboratories. The final two years of my Ph.D. was supported by the Sandia National Laboratories / Texas A&M University Excellence in Geosciences Fellowship, which, in addition to tuition and stipends, provided funds for experimental materials and access to Sandia Facilities. All of the dogbone experiments that I performed, two thirds of this dissertation, were performed during a series of internships at Sandia. I would like to acknowledge the people that made that possible: Marianne Walck, Eric Webb, Moo Lee, Frank Hansen, Steve Bauer, and any other in the management layers that I never met. I would also like the people in the lab that I worked with on a daily basis: my mentor, Steve Bauer, and the technologist who ran the experiments, Greg Flint. I am also indebted to the rest of the staff as well: Matt Ingraham, Scott Broome, Perry, and Mike.

TABLE OF CONTENTS

Page

LIST OF FIGURES

Page

LIST OF TABLES

Page

1. INTRODUCTION

The behavior of rocks at crustal conditions has large implications both economically and environmentally. Petroleum reservoirs in sedimentary basins will continue to dominate the energy landscape for the foreseeable future, and depleted petroleum reservoirs offer possible storage sites for excess CO_2 emissions. In additions, porous granular rocks and sediments act as aquifers for potable water. It is important to understand how porosity develops, both in basins during burial / diagenesis and in reservoirs during production / injection. Of increasing importance is the behavior of rocks in tension and low mean stresses. Beyond naturally occurring joints and fractures in sedimentary basins, induced tensile fractures in tight reservoir rocks opens key permeability pathways. Hydraulic fracturing has revolutionized petroleum exploration, and could significantly impact geothermal power production as well. The behavior of rocks and sediments are defined though laboratory experiments, which utilize homogeneous samples in simplified conditions and extrapolate to in situ conditions. If the experiments are too simple, then the resulting predictions of behavior will be incorrect. If the experiments are too difficult, then it might be too difficult to produce meaningful results. For porous, granular rocks, laboratory experiments do not accurately capture the time and temperature effects seen at in situ conditions. For the behavior of rocks in tension, there have been limited investigations at mixed states of stress seen in hydraulic fracture conditions.

In Section 2, we study the consolidation of porous, granular material under hydrothermal conditions. We report hydrostatic consolidation experiments on St. Peter sand conducted at a constant plastic volume strain rate for four different orders of magnitude of strain rate and four different temperatures. We also report secondary creep consolidation experiments conducted at three different creep stresses at elevated temperatures. The results from the experiments are compared to soil consolidation models to extrapolate results to in situ conditions.

In Sections 3 and 4, we investigate the behavior of rock in tension and low mean stresses. We report a series of triaxial extension experiment on Berea sandstone, Carrara marble, Indiana limestone, and Kansas chalk conducted across the tensile to shear transition. Section 3 focuses on the strength and fracture characteristics of the four different rock types and develops a more accurate failure envelope for the low mean stress regime. The results are applied to examples of naturally occurring and induced fractures to better understand the failure processes. Section 4 focuses on plasticity theory applied to results for Berea sandstone and Carrara marble. The experiments represent the first test of the theory in the tensile to shear transition for natural materials.

2. PREDICTING TIME DEPENDENT FAILURE IN POROUS, GRANULAR MATERIAL AT IN SITU CONDITIONS OF TEMPERATURE AND PRESSURE

2.1. Introduction

The deformation of porous granular material has broad application to the behavior of fault gouge [*F M Chester*, 1994; *Marone and Scholz*, 1989], burial and consolidation of sediments [*David et al.*, 1994; *Dewers and Hajash*, 1995; *Laubach et al.*, 2010; *Milliken and Laubach*, 2000; *Rutter and Wanten*, 2000; *van Noort et al.*, 2008], ground subsidence above reservoirs due to pore fluid withdrawal [*Hettema et al.*, 2000; *Morton et al.*, 2006; *Roberts*, 1964; *Zoback*, 2007], the stability of proppant injected into fractures associated with development of unconventional petroleum and geothermal reservoirs [*Milton-Tayler et al.*, 1992; *Raysoni and Weaver*, 2012], mass movements and landslides [*Katz and Aharonov*, 2006; *Ng and Dobry*, 1994], stability of foundations [*Mitchell and Soga*, 1976; *Terzaghi et al.*, 1996], and high velocity impacts [*Stöffler et al.*, 1975; *Yamamuro et al.*, 1996]. Observed behaviors reflect different deformation processes operating over different time scales, stress, and temperature conditions. Here, we present a methodology based on geotechnical principles of soil consolidation to better predict brittle deformation of porous quartz sand and sandstones at in situ conditions for both geologic and engineered loading.

Porous and granular soil, sediment, and rock differ from low porosity sedimentary and crystalline rocks in their potential for inelastic strain resulting from isostatic stress (i.e., effective confining pressure, P_e) [e.g., Brace, 1971; Wong et al,

1997]. Application of P_e to such materials can lead to consolidation by grain movement, rearrangement and improved packing. With sufficient isostatic stressing, porous material will fail by grain crushing, i.e., distributed grain cracking and sliding, porosity collapse, and communition. For isostatic loading, the macroscopic pressure that induces grain crushing is defined as the crushing strength, or critical pressure, P^*, of the material. The stress distribution at grain contacts leading to brittle failure is often described in the context of Hertzian contacts [*Zhang et al.*, 1990a]. Using models based on Hertzian theory for non-adhesive elastic contacts and comparisons of the model predictions to experiment data, P^* has been shown to be proportional to $(\phi R)^{-n}$, where ϕ is the initial porosity and R is the grain size [*Zhang et al.*, 1990a; *Zhang et al.*, 1990b]. In these models, larger grains have lower P^* values because the grains contain larger inherent flaws; higher porosities have lower P^* values because there are less grain contacts to spread the applied load [*Zhang et al.*, 1990a].

Inelastic, brittle failure of porous granular materials for non-isostatic stress states (e.g., *Pe* plus differential stress, $\Delta\sigma$) also is related to P^*. Specifically, the elliptical failure criterion (cap) that describes failure by shear-enhanced compaction, at combined deviatoric and high mean stresses, is anchored at P^* [*DiMaggio and Sandler*, 1971; *Karner et al.*, 2005; *Menendez et al.*, 1996; *Wong et al.*, 1997]. For cemented materials with contact adhesion, there is relatively little inelastic deformation at mean stress conditions less than P^* and at deviatoric stress conditions less than the cap for shear enhanced compaction. In contrast, for poorly cemented and poorly packed granular material, such as loose quartz sand, significant consolidation can occur at low stresses

below P^* by sliding and rotation of grains to achieve tighter packing arrangements [*Karner et al.*, 2003]. With increasing mean and deviatoric stress, the normal loads across grain contacts increase, progressively inhibiting slip of contacts. At even higher deviatoric and mean stresses at the cap, contact stresses lead to grain cracking and the initiation of shear enhanced compaction [*Karner et al.*, 2003; *Zhang et al.*, 1990a]. In this paper, deformation producing consolidation of material at mean stress below P^* and the cap is referred to as Regime 1 behavior, and the deformation producing by crushing at P^* and shear-enhanced compaction at the cap is referred to as Regime 2 behavior.

Although stress has primary control on brittle deformation in sand, much experimental work has shown that compaction of sand also depends on strain rate, temperature, and chemical environments [*F M Chester et al.*, 2007; *J S Chester et al.*, 2004; *Dewers and Hajash*, 1995; *Dove*, 1995; *Elias and Hajash*, 1992; *He et al.*, 2003; *He et al.*, 2013; *Karner et al.*, 2008; *Rutter and Wanten*, 2000]. The elliptical cap describing shear enhanced compaction collapses to lower stresses with a corresponding decreases in P^* at elevated temperatures in wet sand [*Dewers and Hajash*, 1995; *Karner et al.*, 2008] and sandstone [*Baud et al.*, 2000; *Wong and Baud*, 2012]. In addition, at stresses well below those of the cap, creep consolidation of sand is enhanced with increases in temperature and with increases in exposure to water. The increased creep rates are explained by the operation of thermally-activated, subcritical crack growth, as governed by water–silicate reactions at crack tips controlled by access of water [*Atkinson*, 1982; *F M Chester et al.*, 2007; *J S Chester et al.*, 2005; *Dove*, 1995; *Freiman*, 1984]. The fact that consolidation of quartz sandstones and sand in Regimes 1

and 2 depends on temperature, water and chemical environment, implies that the stress for consolidation and failure of these rocks also depends on strain rate. Thus, the values of P^* and the position of the cap for sandstones and sand in the crust are poorly determined by typical laboratory experiments that are conducted at room temperature, dry and by using relatively high strain rates.

It has long been recognized in geotechnical analysis of soil and sediment behaviors that consolidation is a function of stress and time [*Augustesen et al.*, 2004; *Bjerrum*, 1967; *Garlanger*, 1972; *Karig and Ask*, 2003; *Karig and Hou*, 1992; *Leonards and Deschamps*, 1995; *Leroueil*, 1996; *Leroueil et al.*, 1985; *Leroueil and Vaughan*, 1990; *Mitchell and Soga*, 1976]. The stress dependence is shown by 1D consolidation tests run at constant strain rate, for which strain is approximately linear with log stress. Time dependence is illustrated by secondary creep tests in which consolidation increases with time at constant stress. These observations are integrated in the Bjerrum plot [*Augustesen et al.*, 2004; *Bjerrum*, 1967; *Garlanger*, 1972; *Karig and Ask*, 2003; *Leroueil et al.*, 1985], which shows parallel consolidation curves representing consolidation at different strain rates (Figure 1). It is noted that secondary creep experiments have the effect of achieving strain at lower stress, effectively satisfying consolidation curves for lower strain rates. Upon resumption of loading the sample after secondary creep, the response is very stiff until the constant-rate consolidation curve is re-established [*Bjerrum*, 1967; *Karig and Ask*, 2003; *Leroueil et al.*, 1985]. The pseudo-elastic response associated with loading after creep is tertiary consolidation [*Augustesen et al.*, 2004; *Karig and Ask*, 2003; *Yilmaz et al.*, 2001].

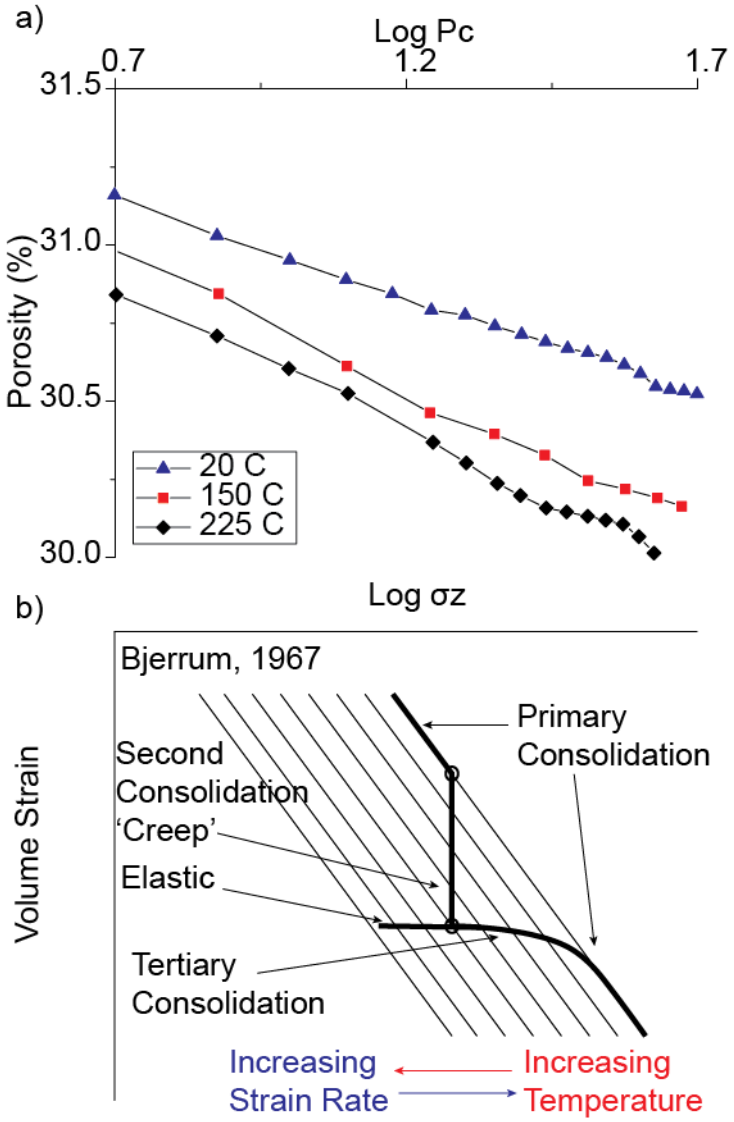

Figure 1. A comparison between plastic consolidation curves for St. Peters sand at different temperatures and a clay consolidation model by Bjerrum, 1967. a) Log confining pressure versus porosity for the plastic consolidation of St. Peters sand conducted at 20° C, blue triangles, 150° C, red triangles, and 225° C, black diamonds. b) Model for 1D consolidation of clay rich soils from Bjerrum, 1967, in log normal stress versus volume strain space.

Consolidation curves determined for quartz sand are nonlinear, unlike the linear curves for many soils [*Pestana and Whittle*, 1998]. However, the nonlinearity is largely due to the poro-elastic components of strain, which accounts for the majority of volume strain up to P^* [*Karner et al.*, 2003]. Elastic strain may be measured directly in experiments [*Karner et al.*, 2003], or determined via appropriate models based on Hertzian contact elasticity [*e.g., Gangi, 1978*]. The plastic component of strain is the difference between total strain and elastic strain, and it corresponds to irreversible porosity reduction due to grain rotation, grain cracking, porosity collapse, and grain comminution. For consolidation of quartz sand, the plastic strain curve is linear for Regime 1 and Regime 2, with the change in slope at P^* (Figure 2). As shown in Figure 1, for isostatic consolidation tests on wet sand at 20°, 150°, and 225° C, the plastic strain curves are approximately linear and parallel in log stress for Regime 1, consistent with the Bjerrum plot. Overall, the strain rate, temperature, and chemical effects observed for sand and documented by Karner et al., 2008, Chester et al., 2004, Chester et al., 2007, and He et al., 2013, likely can be represented in a Bjerrum plot based on the parameters varied.

On the basis of past and present experiments on sand, we find that typical laboratory experiments performed at room temperature and fast strain rates over-predict the strength of granular geomaterials for in situ crustal conditions where elevated temperatures, slow strain rates, and reactive pore fluids can weaken such materials. To improve our predictive capability for sands and sandstones, we present the results of new consolidation experiments on water-saturated quartz sand in the framework of Bjerrum

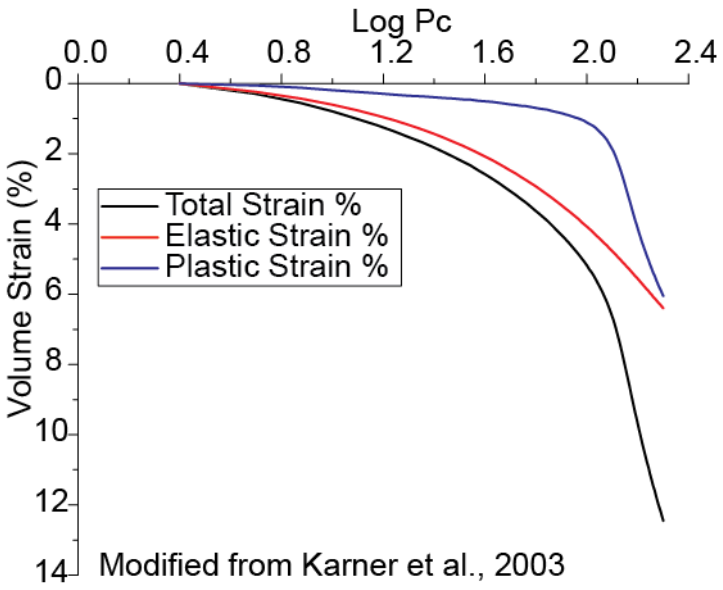

Figure 2. Total, elastic, and plastic strain for sand. Hydrostatic consolidation curves for St. Peters sand in log confining pressure versus volume strain space. Total volume strain is black, elastic strain is red, and plastic strain is blue. Modified from Karner et al., 2003.

plots, to determine P^* and the elliptical cap as a function of porosity and grain size, strain rate, temperature and in the presence of pore water.

2.2. Methods

Hydrostatic consolidation and creep compaction experiments are conducted on cylindrical packs of loose granular quartz, prepared from St. Peter sand at Battle Creek, MN. The sand is the same as that used in previous studies by *Elias and Hajash* [1992], *Dewers and Hajash* [1995], *Chester et al*., [2004], *Chester et al.* [2007], and *Karner et al.* [2008]. The loose granular quartz was acid-washed with 20% HCl solution, repeatedly rinsed with distilled water, washed in an ultrasonic cleaner, dried at room temperature, and then separated into different size fractions by sieving. The 250-350 μm grain size fraction was used in this study. Mean grain diameter and standard distribution for the sieved grains is 255 ± 60 μm. Equivalent spherical grain diameter is within 50% of the mean grain diameter for almost all of the observed grains.

Two different sample geometries were used for the experiments. Room temperature experiments used samples approximately 25 mm in diameter and 50 mm in length. Two layers of heat shrink polyolefin were used to isolate the samples from the confining medium. The jackets were sealed with a single nickel-chromium tie wire on each end cap. Room temperature samples were immersed in deionized water under a vacuum for at least 12 hours to ensure saturation. The starting porosity of room temperature samples were calculated by weight difference before and after saturation.

Samples deformed at elevated temperatures were approximately 45 mm in diameter and 80 mm in length. A three layer jacketing procedure was used: a 50 μm thick silver foil was sandwiched between two 0.64 mm thick PFA Teflon® layers. The silver jacket was annealed at 600°C for at least 12 hours. The jackets were secured to the end caps with two nickel chromium tie wires (see figure 2 of *He et al.,* [2003]). The elevated temperature sample geometry was designed to minimize diffusive transport through the jacket assembly. Elevated temperature samples were saturated in the pressure vessel. Water flowed into the sample through the bottom end cap to the top end cap under a vacuum to ensure complete saturation. For elevated temperature samples, the final porosity of the sample was calculated from the pore fluid volume at the end of the experiment as measured in the vessel at small effective pressure. The top of the sample was connected to pressurized gas, and the bottom of the sample was connected to a vacuum flask. The gas forced out the majority of the fluid for measurement. For the remnant fluid, the sample was heated under a vacuum and the resulting vapor was captured in a liquid nitrogen cooled trap. Previous studies have shown that porosities determined by pore fluid extraction agree with porosities determined by microstructural investigation within 0.5% [*F M Chester et al.*, 2007].

Room temperature experiments were conducted in a pressure vessel with flow through capability and independent confining and pore fluid pressure control. The top and bottom ends of the samples are connected for double ended drainage to allow for faster pore pressure equilibration. Samples are loaded isotropically by pressurized hydraulic fluid delivered by a screw driven pressure generator. Pore pressure was

maintained constant by a HIP® screw driven pressure generator instrumented with a LVDT to monitor displacement, and thus calculate pore volume change. Elevated temperature experiments were conducted in an externally heated pressure vessel with flow though capability, see *Hajash and Bloom* [1991] for further details. Vessel temperature, confining pressure, and pore fluid pressure are independently controlled and recorded. Samples were loaded isostatically with pressurized silicone oil as a confining medium. For consolidation experiments, the confining pressure was delivered by a combination of an air driven pump and a HIP® screw driven pressure generator. For creep experiments, the confining pressure was maintained by the HIP® pressure generator alone. For pore pressure, the bottom end of the sample was connected to an ISCO® pump that was valved off at the beginning of the experiments. The top end of the sample was connected to an HIP® screw driven pressure generator to maintain a constant pore fluid pressure. The pressure generator was equipped with a Vernier scale to measure displacement and calculate pore volume change. The vessels were heated by three zone resistance furnaces to maintain temperature within ± 1.2° C during the experiments. Confining pressure and pore fluid pressure were measured by transducers with resolution of 0.01 MPa and an absolute accuracy of 0.3 MPa.

All experiments in this study were consolidated at a constant plastic volume-strain rate. Pore pressure was held constant at 10 MPa, and confining pressure was increased in increments based on a preset time schedule. Previous work has shown that the total volume strain, ε_v, for St. Peter sand can be divided into elastic, ε_v^e, and plastic, ε_v^p, components:

$$\varepsilon_v = \varepsilon_v^e + \varepsilon_v^p.$$

The elastic behavior dominates the total strain until *P** is reached, Figure 2. Previous work has demonstrated that the elastic behavior of St. Peter sand is repeatable, and can be accurately described by a theoretical model of granular compaction based on Hertzian grain contacts [*Gangi*, 1978; *Karner et al.*, 2003]. This relationship between porosity and hydrostatic pressure is

$$\Phi(P) = \Phi_0 \frac{[1-C_0(P/P_m)^{2/3}]^3}{1-\Phi_0+\Phi_0[1-C_0(P/P_m)^{2/3}]^3},$$

where

$$P_m = 4E/3\pi(1-v^2).$$

Φ is the porosity of the material, *P* is the hydrostatic pressure, P_m is the effective elastic modulus of the grains, *E* is the Young's modulus of quartz, *v* is the Poisson's ratio for quartz, and C_0 is constant related to the packing arrangement, a value of approximately 2. The model and previous experimental results were used to calculate confining pressure increments that would result in a constant plastic strain rate. To maintain constant plastic strain rates across *P**, the time between confining pressure steps was increased. Similarly, to decrease strain rate, the time increment was increased. Consolidation experiments were performed at constant plastic strain rates of 10^{-4}, 10^{-5}, 10^{-6}, 10^{-7}, and 10^{-8} sec^{-1}, and at room temperature, 80°, 150°, and 200° C. Stepping experiments were carried out by reducing the strain rate by two orders of magnitude and increasing it back in tests at room temperature and 150° C. Creep experiments were conducted by consolidating at constant plastic volume-strain rate until the desired

effective pressure was reached, at which the point the sample was allowed to creep. Creep experiments were performed at effective pressures of 22.9, 54.7, and 94.5 MPa.

The strain rate for the experiments is defined in four different ways. The total plastic volume-strain rate for the experiments was calculated by the accumulated plastic volume strain divided by the total elapsed time, with units of sec^{-1}. The instantaneous plastic volume-strain rate was calculated by the plastic strain that occurred between consecutive measurement increments divided by the intervening time interval, with units of sec^{-1}. Total creep strain rate is defined as the accumulated plastic volume strain that occurs during the creep interval divided by the total elapsed time during the creep interval, with units of sec^{-1}. The instantaneous creep strain rate is defined as the creep strain that occurs between consecutive measurement increments divided by the intervening time interval, with units of sec^{-1}. The bulk modulus, *K*, is a measure of elastic volume change against hydrostatic compression, and was calculated for the consolidation experiments:

$K = P_e/\varepsilon_v{}^e$.

The bulk modulus is defined as elastic response, so it is typically derived from unloading curves. However, many of the experiments conducted at elevated temperatures in this study terminated with a leak, preventing measurements during unloads. The bulk modulus for these experiments was defined as the slope of the loading curve for total volume strain versus effective pressure. The slope was defined using a tangent modulus fit to the linear portion of the loading curve, but because there is some plastic strain in loading, it actually is an apparent bulk modulus, *K'*. *P** determination in these

experiments is analogous to the method used to determine preconsolidation pressure in soil mechanics experiments [*Holtz and Kovacs*, 1981]; on charts of volume strain versus log effective pressure, plastic volume strain is plotted for each experiment. Straight lines are fit for the linear portions corresponding to the low-pressure and high-pressure regimes. P^* is defined at the intersection point between these two lines.

In this paper we adopt the convention that compressive stress and contractive strains are positive. Effective pressure (P_e) is the difference between the confining pressure (P_c) and pore fluid pressure (P_p), $P_e=P_c-P_p$. All experiments are hydrostatic, $P_e=\sigma_1=\sigma_2=\sigma_3$.

2.3. Results

A total of 10 experiments were conducted: 5 at room temperature and 5 at elevated temperature. Room temperature experiments were conducted to achieve constant plastic volume-strain rates from 10^{-4} sec^{-1} to 10^{-7} sec^{-1}. Elevated temperature experiments were conducted at temperatures of 80°, 150°, and 200° C and constant plastic volume-strain rates from 10^{-6} sec^{-1} to 10^{-8} sec^{-1}, with creep strain rates reaching 10^{-11} sec^{-1}. All samples compacted continuously throughout the experiments. Total volume strain, elastic volume strain, and plastic volume strain versus effective pressure for all experiments are shown in Figure 3. Plastic volume strain versus log effective pressure is shown in Figure 4. Experimental conditions are listed in Table 1. Calculated P^* and K' are listed in Table 2.

Figure 3. Consolidation of St. Peter sand in effective pressure versus volume strain space. Black curves are total volume stain, red curves are elastic strain, and blue curves are plastic strain. a) Room temperature consolidation curves. b) Consolidation experiments performed at elevated temperature. Dashed curves represent initial loadings.

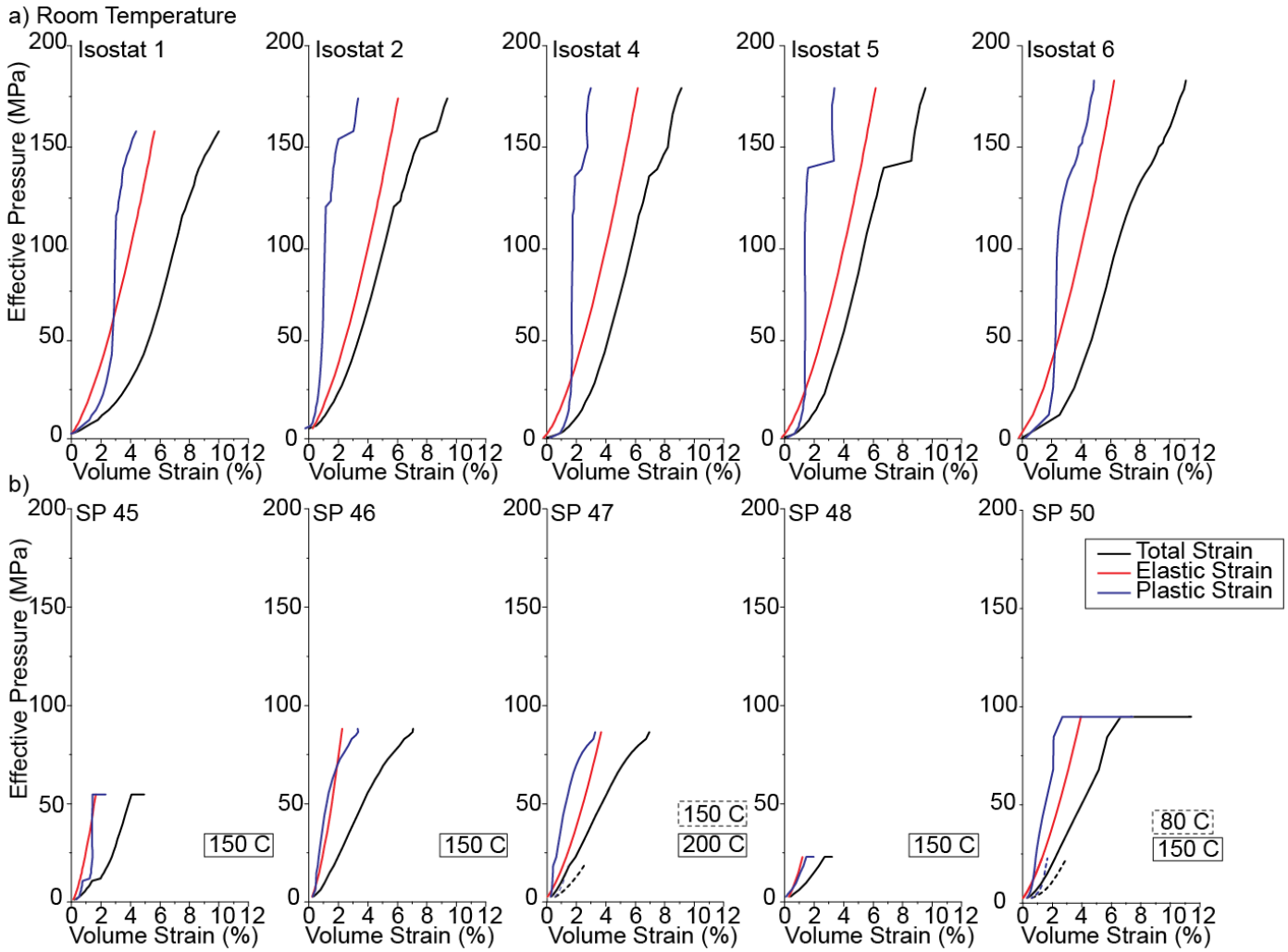
a) Room Temperature
Isostat 1
Isostat 2
Isostat 4
Isostat 5
Isostat 6
Effective Pressure (MPa)
Volume Strain (%)
b)
SP 45
SP 46
SP 47
SP 48
SP 50
150 C
150 C
150 C
200 C
150 C
80 C
150 C
Total Strain
Elastic Strain
Plastic Strain

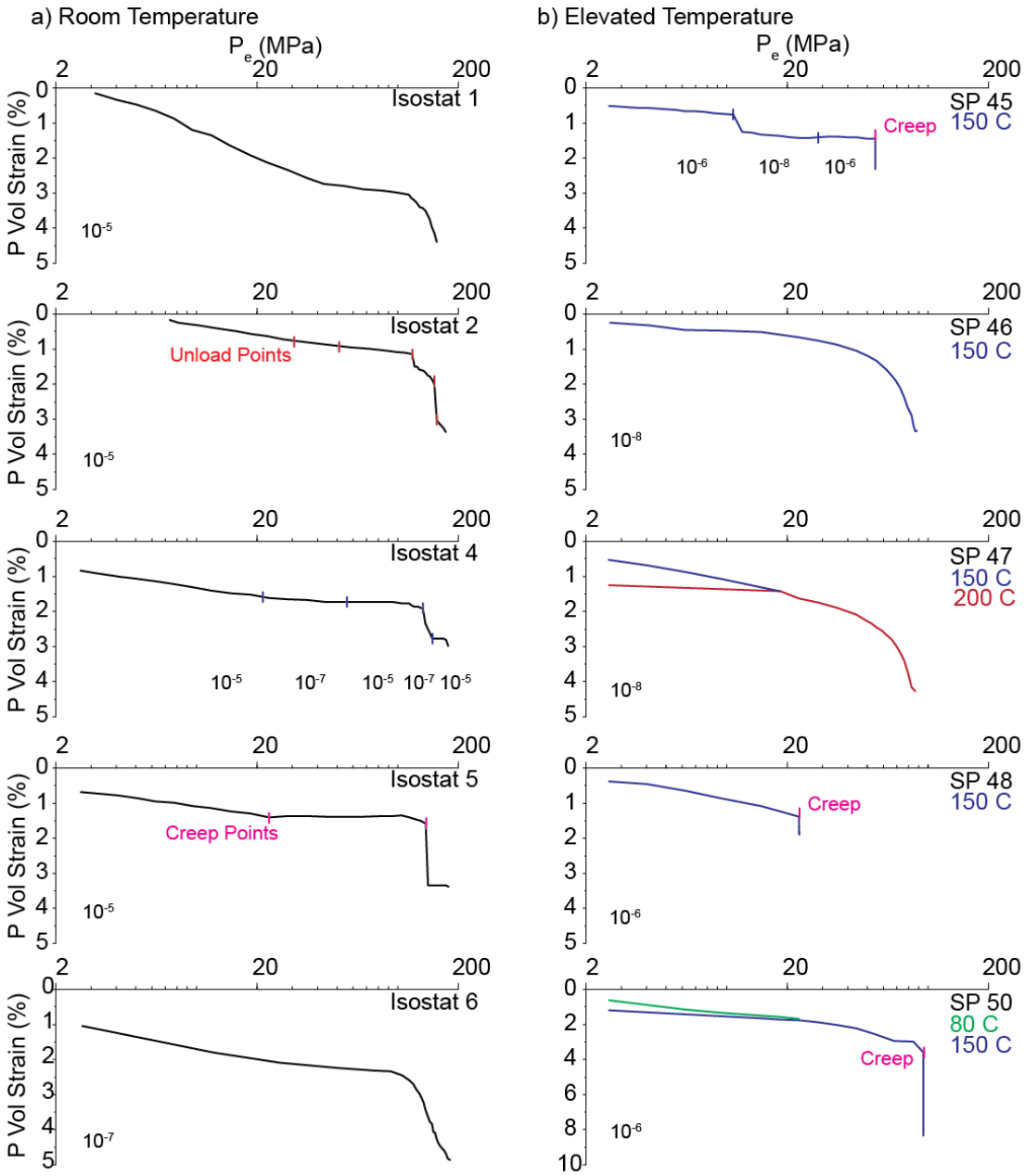

Figure 4. Plastic volume strain (%) versus log effective pressure (MPa). Graphs are annotated with experiment numbers and conditions. a) Experiments conducted at room temperature. b) Experiments conducted at elevated temperature. Green curves are performed at 80° C, blue curves are performed at 150° C, and red curves are performed at 200° C.

Experiment	Temperature (°C)	Strain Rate (sec^{-1})	Max P_e (MPa)	Creep P_e (MPa)
Isostat 1	Room	10^{-5}-10^{-6}	156.4	
Isostat 2	Room	10^{-5}	173.3	
Isostat 4	Room	10^{-4},10^{-6},10^{-4}	178.4	
Isostat 5	Room	10^{-4}-10^{-5}	178.5	23, 141
Isostat 6	Room	10^{-7}-10^{-8}	182.3	
SP 45	150.3°±0.4°	10^{-6}, 10^{-8}, 10^{-6}	54.74	54.74
SP 46	150°±1°	10^{-8}	88.15	
SP 47	149.8°±0.7°	10^{-8}	18.44	
	200°±0.3°	10^{-8}	86.43	
SP 48	150.3°±0.3°	10^{-6}	22.9	22.9
SP 50	80.0°±0.5°	10^{-6}	22.9	
	151.6°±1.2°	10^{-6}	94.9	94.9

Table 1. Temperatures, plastic volume-strain rates, maxiumum load, and creep stresses for experiments conducted in this study.

Experiment	*P** (MPa)	*K'* (GPa)
Isostat 1	111	2.82
Isostat 2	120	2.99
Isostat 4	112	3.13
Isostat 5	110	3.13
Isostat 6	102	2.78
SP 45	---	1.49
SP 46	55	1.56
SP 47	40	1.51
SP 48	---	1.05
SP 50	---	1.74

Table 2. P* and K' values for experiments conducted in this study**.**

Experiment Isostat 1 was conducted at a constant plastic volume-strain rate of 1 x 10^{-5} + 0.9 x 10^{-5} – 6.5 x 10^{-6} sec^{-1} and room temperature. The sample was consolidated to a maximum effective pressure of 156.4 MPa. The total volume strain for the experiment is 10%, 4.38% of which is plastic strain. *K'* for this experiment is 2.82 GPa. The calculated *P** value for this experiment is 111 MPa.

Experiment Isostat 2 was a series of loads and unloads conducted at a constant plastic volume-strain rate at room temperature. In total, 4 cycles of loading and unloading were performed (Figure 5). The sample was loaded to effective pressures of 39.3, 71.6, 117.9, and 148.4 MPa with subsequent unloadings to 4.2 MPa P_e. In the last loading cycle, the sample was consolidated to a maximum effective pressure of 173.3 MPa, Figure 5. The total volume strain is 9.4%, 3.36% of which is plastic strain. *K'* for the combined loading curve is 2.99 GPa. The calculated *P** for this experiment is 120 MPa.

Experiment Isostat 4 was a strain rate stepping experiment conducted at room temperature. The initial plastic volume-strain rate was 2 x 10^{-5} sec^{-1}. The strain rate was stepped to down two orders of magnitude at 22.8 MPa effective pressure; the instantaneous strain rate dropped from 1.5 x 10^{-4} sec^{-1} to 1.3 x 10^{-6} sec^{-1}. At 54.6 MPa, the loading rate was returned to the initial 10^{-5} sec^{-1} strain rate. At 137.1 MPa, the strain rate was again reduced by two orders of magnitude; the instantaneous strain rate dropped from 3.8 x 10^{-5} sec^{-1} to 4.7 x 10^{-7} sec^{-1}. At 152.6 MPa, the loading rate was increased to the original 10^{-5} sec^{-1} strain rate. The sample was consolidated to a maximum effective pressure of 178.4 MPa. The total volume strain is 9.14%, 2.98% of which is plastic

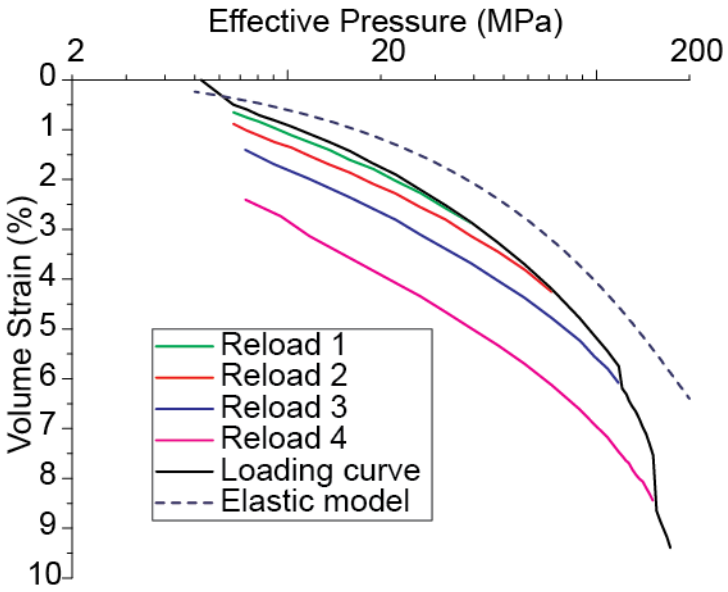

Figure 5. Load and reload curves for experiment Isostat 2 compared to the theoretical elastic model. Log effective pressure versus volume strain. Solid curves are the load and reload curves, the dashed curve is the elastic model. The solid black curve is the total volume strain; the green curve, first reloading curve; red curve, the second reloading curve; blue, third reloading curve; pink curve, fourth reloading curve.

strain. *K'* for this experiment is 3.13 GPa. The calculated *P** value for this experiment is 112 MPa.

Experiment Isostat 5 was conducted at a constant plastic volume-strain rate of $7.33 \times 10^{-5} \pm 4.78 \times 10^{-5}$ sec^{-1} at room temperature with week-long holds conducted at both 23 MPa and 141 MPa effective pressures. The hold time was 5.87×10^{5} seconds at 23 MPa P_e, and 6.01×10^{5} seconds at 141 MPa P_e. The sample was consolidated to a maximum effective pressure of 178.5 MPa. The recorded total volume strain is 9.55%, 3.49% of which is plastic strain. Slow leaks in the system prevented accurate measurements of pore volume during the prolonged holds. *K'* is calculated after the first hold and before the second hold, a value of 3.13 GPa. The calculated *P** value for this experiment is 110 MPa.

Experiments Isostat 6 was conducted at a constant plastic volume-strain rate and room temperature. The initial plastic volume-strain rate was $1 \times 10^{-7} + 1 \times 10^{-7} - 7.84 \times 10^{-8}$ sec^{-1}. The maximum effective pressure was 182.3 MPa. Total volume strain is 11.11%, 4.86% of which is plastic strain. *K'* for this experiment is 2.78 GPa. The calculated *P** for this experiment is 102 MPa.

Experiment SP 45 was conducted at 150.3° ± 0.4° C, the strain rate was varied by two orders of magnitude. The initial plastic volume-strain rate was 2.5×10^{-6} sec^{-1}; at 12 MPa, the strain rate was reduced to 2.5×10^{-8} sec^{-1}. At 28.5 MPa P_e, the loading rate was returned to the original 10^{-6} sec^{-1} strain rate. The sample was consolidated to 54.74 MPa, where it was allowed to creep for 5.09×10^{6} seconds and achieve 0.88% volume strain. The total plastic volume-strain rate reduced to 4.01×10^{-9} sec^{-1} at the end of the

creep stage, the plastic volume-strain rate for creep reduced to 1.75×10^{-11} sec^{-1}. Two different *K'* were measured for this experiment. *K'* for the portion of the experiment conducted at the slower strain rate is 1.49 GPa. *K'* after returning to the faster strain rate is 2.34 GPa.

Experiment SP 46 was conducted at a constant plastic volume-strain rate at elevated temperatures of 150° ±1° C. The plastic volume-strain rate of the experiment was $1.59 \times 10^{-8} \pm 1.21 \times 10^{-8}$ sec^{-1}. The total volume strain is 7.05%, of which 3.32% is plastic. The sample was consolidated to a maximum effective pressure of 88.15 MPa. *K'* for this experiment is 1.56 GPa. The calculated *P** for this experiment is 55 MPa.

Experiment SP 47 was conducted at a constant plastic volume-strain rate at two different temperatures of 149.8° ± 0.7° C and 200 ± 0.3 C. The sample was initially loaded at a plastic volume-strain rate of 10^{-8} sec^{-1} up to 18.44 MPa P_e at 149.8 ± 0.7 C, unloaded, the temperature was increased to 200° ± 0.3° C, and the sample was loaded at a constant plastic volume-strain rate of $2.33 \times 10^{-8} \pm 0.32 \times 10^{-8}$ sec^{-1} to a maximum effective pressure of 86.43 MPa. In the initial loading, the sample compacted by 2.52%, 1.43% of which is plastic. In the subsequent reloading at higher temperature, the sample compacted by 6.96%, of which 3.28% is plastic. *K'* for the experiment was 1.51 GPa. The calculated *P** for this experiment is 40 MPa.

Experiment SP48 was conducted at constant plastic volume-strain rate at elevated temperatures of 150.3° ± 0.5° C. The sample was compacted at a strain rate of 2.5×10^{-6} to 22.9 MPa P_e, at which point it was allowed to creep for 1.26×10^{6} seconds. In the initial loading to 22.9 MPa, the sample compacted by 2.70%, of which 1.39% is

plastic. During the creep phase, the sample compacted by a further 0.65%. In total, the sample compacted by 3.20%, of which 1.89% is plastic. The final plastic volume-strain rate was 1.5 x 10^{-9} sec^{-1}, and the final strain rate for the creep portion was 4.16 x 10^{-10} sec^{-1}. *K'* for this experiment was 1.05 GPa.

Experiment SP 50 was conducted at a constant plastic volume-strain rate and temperatures of 80.0° ± 0.5° C and 151.6° ± 1.2° C. The sample was initially loaded at 80° C to 22.9 MPa, unloaded, the temperature was raised to 151.6° C, and the sample was loaded to 94.9 MPA P_e. At 94.9 MPa P_e, the sample was allowed to creep for 1.08 x 10^7 seconds. In the initial loading, the sample was loaded at a plastic volume-strain rate of 4.88 ± 2.2 x 10^{-6} sec^{-1}; the total volume strain is 2.98%, 1.67% of which is plastic. In the reload at 151.6 C to 94.9 MPa P_e, the plastic volume-strain rate was 2.9 ± 1.02 x 10^{-6} MPa. The total volume strain is 6.3%, 2.69% of which is plastic. During the creep stage, the sample further compacted by 5.5%. The creep strain-rate reached as low as 5.1 x 10^{-11} sec^{-1} at the end of the creep phase. *K'* measured during the reload at 150° C is 1.74 GPa.

2.4. Discussion

The experiments demonstrate that there is a clear dependence of *P** on experimental conditions, Table 2. For experiments conducted at room temperature and consolidated at a constant plastic volume-strain rate corresponding to the standard laboratory strain rate of 10^{-5} sec^{-1}, $\dot{\varepsilon}^p_{ref}$, the critical pressure for crushing St. Peters sand is 111 ± 1 MPa. Experiments Isostat 1, Isostat 4, and Isostat 5 all indicate a *P** value in

this range. Only the experiment Isostat 2 has a higher P^*, and the difference is likely due to effects of imposing multiple unload-reload cycles. The value determined for P^* herein is very close to the previous reported values of P^* for St. Peters sand of 107 MPa [*Karner et al.*, 2005]. For the experiment conducted at room temperature and a plastic volume-strain rate two orders of magnitude lower than $\dot{\varepsilon}^p_{ref}$, the critical pressure is 102 MPa, which is only slightly lower than the standard value. Karner et al., 2008, demonstrated that the consolidation of St. Peters sand is strongly dependent on temperature. At 150° C and total volume-strain rates similar to $\dot{\varepsilon}^p_{ref}$, P^* for St Peters sand is 95 MPa. At 225° C and standard laboratory rates, P^* is estimated as 70 to 80 MPa based on triaxial experiments in the high pressure regime [*Karner et al.*, 2008]. Changing either temperature or strain rate, at the otherwise typical laboratory conditions, the consolidation of St. Peters sand is only slightly affected. At $\dot{\varepsilon}^p_{ref}$, increasing the temperature to 150° C decreases P^* by roughly 10%. At room temperature, decreasing the strain rate by two orders of magnitude decreases P^* by 7%.

Experiments in which both temperature is increased and strain rate is reduced illustrate significant reduction in P^*. In addition, microstructural studies of such experiments also evidence dramatic changes. A significantly greater number of microfractured grains is observed at 34.5 MPa P_e at 150° C after long creep experiments, and similarly after a brief hold at 55.2 MPa and 200° C, relative to the laboratory standard temperature and rate tests [*J S Chester et al.*, 2004; *Dewers and Hajash*, 1995]. In experiments SP 46, P^* for St Peter sand consolidated at a plastic volume-strain rate of 10^{-8} sec^{-1} at 150° C is reduced to 55 MPa. This is a 50% reduction compared to the

room temperature and $\dot{\varepsilon}^{p}_{ref}$. With an increase in temperature to 200° C, P^* further reduces to 40 MPa, a 64% reduction compared to the standard laboratory experiment. These results indicate that using typical laboratory experiments greatly overestimates P^* of porous, granular quartz sand, and therefore overestimate the stress magnitudes for the shear enhanced compaction envelope, and accordingly the stress conditions for the transition from low pressure dilational failure and high pressure compactional failure.

Clear changes in mechanical behavior due to increased temperature and decreased strain rate are reflected in the experimental determinations of apparent bulk moduli, Table 2. The apparent bulk modulus is measured from the total volume strain; as elastic strain is defined as recoverable strain independent of temperature and strain rate, variations in K' reflect differences in the accumulation of plastic volume strain. These variations mirror the observed trends in P^*. K' values are highest for typical laboratory experiments conducted at $\dot{\varepsilon}^{p}_{ref}$ and room temperature. For experiments Isostat 1, Isostat 2, Isostat 4, and Isostat 5, K' are 3.02 ± 0.13 GPa. Room temperature experiments with decreased strain rates have decreased bulk moduli. Isostat 6 is two orders of magnitude slower than the other room temperature experiments, and K' reduces to 2.78 GPa. Elevated temperature further reduce K'. At 150° C and a constant plastic volume-strain rate of 10^{-6} sec^{-1}, K' reduces to 2.04 ± 0.3 GPa. If the strain rate is decreased to 10^{-8} sec^{-1}, K' further decreases to 1.50 GPa at 150° C. The apparent modulus value is less than half of the measured apparent moduli in the room temperature, $\dot{\varepsilon}^{p}_{ref}$ experiments. This reduction also reinforces that combined temperature and strain rate effects can be quite significant.

Previous experiments have demonstrated that the plastic consolidation curves for quartz sand consolidated at similar strain rates but different temperatures have approximately parallel slopes when plotted in porosity versus log effective pressure space (Figure 1). The higher temperature curves have lower porosity values for a given effective pressure, but the slopes for all the temperatures are otherwise parallel; the difference between the curves is that P^* reduces with elevated temperatures. This behavior can be described as shifting a reference consolidation curve to lower P^* values with increasing temperature. This behavior has been demonstrated in soil mechanics literature for preconsolidation pressures by *Bjerrum*, 1967, and others. To test if this theory applies to the consolidation of sand and other porous granular materials, the constant plastic volume-strain rate experiments from this study were compared against previous work on St. Peters sand by *Karner et al.*, [2008] in porosity versus log effective pressure space (Figure 6a). The absolute starting porosity of the experiments can be difficult to measure as some volume strain occurs during the initiation of confining pressure and before pore pressure is established. There is a minor amount of compaction that occurs during this initiation. Due to uncertainties in absolute starting porosity and in order to better illustrate behavior, the reference starting porosity has been adjusted by ± 2.5% to align the curves vertically. P_e is not adjusted, so P^* is accurately maintained. Figure 6a demonstrates that there is a systematic shift in the volume strain behavior to lower effective pressures with decreasing P^*, but the curves otherwise have similar shapes. The previous experiments at $\acute{\varepsilon}^p_{ref}$ show a decrease in strength with elevated temperatures, and the experiments presented here demonstrate behavior that can be

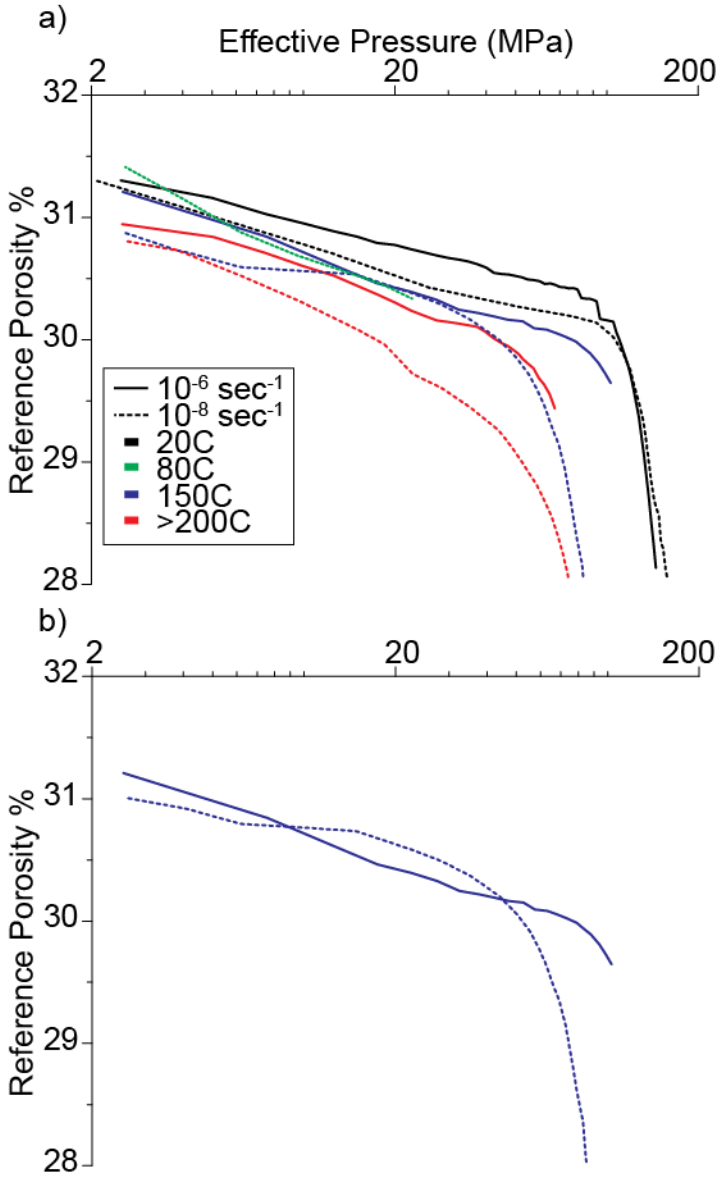

Figure 6. Plastic consolidation of St. Peters sand in log effective pressure versus porosity space. a) Comparison of consolidation experiments conducted at 10^{-6} sec^{-1}, solid curves, and 10^{-8} sec^{-1}, dashed curves, and at temperature of 20° C, black curves, 80° C, green curve, 150° C, blue curves, and over 200° C, red curves. b) Comparison of consolidation experiments performed at 150° C and at 10^{-6} sec^{-1}, solid curve, and 10^{-8} sec^{-1}, dashed curve.

described by consolidation curves shifting to lower *P** values with decreasing strain rates. Figure 6b highlights the effect of strain rate on consolidation. The solid curve is the standard laboratory strain rate experiment conducted at 150° C, and the dashed curve is the experiment conducted at a constant plastic volume-strain rate of 10^{-8} sec^{-1} at 150° C. This demonstrates that the curve for the slower strain rate has been shifted to lower effective pressure values corresponding to a decrease in *P** from 95 to 55 MPa. Other than lowered *P** values, the curves are otherwise similar and have parallel slopes for Regime 1 and 2. Experiments at elevated temperatures and reduced strain rates have a more gradual transition associated with P* as opposed to room temperature and $\dot{\varepsilon}^{p}_{ref}$ experiments. This could be an artifact from using the room temperature elastic correction for elevated temperatures, but more likely reflects the enhanced thermally-activated subcritical crack growth at these conditions [*F M Chester et al.*, 2007; *J S Chester et al.*, 2004]. This behavior agrees with the Bjerrum model and supports the application of this clay rich soil model to the high pressure consolidation of granular materials.

Following the example of Leroueil et al., 1985, who confirmed Bjerrum's model by using special strain rate stepping oedometer tests on Batiscan clay, experiments that were conducted at a constant plastic volume-strain rate are compared to experiments where the instantaneous plastic volume-strain rate was stepped by two orders of magnitude to test the applicability to high pressure consolidation of granular materials. This approach also eliminates any variability in starting porosity when comparing two different strain rates, allowing for a determination of rate effects on porosity changes.

Experiment Isostat 4 tested the model at room temperature, and SP 45 tested the model at 150° C. Figure 7a demonstrates the behavior at 150° C for Regime 1. Experiment SP 45, where the strain rate was stepped from 10^{-6} sec^{-1} to 10^{-8} sec^{-1} and back, is compared against SP 46, which was conducted at a constant plastic volume-strain rate of 10^{-8} sec^{-1}. These experiments demonstrate that during initial loading, curves are parallel for strain rates of 10^{-6} sec^{-1} and 10^{-8} sec^{-1}. When the strain rate is decreased in SP45, there is a sharp decrease in porosity. After the initial decline, the subsequent 10^{-8} sec^{-1} curve is parallel to the experiment at a constant 10^{-8} sec^{-1}. The strain rate is increased in SP45, but never re-achieves the original consolidation curve before a secondary creep test was initiated, i.e., the loading was still in tertiary consolidation when the secondary creep phase was begun, while SP 46 shortly thereafter transitions through P^* into Regime 2. Figure 7b demonstrates the behavior at room temperature for Regime 2. Experiment Isostat 4, where the strain rate was stepped from 10^{-5} sec^{-1} to 10^{-7} sec^{-1}, and back to 10^{-5} sec^{-1}, is compared against experiment Isostat 6, conducted at a constant plastic volume-strain rate of 10^{-7} sec^{-1}. The experiments demonstrate that during the initial loading, the different strain rates have parallel curves. For experiment Isostat 4, when the strain rate is decreased by two orders of magnitude, there is a sharp decrease in porosity associated with this change. Subsequent consolidation at 10^{-7} sec^{-1} is parallel to the consolidation curve conducted at a constant 10^{-7} sec^{-1}. When the strain rate in Isostat 4 is returned to 10^{-5} sec^{-1}, there is a transitional period where the curve shifts to the original loading envelope, and subsequently consolidates parallel to the 10^{-7} sec^{-1} envelope. The experiments demonstrate that for Regimes 1 and 2, for room temperature and elevated

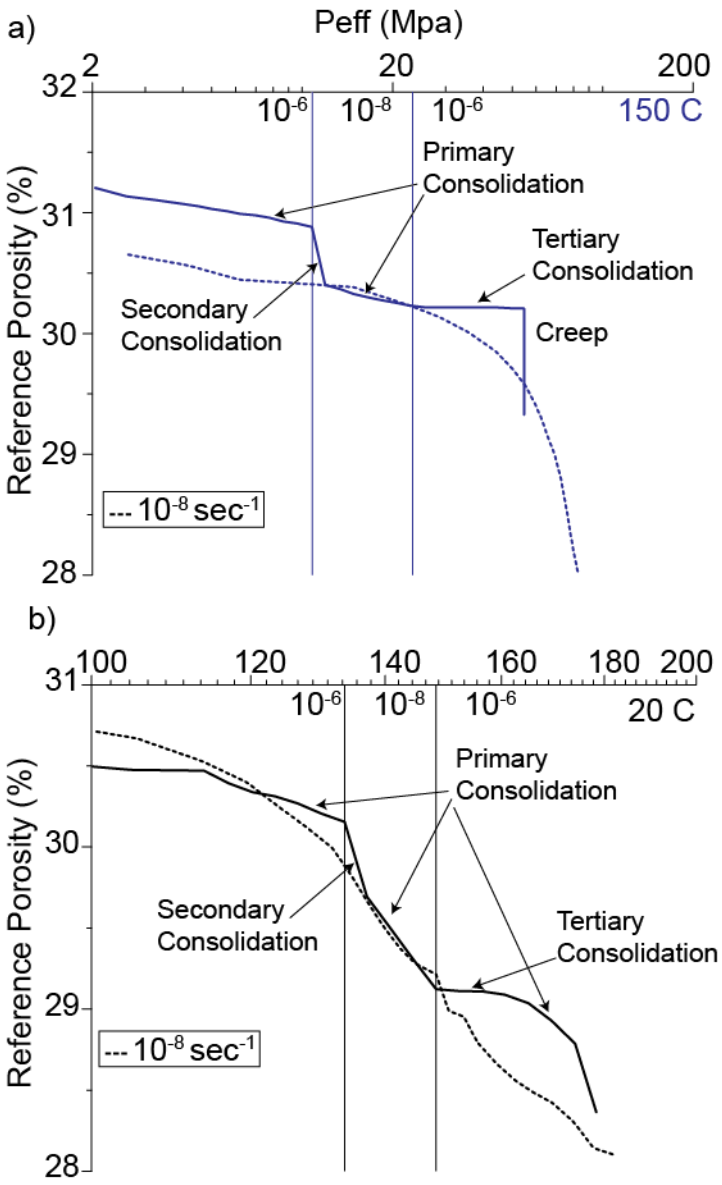

Figure 7. Comparison of strain rate effects in plastic consolidation of St. Peters sand in porosity versus log effective pressure space. a) Strain rate effects in the low effective pressure regime, Regime 1, conducted at 150° C. Dashed curve is conducted at a constant plastic strain rate of 10^{-8} sec^{-1}, for the solid curve the strain rate is stepped between 10^{-6} sec^{-1}, 10^{-8} sec^{-1}, and back to 10^{-6} sec^{-1}. b) Strain rate effects in the high effective pressure regime, Regime 2, conducted at room temperature. Dashed curve is conducted at a constant plastic strain rate of 10^{-7} sec^{-1}, for the solid curve the strain rate is stepped between 10^{-5} sec^{-1}, 10^{-7} sec^{-1}, and back to 10^{-5} sec^{-1}.

temperature, the consolidation of quartz sand can be described by a series of parallel envelopes corresponding to different strain rates as developed for the normal consolidation of clay rich soils.

Other behaviors seen in experiments can also be explained using the Bjerrum framework. In experiments Isostat 4 and SP 45, when the strain rate is decreased, there is a sharp decrease in porosity before the curves return to the original slope. Figure 8 compares the behavior seen in experiment SP45 against the behavior seen in the Bjerrum model. In the Bjerrum framework, the sample essentially creeps to a lower strain rate curve, and the sample then consolidates along the lower strain rate curve. When experiments Isostat 4 and SP 45 return to the original strain rate, there is a stiffer loading portion with a reduced slope (Figure 7, 8). A similar behavior can be seen in experiment Isostat 5, where the consolidation curve is flat after the prolonged hold. This behavior can be explained as tertiary consolidation in the Bjerrum framework (Figure 8). In this framework, a sample creeping at a constant effective pressure, or consolidating at a slower strain rate, needs to transition to the newer faster strain rate curve before consolidating normally. The experiments Isostat 4, Isostat 5, and SP 45 are essentially overloaded for the new strain rate consolidation curve, even though they are at their maximum consolidation pressure. In SP 45, in the step up in plastic volume-strain rate from 10^{-8} sec^{-1} to 10^{-6} sec^{-1}, the sample would have to reach the dashed consolidation curve corresponding to 10^{-6} sec^{-1} before consolidating normally (Figure 8). Hence the semi-elastic tertiary consolidation as the samples plastically deform very little until the load path intersects the consolidation curve for the faster strain rate. A slope change can

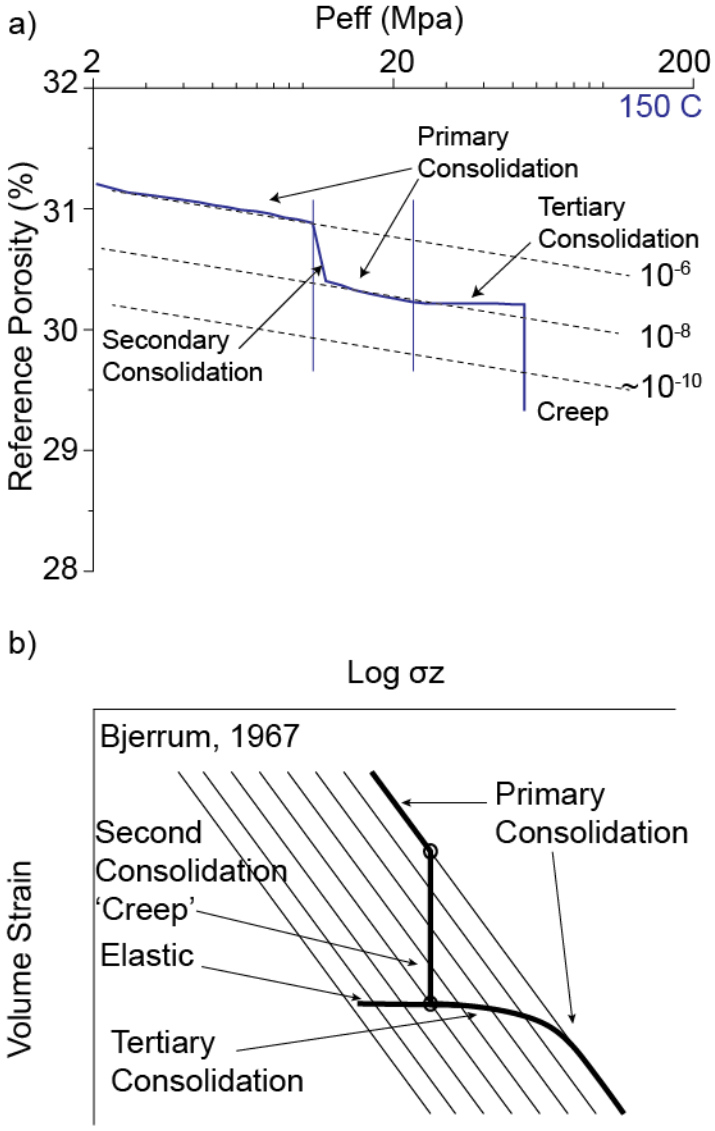

Figure 8. Comparison of experiment SP 45 to Bjerrum model in porosity versus log effective pressure space. a) Strain rate effects in the low effective pressure regime, Regime 1, conducted at 150° C. The strain rate is stepped between 10^{-6} sec^{-1}, 10^{-8} sec^{-1}, and back to 10^{-6} sec^{-1}. Dashed black curves show approximate locations of parallel consolidation curves based off of this experiment. Behavior of experiment is annotated. b) Model for 1D consolidation of clay rich soils from Bjerrum, 1967, in log normal stress versus volume strain space.

be seen in experiments Isostat 4 and Isostat 5 as the samples transition from tertiary consolidation to normal consolidation, SP 45 does not reach high enough stresses to transition to normal consolidation.

The constant plastic volume-strain rate consolidation experiments and the strain rate stepping consolidation experiments have demonstrated that the parallel consolidation curves theory developed for normally consolidated soils by Bjerrum, 1967, also applies to quartz sand. The applicability of the framework can be used to extend laboratory results to in situ conditions. The consolidation curves presented here reached strain rates as low as 10^{-8} sec^{-1}. Due to experimental limitations, it is prohibitive to consolidate at slower strain rates, even though engineering strain rates for reservoirs are at least an order of magnitude slower, and geologic strain rates are at least four orders of magnitude slower. Utilizing this framework the creep experiments presented here as well as from previous work can be used to establish consolidation curves at strain rates as low as 10^{-10} sec^{-1}, applicable to engineering applications and closer to geologic conditions, an approach was first demonstrated by Leroueil et al., 1985. The authors identified a series of constant strain rate curves using the creep strain rate from 9 creep experiments. The creep strain rates from the experiments conducted here are presented in Figure 9. Due to differences in loading paths between the previous work and experiments conducted in this study, this approach must be modified. Here, the creep experiments are hung off reference consolidation curves, the experiments conducted at a constant plastic volume-strain rate of 10^{-6} sec^{-1} and 10^{-8} sec^{-1}. In this manner, the shape of the consolidation curves from these experiments can be extrapolated to lower strain

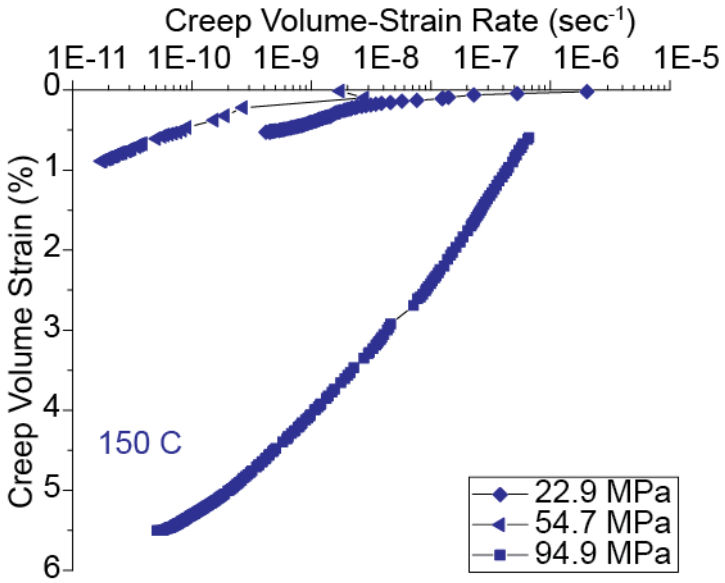

Figure 9. Creep compaction experiments. Plastic volume strain versus plastic volume-strain rate for the creep portion of two experiments, SP 45 (54.7 MPa), SP 48 (22.9 MPa), and SP 50 (94.9 MPa). SP 45 is represented by the blue triangles; SP 48, blue diamonds; SP 40, blue squares.

rates and predict declines in P^*. Figure 10a shows the results for 150 C. Creep experiments at 22, 54.5, 95 MPa, and a creep experiment at 34.5 MPa from *He et al.,* [2003] are hung off references curves of SP 46 and a consolidation experiment at 10^{-6} sec^{-1} and 150° C from *Karner et al.,* [2008]. The instantaneous creep strain rates are annotated on the creep experiments. For the creep experiment at 22 MPa, the strain rates of 10^{-9} sec^{-1}, 10^{-10} sec^{-1}, and 10^{-11} sec^{-1} are close together. With increasing creep stress, the slower creep strain rates start to diverge. This is due to the reduction in P^* at slower strain rates; the consolidation curves shift to lower effective pressures. The change in spacing is due to the difference in slope between Regime 1 and Regime 2. To determine the shape of the reference curve, experiments were fit in plastic volume strain versus log P_e space with a linear line for both Regimes 1 and 2.

$$Plastic\ Volume\ Strain\ (\%) = a + b' \times \log(P_e),$$

where, a is the intercept, and b' is the slope of the curves. b' values are tabulated in Table 3. The shape of the reference consolidation curve was determined by an average of the b' values for all experiments. Due to load path effects (e.g., cyclic load and unloads, incomplete tertiary consolidation), some curves do not represent normal consolidation behavior and are excluded from the average. The slope of the line defining Regime 1 is 0.92 (%/sec^{-1}), and the slope of the line defining Regime 2 is 14 (%/sec^{-1}). To determine the spacing of the parallel consolidation curves, the porosity change due to changing plastic volume-strain rates for both creep experiments and strain rate stepping experiments are tabulated in Table 4. Spacing between two orders of magnitude change is greater for Regime 2 than Regime 1, and spacing increases with

Experiment	Temperature (°C)	Strain Rate (sec^{-1})	Regime 1 slope	Regime 2 slope
Isostat 1	Room	10^{-5}	~~2.09~~	14.04
Isostat 2	Room	10^{-5}	0.85	~~6.94~~
Isostat 4	Room	10^{-4},10^{-6},10^{-4}	0.82	12.37
Isostat 5	Room	10^{-5}	0.79	~~3.88~~
Isostat 6	Room	10^{-7}	1	13.82
SP 45	150.3°±0.4°	10^{-6}, 10^{-8}, 10^{-6}	0.41, 0.53	----
SP 46	150°±1°	10^{-8}	0.44	14.87
SP 47	149.8°±0.7°	10^{-8}	1.07	----
	200°±0.3°	10^{-8}	~~1.43~~	14.91
SP 48	150.3°±0.3°	10^{-6}	1.18	----
SP 50	80.0°±0.5°	10^{-6}	1.03	----
	151.6°±1.2°	10^{-6}	1.1	----

Table 3. Determination of Bjerrum consolidation curve for quartz sand. Slopes are calculated with linear fit for the equation "Plastic Volume strain = $a + b'$* log (P_e), for pre and post P*. Values that are crossed through were eliminated due to load path effects.

Experiment	Temperature (°C)	Strain Rate (sec^{-1})	Regime 1 Porosity Change (%)	Regime 2 Porosity Change (%)
Isostat 4	Room	10^{-5} to 10^{-7}	----	0.41
SP 45	150.3°±0.4°	10^{-6} to 10^{-8}	0.48	----
SP 48 Creep @ 22.9 MPa	150.3°±0.3°	10^{-7} to 10^{-9}	0.38	----
He et al., [2003] Creep @ 34.5 MPa	150°	10^{-8} to 10^{-9}	0.25	----
He et al., [2003] Creep @ 34.5 MPa	150	10^{-9} to 10^{-10}		1.01
SP 45 Creep @ 54.7 MPa	150.3°±0.4°	10^{-9} to 10^{-11}	----	0.88
SP 50 Creep @ 95 MPa	151.6°±1.2°	10^{-8} to 10^{-10}	----	2.94

Table 4. Effect of strain rate changes on consolidation curve spacing.

elevated temperature. For the creep experiment at 34.5 MPa, the porosity change increases with decreasing strain rate, suggesting that it has passed though *P** between creep volume-strain rates of 10^{-8} sec 10^{-9} sec^{-1}. Figure 10b shows the Bjerrum plot for quartz sand based off of the experimental results from this study, *Karner et al.,* [2008], and *He et al.,* [2003]. The solid blue curves represent the reference consolidation curve based off of the slopes in Table 3. The consolidation curves for plastic volume-strain rates of 10^{-6} sec^{-1} and 10^{-8} sec^{-1} reflect *P** values in Table 2. The vertical dashed black curves represent the spacing for the curves determined from creep and strain rate stepping experiments (Table 4). The diagonal dashed black line represents the best fit lines for *P**. The dashed blue curves represent the extrapolated consolidation curves to slower strain rates than what is achievable in creep experiments. The curves were extrapolated by maintaining similar spacing and following the *P** line. Based off of the creep results, the consolidation curve at a constant plastic volume-strain rate of 10^{-10} sec^{-1} would go through *P** at 33.3 MPa. This is a significant reduction compared to the standard laboratory experimental value of 111 MPa. At the geologic strain rate of 10^{-12} sec^{-1}, *P** is 20.4 MPa. At a strain rate of 10^{-14} sec^{-1}, *P** is 12.5 MPa. These results indicate sediments undergoing burial would pass though *P** within a couple kilometers of burial depth. Figure 11 shows the failure envelope for St. Peters sand at 150° C for different strain rates as a function of depth (effective pressure). Karner et al., [2008], demonstrated that dilatant Coulomb behavior for St. Peters sand is not sensitive to temperature or strain rate, but shear enhanced compaction in the elliptical cap region is. This study demonstrates that *P** is also sensitive to temperature and strain rate, and the

Figure 10. Parallel consolidation curves for St. Peter sand. a) Plastic porosity reduction from constant plastic consolidation strain rate experiments and secondary creep experiments from this study and Karner et al., 2008, He et al., 2003, plotted in log effective pressure versus porosity space. All experiments at 150° C. Solid curve is 10^{-6} sec^{-1}, dashed curve is 10^{-8} sec^{-1}. Vertical lines are creep experiments. Creep strain rates are annotaed on experiments. b) Model based off parallel consolidation curves. Solid blue curves are consolidation curves for constant plastic volume-strain rates based off averaged slopes of experimental curves. Strain rates annotated on curves. Vertical dashed black lines depict spacing of curves determined from creep experiments and strain rate stepping experiments. Diagonal dashed black line is best fit line through P* values. Dashed blue curves are extrapolated consolidation curves.

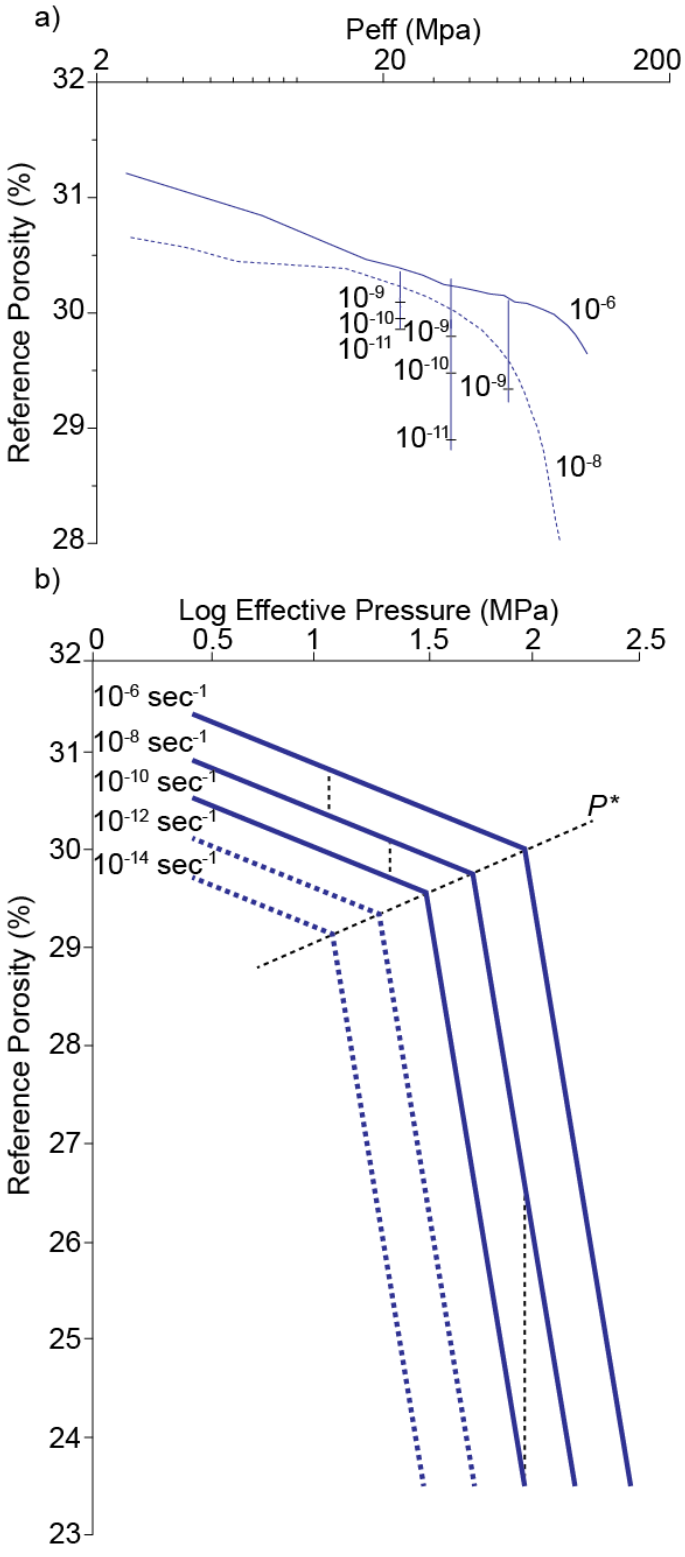
a)
Peff (Mpa)
2
20
200
32
31
30
29
28
Reference Porosity (%)
10-9
10-10
10-11
10-9
10-10
10-9
10-11
10-6
10-8
b)
Log Effective Pressure (MPa)
0
0.5
1
1.5
2
2.5
32
31
30
29
28
27
26
25
24
23
Reference Porosity (%)
10-6 sec-1
10-8 sec-1
10-10 sec-1
10-12 sec-1
10-14 sec-1
P*

significant reduction from the combined effect has so far been unappreciated. The decreases in P^* from this study demonstrate that the failure envelope collapses significantly at geologic strain rates (Figure 11, Table 2). Proppant used to maintain fracture aperture in unconventional reservoirs could also be at P^* conditions over the life of the well if the reservoir is deeper than about 3 km. The temperature in the experiments are much higher than in situ conditions at shallow burial depths, but P^* would still be lower than expected.

The critical pressure of porous granular material is a function of temperature, strain rate, and chemical environment, all of which evolve throughout the burial and diagenesis process. The Bjerrum plot in Figure 10 extrapolates behavior at 150° C, but the experiments in this study do not provide sufficient data coverage to determine spacing at other temperatures. In an attempt to extrapolate the experimental results to burial, P^* was plotted as a function of strain rate and temperature. Because the temperature and time effects are classically described using Arrhenius relationships, the 3D surface was fit with an exponential function (Figure 12a):

$$P^* = z_0 + B * \exp(-\dot{\varepsilon}/C) * \exp(T^{-1}/D).$$

Where z_0 is 264.6 MPa, B is -403.2 MPa, C is 3.79 x 10^{-3} sec^{-1}, D is 3.62 x 10^{-3} K^{-1}, $\dot{\varepsilon}$ is strain rate in sec^{-1}, T is temperature in Kelvin. The R^2 value of the fit is 0.83. The curve adequately handles changes in temperature based on the four values of experimental values, but it is insensitive to variations in strain rate as compared to observations from experimental results. The function can illustrate changes in P^* from increasing temperature during burial assuming constant strain rates. To correct the 3D function, P^*

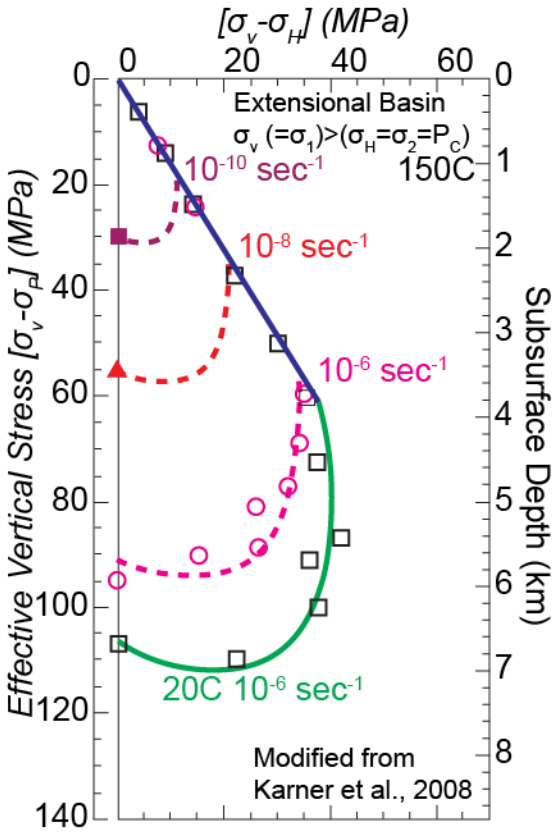

Figure 11. Failure envelope for St. Peter sand, modified from Karner et al., 2008. Vertical stress and calculated burial depth versus differential stress. Failure envelopes at 20° C are solid curves, and 150° C, dashed curves. Black squares are 20° C experiments at 10^{-6} sec^{-1}; pink circles, 150° C at 10^{-6} sec^{-1}; red triangles, 150° C at 10^{-8} sec^{-1}; purple squares, 150° C at 10^{-10} sec^{-1}. Previous work is represented with open symbols.

a)

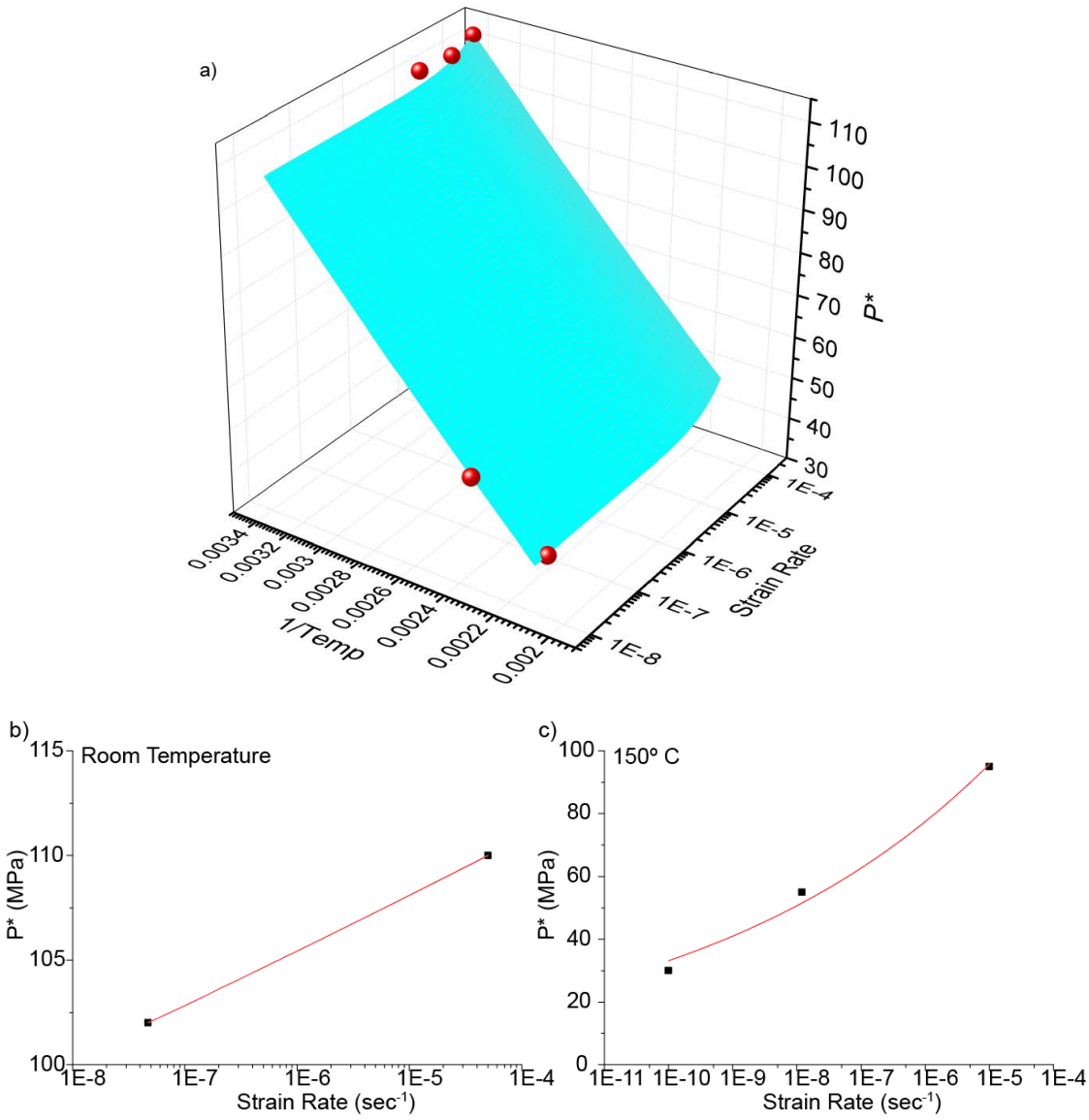

Figure 12. *P** extrapolation to nature. a) *P** plotted as a function of strain rate and temperature. Red spheres represent *P** values, blue curve represents exponential fitting function. b) *P** plotted as a function of strain rate for room temperature experiments. Red curve is fitted exponential function. c) *P** plotted as a function of strain rate for 150° C experiments. Red curve is fitted exponential function.

was fit as function of plastic volume-strain rate for room temperature and 150° C (Figure 12b,c):

$P^* = a_0 \dot{\varepsilon}^b$.

For room temperature, a_0 is 122.46, b is 1.08 x 10^{-2}; for 150° C, a_0 is 276.72, b is 9.212x 10^{-2}. At a strain rate of 10^{-15} sec^{-1}, the 3D fitted function over predicts P^* compared to individual 2D fits of P^* by 20 MPa at room temperature and 43 MPa at 150° C; at a strain rate of 10^{-12} sec^{-1}, 14 MPa, 35 MPa; at a strain rate of 10^{-9} sec^{-1}, 6 MPa, 14 MPa; at a strain rate of 10^{-6} sec^{-1}, the function under predicts P^* by 2 MPa at room temperature and 23 MPa at 150° C. The function has been shifted to correct the disparity with a linear correction. For the burial stress calculation, the effective stress gradient is assumed to be 15 MPa per kilometer, and the effective temperature gradient is assumed to be 20° C per kilometer with a surface temperature of 25° C. The effective stress gradually increases as the burial depth increases, while the critical pressure decreases with burial (Figure 13). According to these calculations, at a strain rate of 10^{-15} sec^{-1}, the sediments would go through P^* at a burial depth of 3.09 km, where the effective pressure is 46.4 MPa and the temperature is 87° C. At a strain rate of 10^{-12} sec^{-1}, the sediments would go through P^* at a burial depth 3.35 km, where the effective pressure is 50.3 MPa and the temperature is 92° C. At a strain rate of 10^{-9} sec^{-1}, the sediments would go through P^* at 3.97 km, where the effective pressure is 59.6 MPa and the temperature is 104° C. At a strain rate of 10^{-6} sec^{-1}, the sediments would go through P^* at 5.38 km, where the effective pressure is 80.7 MPa and the temperature is

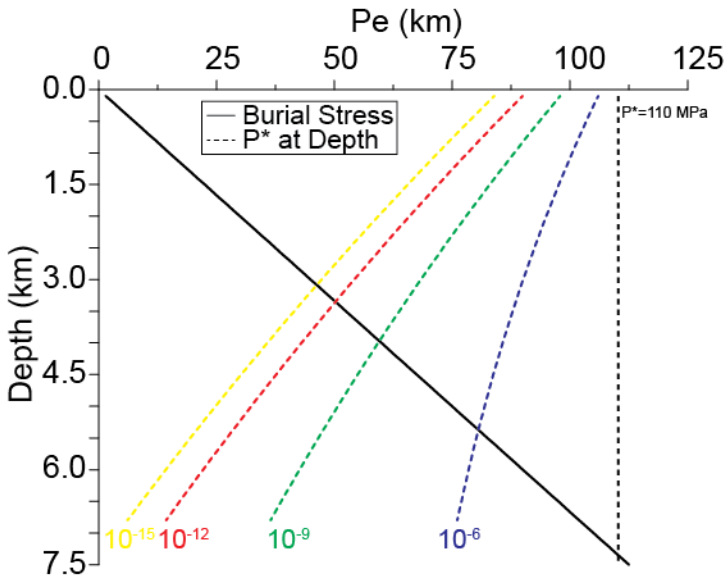

Figure 13. Predictions for sedimentary basins. A comparison of changes in burial stress, solid curve, and P*, dashed curves, at in situ conditions, plotted on axes of effective pressure (MPa) versus burial depth (kilometers). Burial stress calculated for a stress gradient of 15 MPa per kilometer. Critical pressures calculated assuming temperature gradient of 20° C per kilometer and strain rates of 10^{-15} sec^{-1}, yellow, 10^{-12} sec^{-1}, red, 10^{-9} sec^{-1}, green, and 10^{-6} sec^{-1}, blue. The dashed black curve demonstrates a constant vale of P*, 110 MPa.

133° C. The intersection points would be shallower with a higher temperature gradient, and deeper with a lower temperature gradient. This function is also calculated based on experiments saturated with deionized water. The intersection point determined here is almost half the depth that would be calculated off the standard laboratory experiment results, 7.3 km, and demonstrates the pronounced effect the coupled variables of temperature and strain rate can have on porous granular compaction. All experiments were performed with static deionized water. *Chester et al.*, [2007], demonstrated the creep of St. Peters sand is highly dependent on the chemical environment. Naturally occurring brines and flowing fluids would also act to depress P^* values, acting similar to elevated temperatures and slower strain rates. Chemical effects are beyond the scope of this study, but it is likely that combined temperature, strain rate, and chemical effects would be significant.

The depth ranges from these predictions for geologic strain rates are able to match observations of naturally consolidated sandstones. Long standing observations on diagenetically deformed sandstones attributed porosity reduction to pressure solution since HC Sorby's pioneering work in the 1860's [*Ramm*, 1992; *Tada and Siever*, 1989]. Recent observations of pressure solution structures utilizing cathode luminescence in scanning electron microscopes has demonstrated that these classic structures are actually grains that have been fractured and subsequently recemented [*Laubach et al.*, 2010; *Makowitz and Milliken*, 2003; *Milliken and Laubach*, 2000]. These observations indicate that the presence of pressure solution structures can be used to identify natural sands and sandstones that have passed through P^*. Observations of porosity trends in

sands in offshore Norway have demonstrated that at shallow depths, sands have undergone gradual porosity reduction through Regime 1 compaction: grain rearrangement, elastic deformation of grains, and only minor contributions of fracturing and ductile deformation from weaker components in the sediments [*Ramm*, 1992]. At deeper depths, 2.5 km to 3 km, there is a marked decrease in porosity due to pressure solution, which can be interpreted as the healing of fractured grains that have passed through P^*. Porosity versus depth trends show that the shallow porosity reduction can be fit with a linear trend, but with increasing depth the behavior can be fit with an exponential function due to the increased porosity reduction from grain fracturing (see Figure 2 of *Ramm*, 1992). The burial depth for geologic strain rates from this study is 3.09 km to 3.35 km for clean sands saturated with deionized water (Figure 13). Naturally occurring chemically active in situ environments would reduce this depth, but this is within the range of depths for natural sandstones especially as experiments at elevated temperature and decreased strain rates show a rounding of curves at P^*, suggesting slow fracture growth begins at stresses below P^*. Studies linking thermal maturity to porosity reductions also support the findings of this study [*Bloch et al.*, 1986; *Schmoker and Gautier*, 1988]. Thermal maturity increases with burial depth as porosity naturally decreases, but differenced in thermal maturity can also explain porosity differences for different reservoirs at similar depths [*Schmoker and Gautier*, 1988]. Increased temperatures would decrease P^*, and lead to reduced porosity for a given depth.

The reduction in P^* for quartz sand is of particular interest for unconventional reservoirs and enhanced geothermal systems, where engineering strain rates of 10^{-9} sec^{-1} are appropriate for the life of the reservoir. St. Peter sand is a common proppant material, and the grain size used is larger than that of this study [*McDaniel and Willingham*, 1978; *Syfan and Anderson*, 2011]. Many unconventional reservoirs are at or near the burial depth of 3.97 km corresponding to P^* for 10^{-9} sec^{-1} [*Blackwell et al.*, 2006; *Fisher and Warpinski*, 2011]. Proppants in situ would also be exposed to chemically active environments, from the fracturing fluids and treatments used during stimulation, the naturally occurring brines in reservoirs, and flowing fluids through the fracture network. Larger grain sizes used for proppants would also lower P^* values. This study indicates that over the life cycle of the well, it is very likely that proppant is deformed by grain fracturing and porosity collapse, reducing the permeability of the induced fracture network.

2.5. Conclusions

We conducted three different types of experiments in this study: constant plastic volume-strain rate experiments, strain rate stepping experiments, and creep compaction experiments. Quartz aggregates of St. Peter sand were deformed at four different temperatures, room temperature, 80° C, 150° C, 200° C, four different orders of magnitude consolidation strain rates, 10^{-4} sec^{-1} to 10^{-8} sec^{-1}, and creep rates as low as 10^{-11} sec^{-1}. The experiments demonstrate that the theory of parallel consolidation curves developed by Bjerrum, 1967, for normally consolidated clay rich soils, can be employed

to describe the behavior observed in this study on quartz sand. The constant plastic volume-strain rate experiments depict parallel curves for different strain rates and temperatures. Strain rate stepping experiments confirm parallel envelopes. These experiments also produce creep behavior and tertiary consolidation predicted by the parallel consolidation curve model. The plastic consolidation curves for St. Peter sand can be described by a series of parallel envelopes with two different slopes separated by the critical pressure, P^*. P^* decreases with increasing temperature and decreasing plastic volume-strain rate. Individually, increases in temperature and decreases in strain rate result in modest reductions in P^*. However, the combined effects of temperature and strain rate are substantial. P^* for room temperature experiments conducted at standard laboratory strain rates of 10^{-5} sec^{-1} for St. Peter sand is 111 MPa; P^* for room temperature experiments conducted at slow strain rates of 10^{-8} sec^{-1} is 102 MPa; P^* for 150° C experiments conducted at standard laboratory strain rates of 10^{-5} sec^{-1} is 95 MPa; P^* for 150° C experiments conducted at slow strain rates of 10^{-8} sec^{-1} is 55 MPa. The Bjerrum model allows creep experiments to interpret P^* at even slower strain rates that would be prohibitive in consolidation experiments. P^* for 150° C and strain rates of 10^{-10} sec^{-1} is 33 MPa. Extrapolating to geologic strain rates of 10^{-12} sec^{-1}, P^* at 150° C is 20 MPa. For the burial of sediments, assuming geothermal gradients of 20° C per kilometer, burial stresses of 15 MPa per kilometer, and strain rates of 10^{-12} sec^{-1}, P^* would occur at 3.35 kilometers depth. This is less than half of the 7.3 kilometers depth predicted by from the room temperature standard laboratory strain rate experiment. This demonstrates that typical experiments greatly over predict the strength of granular

material, and temperature and strain rate effects must be considered when extrapolating to in situ conditions.

3. AN EXPERIMENTAL INVESTIGATION OF BRITTLE FAILURE IN ROCK AT LOW MEAN EFFECTIVE STRESS WITH APPLICATIONS TO INDUCED HYDRAULIC FRACTURE

3.1 Introduction

In recent years the development of unconventional petroleum reservoirs has had significant impact on domestic energy production, due in large part to extensive hydraulic fracturing of previously uneconomic formations [*U.S.E.I.A.*, 2012]. The induced fracture networks enhance reservoir permeability, allowing production at reasonable rates [*Lafollette et al.*, 2012; *U.S.E.I.A.*, 2011]. The technique has been successful enough to create over a dozen major, new plays in the U.S. alone [*U.S.E.I.A.*, 2011]. Because of the rise in prominence and importance of hydraulic fracturing, there is a renewed interest in predicting the brittle behavior of rocks in tension at low mean effective stress.

The vast majority of geomechanics research has focused on the behavior of rocks loaded in compression due to the overwhelmingly compressive stress states that exist within the Earth [*Brace*, 1964; *M S Paterson et al.*, 2005]. Tensile stresses are usually limited to the very shallow crust where planar jointing of rock occurs, and deeper in the crust where geothermal, volcanic, and metamorphic processes create abnormally high fluid pressures that can exceed the minimum principal stress to drive tensile failure [*Sibson*, 1990]. The overpressurization of pore fluid in rock can create a mixed effective-stress state, i.e., a state of stress characterized by both compressive and tensile

principal effective stresses. Mixed stress states may generate hybrid fractures formed by a combination of tensile and shear mechanisms [*Hill*, 1977; *Sibson*, 1990] *Engelder*, 1999; *Ramsey & Chester*, 2004]. Hill (1977) first proposed a mechanical model to explain the high permeability channels needed to convey large volumes of fluid associated with earthquake swarms arising in geothermal and volcanic provinces: a honeycomb mesh of interlinked shear fractures and extension fractures. Physical observations from outcrops in gold quartz lode deposits confirm this fracture geometry occurs in systems with elevated fluid pressures arising from large fluxes of metamorphic fluids [*Cox et al.*, 1995; *L D Miller et al.*, 1992; *Mortimer*, 1993; *C J Paterson*, 1986; *Sibson*, 1996; 2004; *Sibson and Scott*, 1998]. Seismic observations of double couple and non-double couple sources active concurrently in earthquake swarms in geothermal and volcanic provinces demonstrate that both tensile and shear processes are active [*Foulger et al.*, 2004; *Julian et al.*, 1998; *A D Miller et al.*, 1998; *Shelly et al.*, 2013a; *Shelly et al.*, 2013b]. The physical and seismic observations provide supporting evidence that Hill's model has general applicability.

Induced hydraulic fractures in boreholes are idealized as planar wing fractures that are similar in morphology to joints, and there is evidence from observations that the idealizations are appropriate. There is also some evidence that induced hydraulic fractures do not match this idealization; instead, the induced deformation consists a large interconnected fracture network, possibly similar to the Hill type fracture meshes seen in geothermal and metamorphic provinces [*Cipolla et al.*, 2008]. Microseismic studies have shown that stimulation of a wellbore often creates a distributed cloud of seismic

events, and enhanced rates of production suggests that the diffuse cloud represents an interconnected network exposing a large volume of reservoir to the wellbore [*Cipolla et al.*, 2008]. The distributed nature of the microseismic events also indicates that the region of perturbed stress associated with hydraulic fracturing is not limited to the tip of a single fracture. Source analysis from microseismic studies have shown that double couple and non-double-couple sources are active concurrently during hydraulic stimulation, similar to the source distribution for earthquake swarms in geothermal provinces [*Busetti et al.*, 2014; *Sileny et al.*, 2009]. Physical observations of induced hydraulic fractures from coring and mineback experiments also show the complicated nature of the induced fracture networks, consisting of multiple fracture strands with an en echelon geometries and mutually cross-cutting timing relationships [*Cipolla et al.*, 2008; *N. R. Warpinski et al.*, 1993; *N.R. Warpinski and Teufel*, 1987]. Complexities in hydraulic fracturing are typically explained by the presence of natural fractures and other pre-existing heterogeneities[*Cipolla et al.*, 2008]. While this likely occurs, the similarity to natural fractures in metamorphic and geothermal provinces suggest that other factors also may contribute to fracture network complexity. Because the production of unconventional reservoirs often depends on fracture network connectivity and development of large fracture surface areas, it is vital to improve our capability to predict the extent and interconnectivity of the generated fracture network.

The similarity of induced hydraulic fracture networks to natural examples of fracture meshes in metamorphic, geothermal, and volcanic provinces, as opposed to the development of systematic joints in bedded rock, suggest that the behavior of induced

hydraulic fractures is not described by tensile failure alone, but rather a combination of extensional and shear failure that occurs in low mean effective stress states comprised of both tensile and compressive principal stress. The standard approach for defining the brittle failure behavior of rock at tensile and low mean effective stress is the Griffith criterion, which is often combined with the Modified Griffith criterion (or Coulomb criterion) to describe shear fracture under wholly compressive stress states [*Brace*, 1964; *Engelder*, 1999; *Hancock*, 1985; *Julian et al.*, 1998; *Sibson and Scott*, 1998]. Although the composite Griffith-Coulomb failure criterion successfully describes brittle failure in a qualitative sense, it is inadequate for much quantitative work [*Bobich*, 2005; *Ramsey and Chester*, 2004].

Compared to shear fracture and shear-enhanced compaction, the extension to shear fracture transition in rock has received relatively little attention in the field of experimental rock deformation. Tensile strength tests are common, but systematic investigations of failure under mixed states of stress are limited. There is some early work on Westerly granite, greywacke sandstone, quartzite, diabase, and dolomite [*Bobich*, 2005; *Brace*, 1964; *Chemenda et al.*, 2011; *Nguyen et al.*, 2011; *Schock and Louis*, 1982], and more recent work on Berea sandstone, Carrara marble, and rock analog materials [*Ramsey & Chester*, 2004; [*Bobich*, 2005; *Brace*, 1964; *Chemenda et al.*, 2011; *Nguyen et al.*, 2011; *Schock and Louis*, 1982]. The work on Carrara marble provides the best demonstration of hybrid fracture and the transition from extension fracture to shear fracture [*Ramsey & Chester*, 2004; *Rodriguez*, 2005]. The experimental observations from experiments on Berea sandstone and Carrara marble illustrate that

conventional failure criteria used for mixed stress states, such as the Griffith and modified Griffith criteria, are not capable of accurately predicting the fracture strength and fracture orientation across the transition [*Bobich*, 2005; *Ramsey and Chester*, 2004; *Rodriguez*, 2005]. Despite the compositional, mineralogical and textural differences in lithological differences between Berea sandstone and Carrara marble, the rocks have similar tensile strength, T_O, and uniaxial compressive strength, C_O, and the rocks are characterized by similar failure envelopes and changes in fracture mode across the extension to shear fracture transition. These findings lead to the hypothesis that the general characteristics of brittle failure may be independent of lithology and may scale with common rock mechanical properties such as C_O and T_O.

In this paper, we present the results of rock deformation experiments on four distinct rocks: Berea sandstone, Carrara marble, Indiana limestone, and Kansas chalk. The rocks were deformed in axisymmetric triaxial extension over a range of confining pressure, P_C, that spans the extension to shear-fracture transition. The rock types represent a spectrum of intrinsic characteristics: sedimentary and crystalline rock types; clastics and carbonates; high and low porosity; equant pores and cracks; different C_O and T_O. The experiment results are consistent with the hypothesis that brittle failure across the extension to shear transition at low mean stress is independent of lithology and scales to strength of the material. We use the universal failure characteristics and scaling relationships for the extension to shear transition to address uncertainties in fracture processes and fracture network development in unconventional reservoirs subjected to induced hydrofracture.

3.1.1. Previous Work

The Brazilian test, which is used to create a tensile stress, is a common rock mechanics procedure to determine tensile strength; however, creating a tensile stress along with an approximately homogeneous mixed stress state to investigate fracture is technically challenging. Due to the highly heterogeneous nature of rocks, it is difficult to apply a direct tensile force to a sample and achieve reproducible results [*Jaeger et al.*, 2009]. Better success is achieved by deforming samples in a triaxial-extension stress state, in which the confining pressure is the greatest principal stress. By reducing the diameter in the central portion of a cylindrical sample (i.e., creating a neck), an axial tensile stress can be developed during triaxial extension within an otherwise compressive stress state [*Brace*, 1964; *Schock and Louis*, 1982]. Using a constant neck diameter with small radius at the transition from neck to shoulder, the sample behavior is controlled by the stress concentration at the transition, which can dictate fracture orientation [*Nguyen et al.*, 2011; *Schock and Louis*, 1982]. In contrast, using a neck with a single large and constant radius of curvature to form a perfectly continuous neck and shoulder, a reliable and reproducible fracture strength and fracture orientation across the extension to shear fracture transition in achieved [*Bobich*, 2005; *Ramsey and Chester*, 2004].

Triaxial extension experiments on Berea sandstone and Carrara marble employing the single radius notch-cut samples demonstrate that there is a smooth, systematic transition in fracture behavior at low mean stresses. Differential stress at failure increase monotonically with P_C across the transition; fracture angles (maximum angle between the fracture plane and the plane normal to the sample axis) are

approximately zero for extension fractures at the lowest P_C, then increase linearly with increasing P_C through the transition through hybrid fracture to shear fracture [*Bobich*, 2005; *Ramsey and Chester*, 2004]. Within the extension fracture regime, the axial stress at failure becomes increasingly negative (greater tension) with increasing P_C before reversing the trend to transition to wholly compressive stresses. The failure behavior can be described using two different linear fracture envelopes. The intersection of the two envelopes corresponds to the change from extension fracture to hybrid fractures [*Bobich*, 2005]. The stress at failure and the corresponding fracture angles are not adequately described by either the Griffith or modified Griffith criteria.

Observations of fractured Berea and Carrara samples from across the transition display key characteristics that correlate well with fracture angle. Laser profilometry scans of deformed Carrara marble samples show that the fracture surface morphology changes with confining pressure [*Rodriguez*, 2005]. For extension fractures, the sample faces are rough and isotropic. For hybrid fractures, the sample faces have a tread-riser geometry formed from en echelon extension fractures (treads) linked by shear fracture segments (risers). In these samples surface roughness is greater in the slip direction than perpendicular. For the shear fractures formed under wholly compressive stress, the surfaces are smoother in the slip direction [*Rodriguez*, 2005]. Visual observations correlate with the laser profile scans: tensile fractures lack shear indicators, hybrid fractures have intermittent patches of gouge that increase in extent with confining pressure, and shear fractures are covered with gouge [*Bobich*, 2005; *Rodriguez*, 2005]. Microstructural observations of deformed Carrara marble demonstrate clear relationships

between induced damage and confining pressure [*Rodriguez*, 2005]. The microfracture density and extent increases with P_C, and the extension fractured samples display very few microfractures. Although microstructures of the Berea samples were not documented, acoustic emission counts for prior to the development of a through going fracture, an indicator of microfracture damage, display a systematic increase with P_C [*Bobich*, 2005]. This also corresponds to increase in inelastic strain prior to failure for both Berea sandstone and Carrara marble [*Bobich*, 2005; *Rodriguez*, 2005]. The acoustic emission data indicate that the microcracks observed in Carrara marble likely occurred prior to failure [*Bobich*, 2005; *Rodriguez*, 2005].

Although the past work on Berea sandstone and Carrara marble is quite comprehensive, additional experiments were conducted on these rocks in order to 1) confirm reproducibility between the present and past results, and 2) determine the radial and avail strain components during loading to failure in the local region where failure occurs in the neck of the sample.

3.2. Methods

3.2.1. Description of Rock Types and Sample Preparation

Four different rock types were used in this study, Berea Sandstone, Carrara marble, Indiana Limestone, and Kansas Chalk (Table 5). The Berea sandstone samples are from a single block from the Cleveland Rock Quarry in Ohio. Previous studies on samples from this local have shown that the grain size, porosity, and mineralogy are

Rock Type	Composition	Porosity (%)	Grain Size (μm)	Compressive Strength (MPa)	Tensile Strength (MPa)	Critical Pressure (MPa)
Berea Sandstone	[1]70-85% quartz, 20-25% feldspar, dolomite, rutile, zircon, and kaolinite	[2]16-19	[2]185	[3]100	[4]4.8	[1]380
Carrara Marble	[5]~98% calcite	[5]1	[5]250-350	[3]85	[4]7	---
Indiana Limestone	[6]~97% calcite	[6]15-20	[6]300	[3]53	[4]0.85	[6]60
Kansas Chalk	[7]~99% calcite	[7]30	[7]0.2-.055	[3]8.5	[4]0.22	[8]~14-20

[1] [*Bernabe and Brace*, 1990; *Hart and Wang*, 1995; *Menendez et al.*, 1996; *Zhang et al.*, 1990a]
[2] [*Bobich*, 2005; *Choens and Chester*, 2014]
[3] *Unpublished Class Research*
[4] *This study*
[5] [*Ramsey and Chester*, 2004]
[6] [*Churcher et al.*, 1991; *Hart and Wang*, 1995; *Ji et al.*, 2012; *Vajdova et al.*, 2004]
[7] [*Pooladi-Darvish and Firoozabadi*, 2000; *Spinler et al.*, 2000]
[8] *Based on similar chalks in [Vajdova et al., 2004]*

Table 5. Mineraliogies and rock properties of the four different rock types.

comparable to other published measurements for Berea (Table 5) [*Bernabe and Brace*, 1990; *Bobich*, 2005; *Hart and Wang*, 1995; *Menendez et al.*, 1996; *Zhang et al.*, 1990a]. In general, the samples consist of subangular, well-sorted grains composed of 75-80% quartz, 20-25% feldspar, and lesser amounts of dolomite, rutile, zircon, kaolinite, and some secondary minerals [*Menendez et al.*, 1996; *Zhang et al.*, 1990a]. Dolomite grains and cement (up to 400μm) are distributed throughout the granular mass. Porosity measurements attained from mass differences between dry samples and samples saturated with alcohol or distilled waters range from 16-19%. The Schwawrtz-Saltykov method was used to determine the grain size distribution from measurements of grain diameter in plane petrographic sections; the mean diameter is 185 μm [*Hillard and Lawson*, 2003; *Zhang et al.*, 1990b]. Bedding laminae, with spacing around 0.5 mm, are defined by concentration of mafic minerals visible on the hand sample scale. Previous studies on Berea have shown that the laminations influence fracture behavior [*Herrin*, 2008]. Samples were cored parallel to the laminations to minimize bedding effects on tensile fracture orientation.

Carrara marble samples were taken from a single block from the Lorano Bianco Carrara marble of Italy. This marble is nearly pure calcite and has less than 1% porosity, with a weak crystallographic preferred orientation. The grain sizes range from 250-355 μm [*Rodriguez*, 2005]. The undeformed marble displays occasional thin mechanical twins and sporadic, intragranular, cleavage microfractures that are a few microns in length [*Fredrich et al.*, 1989; *Pieri et al.*, 2001; *Rodriguez*, 2005]

Indiana limestone samples were taken from a single block of limestone. Indiana limestone is over 97% calcite with 15 to 20% porosity. It is a calcite-cemented grainstone, where the grains can be over 300 μm in diameter [*Churcher et al.*, 1991; *Ji et al.*, 2012; *Vajdova et al.*, 2004]. Classified as a freestone for architectural purposes, the rock is homogeneous and contains no inherent parting planes in the material.

Kansas chalk samples were taken from a 20 inch diameter core purchased from TerraTek. The unit is a member of the Upper Cretaceous Niobrara Formation. This chalk is very pure, 99% calcite, with high porosity at 30% [*Pooladi-Darvish and Firoozabadi*, 2000]. Grain sizes are very small, 0.2 to 0.55 μm in diameter. Due to similarities in capillary behavior, Kansas chalk has long been used as an analog material for North Sea reservoir rocks [*Pooladi-Darvish and Firoozabadi*, 2000; *Spinler et al.*, 2000]. Additionally, the Niobrara Formation is now an active unconventional reservoir itself.

The tests utilize the specialized sample geometry, the notch-cut, or 'dogbone' geometry used in previous studies [*Bobich*, 2005; *Ramsey and Chester*, 2004]. The sample geometry and jacket assembly is shown in Figure 14. To create the dogbone geometry, the samples are ground on a microlathe mounted on a stationary surface grinder to create the neck of the sample. 50 mm diameter cores are mounted on the microlathe with the cylindrical axis perpendicular to the grinding wheel. The samples are ground down slightly, to a 47 mm diameter to ensure that the samples are perfectly round and the axis is true to the microlathe. To cut the neck, the microlathe is turned parallel to the grinding wheel. The diameter of the grinding wheel determines the radius

of curvature of the neck, 88 mm. After the neck is ground, the samples are cut to length and the ends are ground perpendicular to the axis and parallel to each other. The final dimensions of the sample are 102 mm in length, 47 mm diameter at the shoulder, and 30 mm diameter at the neck.

Maintaining jacket integrity pre and post failure while still transmitting the pressure from the confining medium and minimizing jacket strength necessitates a three layer jacketing procedure (Figure 14). The first layer is a 0.2 mm thick latex sheeting wrapped directly onto the sample. Previous studies have demonstrated that the latex jacketing is extremely weak, and will not affect the mechanical behavior of the sample while still protecting it from the next layer, placticene modeling clay [*Bobich*, 2005; *Ramsey and Chester*, 2004]. The clay is used to fill the notch in the sample and reestablish an approximate cylindrical geometry; because clay is extremely weak under pressure, it transmits the confining pressure to the neck of the sample while mechanically decoupling the jackets. The clay also prevents the edges of the shoulders from cutting the outer jacket. The assembly is isolated from the confining fluid by a layer of heat shrink polyolefin tubing sealed at the end-caps with nickel-chrome tie-wires. The tie-wires are coated with a layer of flexible UV cure epoxy for additional protection. Berea sandstone and Carrara marble samples are instrumented with strain gages; details on strain gage installation is presented in a separate paper. Indiana limestone and Kansas chalk are deformed without instrumentation to ensure the gages do not affect fracture development and strength, particularly because these rocks are considerably weaker than the sandstone and marble. After completing a few preliminary

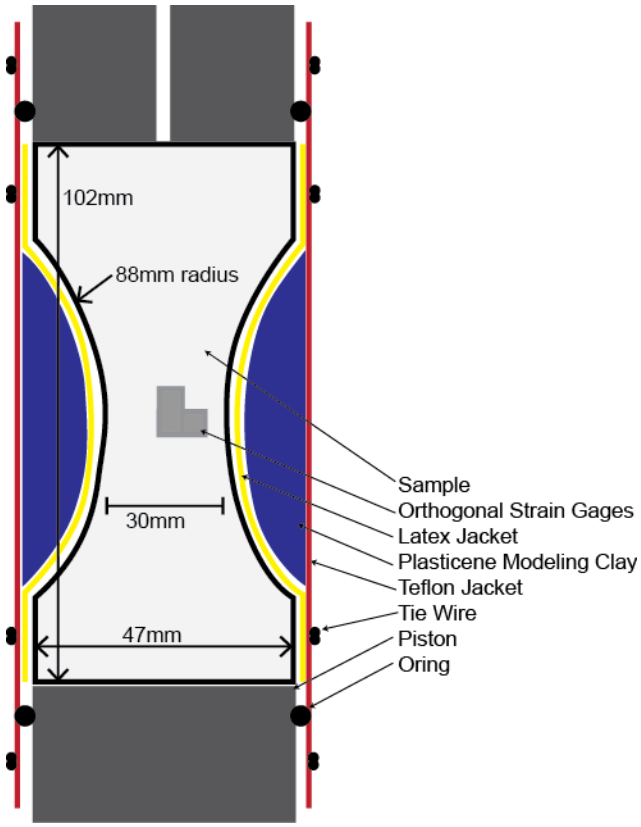

Figure 14. Dogbone sample geometry and jacket assembly. Samples are 30 mm in diameter at the neck, 47 mm in diameter at the shoulder, 102 mm in length, and the radius of curvature for the neck is 88 mm. Samples are wrapped in a layer of latex sheeting, and the neck is filled with plasticene modeling clay. The sample is jacketed with Teflon. Berea sandstone and Carrara marble samples have strain gages affixed on the neck of the sample, the wires are routed out underneath the jacket and through a pore pressure port in top piston.

tests on the weaker materials, it was thought that slight misalignments in the axial load column of the materials-testing machine used for this study may have contributed to poorer data quality at low confining pressures. Accordingly, additional actions were employed to improve uniformity and alignment of loading. Specifically, the ends of the samples for Indiana limestone and Kansas chalk were coated with a stearic acid and Vaseline mixture and copper shims [*Labuz and Bridell*, 1993]. Additionally, Kansas chalk samples were deformed with lead shims in the axial column and a spherical seat between the platen and the piston. A sample of Indiana limestone was deformed at 25 MPa P_c with the same loading geometry as the chalk for comparison.

3.2.2. Experimental Procedure

All experiments were conducted at Sandia National Laboratories at the geomechanics research laboratory using a 1 MN servo-hydraulic load frame. The machine is capable of independent confining and pore pressure control, and contains electrical feed-throughs for sample instrumentation. In this machine, Isopar, an isoparaffinic fluid solvent, is the confining medium. Samples are deformed at an axial strain rate of 10^{-5} per second. Axial stress is measured with an external load cell capable of 900 kN calibrated to 0.4% of the indicated reading. The confining pressure is measured with a 30000 psi transducer calibrated to 0.3% of the indicated reading. Axial displacement is measured with ±76 mm LVDT calibrated to 0.15% of the indicated reading. Seal friction is corrected using calibration experiments conducted at each confining pressure where the piston displacement was cycled to establish hysteresis.

The arrangement of the sample assembly in the testing machine requires that the axial stress and confining pressure must be controlled independently. Samples were initially loaded to 1 MPa axial stress before confining pressure was added. The axial stress was increased at the same rate as the confining pressure, maintaining a 1 MPa differential stress on the sample. This small load ensures that the sample assembly remained in contact with the piston during the hydrostatic loading. When the desired confining pressure was reached, the axial stress was decreased and the piston was extended at a constant rate while the confining pressure was held constant.

In triaxial extension the confining pressure is the greatest principal stresses, σ_1 and σ_2, and the axial stress is the least principal stress, σ_3. Due to the difference in areas between the shoulders and necks of the samples, a tensile stress may be generated locally in the neck of the sample during extension. The tensile stress is equal to the change in axial stress subtracted from the confining pressure, with the calculations based on the neck diameter of the sample. For Berea sandstone and Carrara marble samples instrumented with strain gages, the change in neck diameter was monitored. For Indiana limestone and Kansas chalk, the neck diameter is assumed constant for stress calculations. Confining pressures of 10 - 150 MPa were used for Berea sandstone and Carrara marble. Indiana limestone samples were deformed at 5 - 90 MPa confining pressure. Kansas chalk samples were deformed at 1 - 22.5 MPa confining pressure. Samples were deformed dry and vented to the atmosphere. The linear portions of the axial-stress versus axial-strain curves were used to calculate the elastic response of the sample, similar in methodology to determining the tangent modulus. The external

measurements average the response over the entire length of the sample and across the piston sample interfaces, so the term apparent stiffness is used in this paper.

In this paper we adopt the convention that compressive stress and contractive strains are positive. We will note the maximum and minimum principal compressive stresses by σ_1 and σ_3, respectively. For triaxial extension experiments, the axial stress, σ_a, is the minimum principal stress, and the confining pressure, P_C, is the maximum principal stress. The mean stress, $(2\sigma_1 + \sigma_3) / 3$, P, and the differential stress, $\sigma_1 - \sigma_3$, Q.

3.3. Results

All samples failed by the development of a through going fracture, the characteristics of which changed across the extension to shear transition. The overall changes in fracture behavior of the four different rocks across the transition is similar in many regards, despite differences in absolute strength, mineralogy, grain size, and porosity (Table 5); however, there are some important differences in mechanical properties. The relative differences in properties of the rocks can be illustrated by comparing mechanical response to similar loading conditions. Figure 15 illustrates the relative mechanical response of the rocks at the loading condition somewhat analogous to an unconfined compressive strength, UCS, test. A representative experiment is plotted for each rock type at or closely approximating the loading condition of σ_3 equal to zero (i.e., approximately unconfined); a triaxial extension test in which σ_3 is zero at failure is referred to as an unconfined extensional strength, UES, test. The difference between a UES and UCS test is the magnitude of σ_2 at failure; in a UCS test $\sigma_2 = \sigma_3 = 0$, and in a

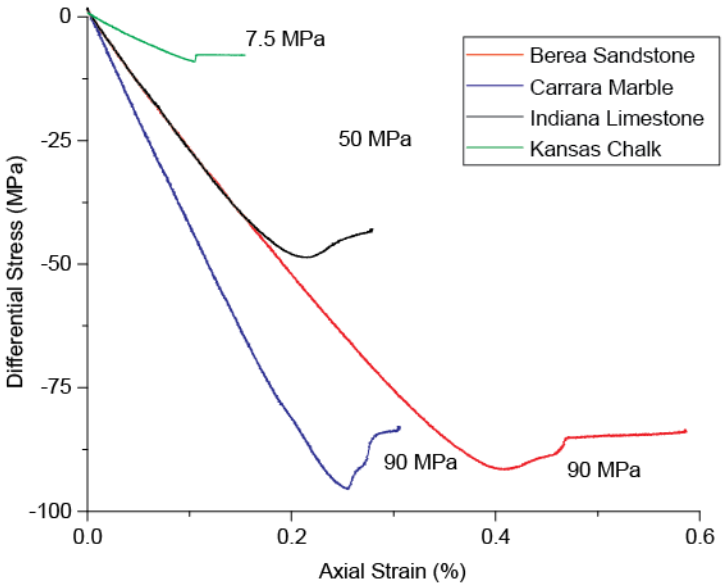

Figure 15. A comparison of the four different rock types for experiments at or nearest to the UES for differential stress (MPa) versus axial strain (%). Berea sandstone deformed at 120 MPa, in red; Carrara marble deformed at 120 MPa in blue; Indiana limestone deformed at 50 MPa in black; Kansas chalk deformed at 12.5 MPa in green.

UES test $\sigma_2 = \sigma_1 = P_C$. As shown in Figure 15, there is a wide range in strength for the four different rock types. In general, the higher the porosity, the weaker the sample, and calcite dominated rocks are weaker than quartz dominated rocks. Berea sandstone and Carrara marble have a similar strength in a UES test, largely because the combine effects of mineralogy and porosity cancel (Figure 15). Indiana limestone is the next strongest material, at less than half the strength, with the same porosity as Berea sandstone and a calcite dominated lithology. Kansas chalk is the weakest material, with the highest porosity of the four rocks. Differences in pore structures are also reflected in this weakening trend. Berea is a granular material with strong grains and intergranular porosity; Indiana limestone is a granular material with weaker grains, with some intragranular porosity; and Kansas chalk is a granular material where the grains have high amounts of intragranular porosity [*Haddadi*, 2013; *Hattin*, 1981; *Ji et al.*, 2012]. Differences in apparent stiffness between the different rock types mirror the differences in porosity. The lowest porosity rock type, Carrara marble, has the highest apparent stiffness. Indiana limestone and Berea sandstone have similar porosities and similar apparent stiffnesses. Kansas chalk has the highest porosity, and the lowest apparent stiffness. Yielding and failure manifests differently in the different rock types. Carrara marble has very little post yield strain, Indiana limestone and Berea sandstone have strain softening post peak stress prior to fracture. Kansas chalk does not appear to accumulate inelastic strain prior to failure, but this was not independently confirmed (e.g., by cyclic loading prior to fracture).

3.3.1. Previously Tested Materials: Berea Sandstone and Carrara Marble

The previous work on Berea sandstone and Carrara marble demonstrated new phenomena in the extension to shear fracture transition, as well as established sample geometries and testing methodology that allowed for accurate and reproducible result [*Bobich*, 2005; *Ramsey and Chester*, 2004; *Rodriguez*, 2005]. The experiments performed in this study are conducted on a different testing apparatus than the previous work, and with a slightly modified geometry. This study duplicated key experiments on Berea sandstone and Carrara marble to establish the reproducibility using a different testing system as compared to the previous work. In addition, the samples in the present work were instrumented with strain gages to determine local strains in the neck region.

The axial stress at failure for Berea sandstone and Carrara marble in the present experiments agrees well with the previous work (Figure 16a, b) [*Bobich*, 2005; *Ramsey and Chester*, 2004]. At the lowest confining pressure, $P_C = \sigma_1$, the sample fails in extension with a negative (tensile) axial stress, $\sigma_3 < 0$. With increasing σ_1, the σ_3 at fracture becomes increasingly tensile, i.e., the tensile strength of the sample increases with P_C. Similarly, the magnitude of extensional axial strain up to fracture also increases with P_C. For both Berea and Carrara, the relationship between the change in σ_3 with increase in σ_1 reverses at a P_C = 50 MPa. It is noted, however, that the differential stress at fracture monotonically increases with increase in P_C. The stress at fracture is well described in stress space (e.g., σ_1 vs σ_3) by two linear relationships. The stress at fracture determined from present experiments agrees, allowing for sample to sample variation, with the relationships determined from the previous work.

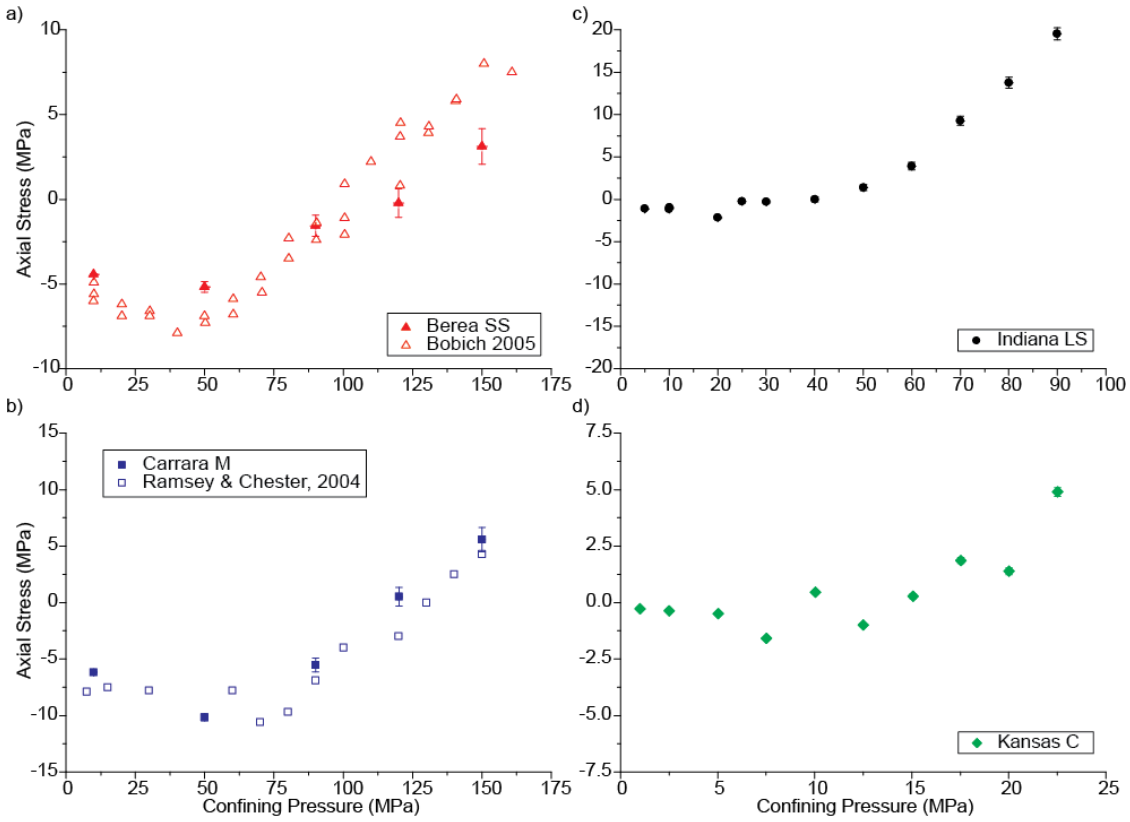

Figure 16. Failure stength for the four different rock types. Results from triaxial extension experiments on Berea sandstone, Carrara marble, Indiana limeston, and Kansas chalk. Axial stress versus confining pressure. Results from this study are solid symbols; resulst from previous work, open symbols. (a) Results for Berea sandstone. (b) Results for Carrara marble. (c) Results for Indiana limeston. (d) Results for Kansas chalk.

The results for Carrara marble agree with the magnitude of the previous failure strengths, as well as the overall trend [*Ramsey and Chester*, 2004]. The failure strengths for Berea sandstone agree well with the magnitude of the previous results, but the strengths at the higher P_C are somewhat lower than determined in the previous work [*Bobich*, 2005]. The reduced strength could be due to minor variations in the rock material because although the samples come from the same quarry, different blocks were used in the two studies; or, it could just reflect an apparent difference resulting from less data in the present work.

The orientation of fractures in Berea sandstone and Carrara marble with change in PC determined in the present experiments agrees well with the previous findings (Figure 17a, b) [*Bobich*, 2005; *Ramsey and Chester*, 2004]. At the lowest confining pressures tested, the samples fail by a single fracture oriented at a low angle to the plane normal to the σ_3 direction. As the confining pressure increases, the fracture angle remains low or decreases slightly; however, at a P_C = 50 MPa the fracture angles increase linearly with P_C. Thus, fracture angle can be described by two linear relationships with respect to P_C, similar to the fracture strength data. The intersection of the linear relationships for both strength and fracture angle with respect to stress occur at the same P_C (Figure 16 and Figure 17a, b). At the same confining pressure where the failure strength changes behavior, there is a linear increase in fracture angle Figure 16. The behavior can be described by two linear segments.

In general, the present experiment results on Berea and Carrara duplicate the findings of previous work with respect to stress at failure and fracture angle. For Carrara

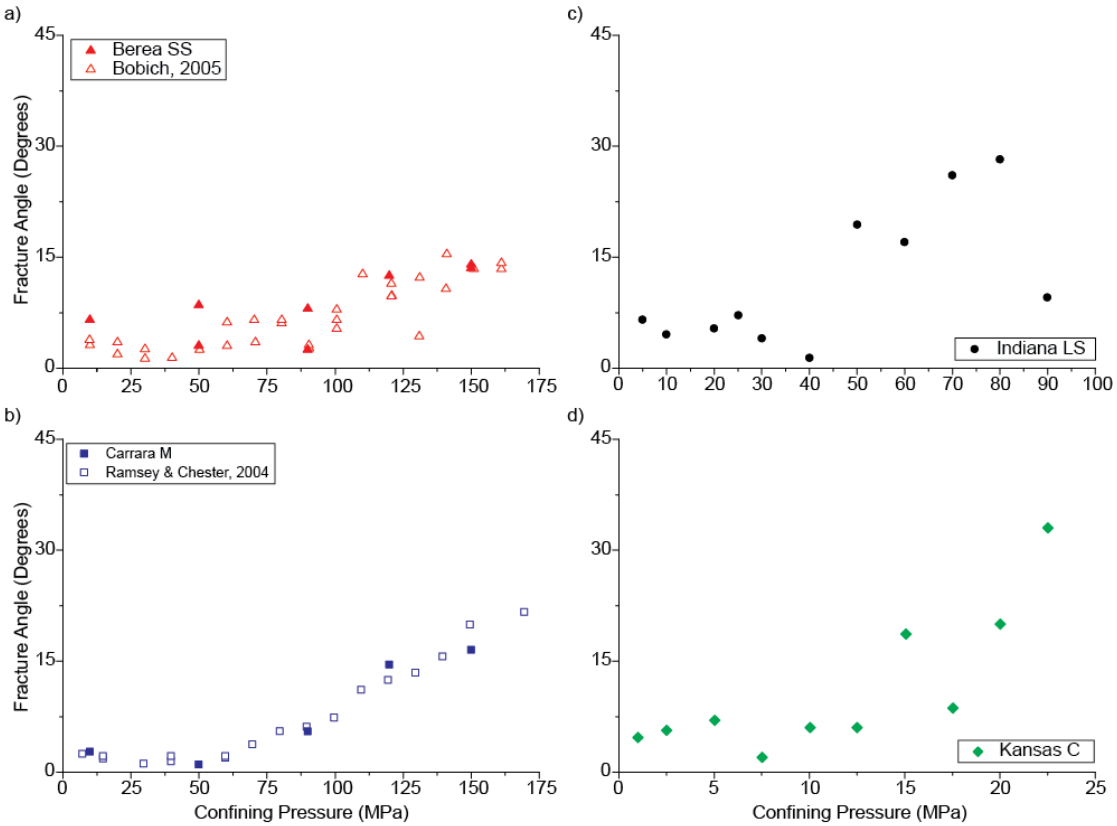

Figure 17. Changes in fracture angle with confining pressure. Results from Berea sandstone, Carrara marble, Indiana limestone, and Kansas chalk. Results from this study are solid symbols; results from previous work, open symbols. (a) Results for Berea sandstone. (b) Results for Carrara marble. (c) Results for Indiana limestone. (d) Results for Kansas chalk.

marble, the results are nearly an exact replication of the previous work [*Ramsey and Chester*, 2004]. For Berea sandstone, the present work shows somewhat less distinct trends in strength and fracture angle then shown by past work. The less-distinct trends could simply reflect sample to sample variation and relatively few data in the present work. Minor variation in the Berea samples is likely because even though the Berea samples come from the same quarry, different quarried blocks were used for the two studies. In the case of Carrara, marble, the rock is extremely uniform and samples for both studies came from a single quarried block. Given the agreement for Carrara marble, it would appears that any disagreement in between studies should not be attributed to the testing machines, and that the new results for other rock types should be directly comparable with previous work. One noteworthy observation is that in the previous work, fractures nearly always formed in the minimum diameter region of the necked samples. In the present study the samples did not always fracture at the same location, particularly at low confining pressures. In this case several samples fractured at a location roughly one third of the length of the neck. Initially this was thought to be due to sample heterogeneities or strain gage effects, but similar behavior in Indiana limestone (without strain gages) suggests that misalignment in the loading column was causing the fractures to occur outside the minimum diameter region of the neck. Accordingly, additional steps were taken to alleviate off axis loading in the weaker materials. Nonetheless, the reproducibility of failure strength and fracture angle in Berea sandstone and Carrara marble suggest the off-axis loading primarily influenced the fracture initiation point, not the overall behavior.

Additional agreement between present and past results can be seen in the differential stress versus axial strain plots for Berea sandstone and Carrara marble (Figure 18). The pre- and post-fracture behaviors are very similar. Both Berea and Carrara show increased pre-fracture yielding with increasing confining pressure. The rounding of the axial stress – strain curves at yielding for Berea is observed in this study and the previous work, and produce roughly equivalents amount of inelastic strain [*Bobich*, 2005]. Similarly, the plateau in differential stress prior to fracture at high confining pressures for Carrara marble is observed in this study and previous work; the experiments also show similar magnitudes of post yield strain prior to fracture [*Ramsey*, 2003]. Microstructural investigations have documented mechanical twinning is active at the experimental conditions that produce the plateaus in strength [*Rodriguez*, 2005]. Both rock types in both studies display increases in apparent stiffness with increasing confining pressure. One apparent difference between studies is the apparent stiffness at the onset of differential loading. However, this effect is actually caused by differences in the design of the loading column in the two machines employed. In the machine employed for the previous work, the differential axial stress is generated independent of the total stress, whereas in the machine for the present work the total axial stress and the P_C are generated independently. This results in the axial loading column being more compliant at the onset of extension and relatively stiffer at the conditions of fracture in the previous work, whereas in the present machine the axial loading column is very stiff at the onset of extension, but relatively compliant once axial stress approaches zero, as occurs during fracture of the sample during triaxial extension at low P_C.

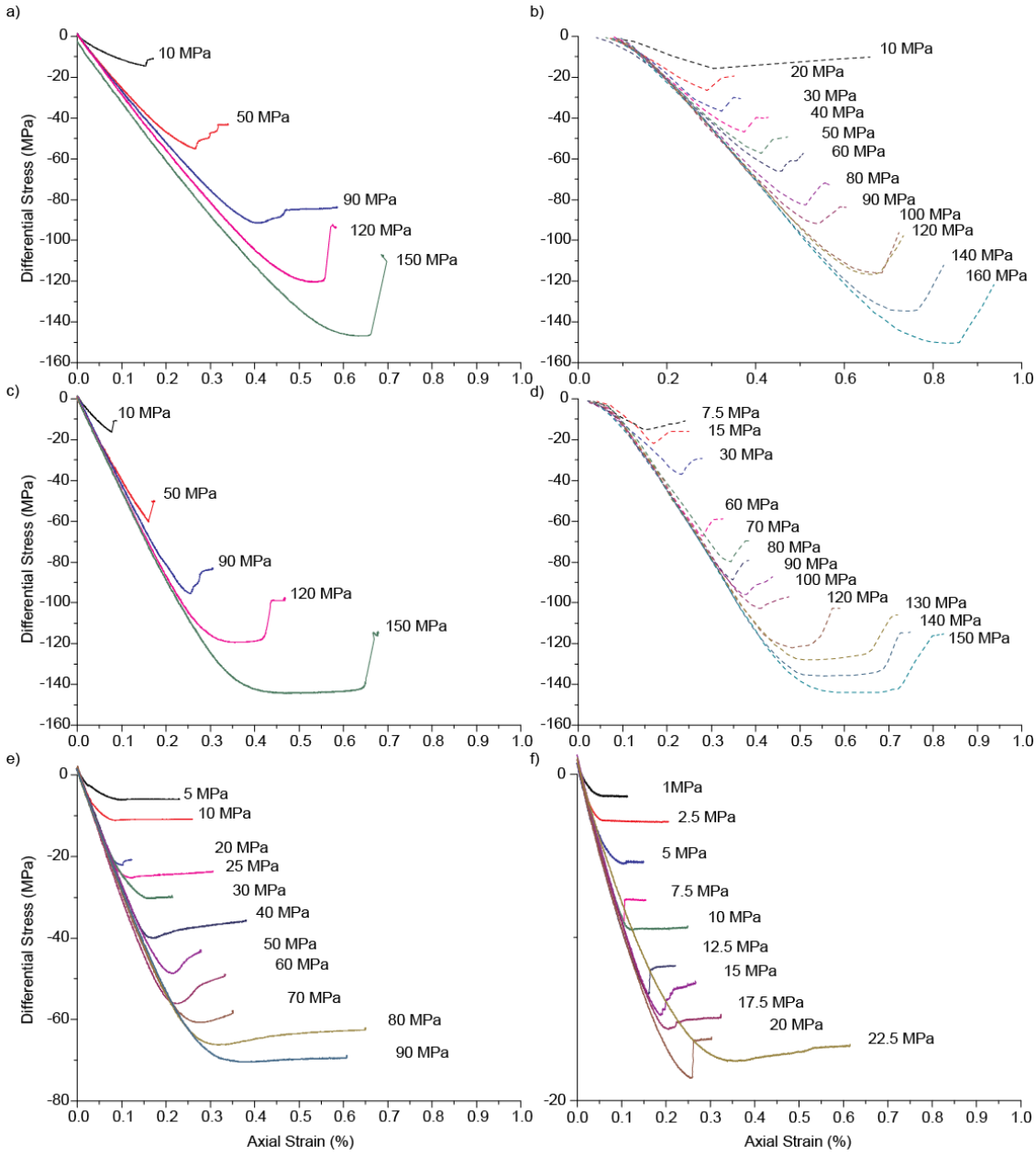

Figure 18. Mechancial response comparison. Results from triaxial extension experiments on Berea sandstone, Carrara marble, Indiana limestone, and Kansas chalk from this study, solid curves, and previous work, dashed curves. Differential stress versus axial strain, measure externally. (a) Results for Berea sandstone. (b) Results for Bobich 2005. (c) Results for Carrara marble. (d) Results for Ramesy 2003. (e) Results for Indiana limestone. (f) Results for Kansas chalk.

3.3.2. New Material: Indiana Limestone and Kansas Chalk

3.3.2.1. Indiana Limestone

Indiana limestone is well-tested rock mechanics standard; it has a UCS less than half of Berea sandstone and Carrara marble (Table 5). Indiana limestone demonstrates similar relationships with P_C as Berea sandstone and Carrara marble, but over a lower range of P_C. The differential stress and axial strain at fracture increases with increasing P_c (Figure 18). At the lowest P_C of 5 MPa, the sample has low stiffness, very weak, and shows very little plastic strain prior to failure. With increasing P_C, there is an increase in apparent stiffness and inelastic strain prior to failure (Table 6). Starting at 20 MPa P_C, there is a small but noticeable increment of plastic strain as the sample yields prior to a stress drop. At 40 MPa P_C, the sample displays strain softening associated with the development of the through going fracture, and noticeable stress drops are observed with additional increase in P_C. At 70 MPa P_C, there is strain softening post failure without a clear stress drop associated with fracture, and the experiments performed at 80 MPa and 90 MPa P_C are mechanically ductile as well.

The axial stress at failure for the Indiana limestone samples is shown in Figure 16. The relationship is similar to that of Berea sandstone and Carrara marble. At 5 MPa P_C, the sample fails with a small negative axial stress. The axial stress is constant up to confining pressures of 40 MPa; except for a slight increase in the tensile strength for the sample at 20 MPa P_C. Starting at 50 MPa P_C, the axial stress at failure is positive. With increasing confining pressure, there is a linear increase in axial stress at failure. Similar

Berea Sandstone

Confining Pressure (MPa)	Axial Stress (MPa)	Differential Stress (MPa)	Fracture Angle (Degrees)	Apparent Stiffness (MPa)
10	-4.4	-14.5	6.5	1.5E+04
50	-5.2	-55.2	3.0	2.5E+04
90	-1.6	-91.6	8.0	2.6E+04
120	-0.2	-120.3	12.5	2.8E+04
150	3.1	-146.9	14.0	2.8E+04

Carrara Marble

Confining Pressure (MPa)	Axial Stress (MPa)	Differential Stress (MPa)	Fracture Angle (Degrees)	Apparent Stiffness (MPa)
10	-6.2	-16.2	2.8	2.7E+04
50	-10.2	-60.2	1.0	4.1E+04
90	-5.5	-95.6	5.5	4.3E+04
120	0.5	-119.5	14.5	4.5E+04
150	5.6	-144.4	16.5	4.5E+04

Indiana Limestone

Confining Pressure (MPa)	Axial Stress (MPa)	Differential Stress (MPa)	Fracture Angle (Degrees)	Apparent Stiffness (MPa)
5	-1.1	-6.2	6.5	1.6E+04
10	-1.2	-11.2	4.5	2.4E+04
20	-2.2	-22.2	5.3	2.7E+04
25	-0.3	-25.3	6.7	2.9E+04
30	-0.3	-30.3	4.0	2.8E+04
40	0.0	-40.1	1.3	2.9E+04
50	1.4	-48.7	19.3	2.8E+04
60	3.9	-56.1	17.0	3.2E+04
70	9.3	-60.7	26.0	3.1E+04
80	13.7	-66.3	28.2	2.9E+04
90	19.5	-70.5	9.5	2.9E+04

Kansas Chalk

Confining Pressure (MPa)	Axial Stress (MPa)	Differential Stress (MPa)	Fracture Angle (Degrees)	Apparent Stiffness (MPa)
1	-0.3	-1.3	4.7	6.1E+03
2.5	-0.4	-2.9	5.7	9.4E+03
5	-0.5	-5.5	7.0	9.7E+03
7.5	-1.6	-9.1	2.0	1.1E+04
10	0.5	-9.6	6.0	1.0E+04
12.5	-1.0	-13.5	6.0	1.0E+04
15	0.3	-14.8	18.7	1.0E+04
17.5	1.9	-15.7	8.7	1.0E+04
20	1.4	-18.6	20.0	1.0E+04
22.5	4.9	-17.6	33.0	8.6E+03

Table 6. Experimental results for the four rock types.

to Berea sandstone and Carrara marble, the data can be described by two linear relations in stress space.

The fracture angles for Indiana limestone display a similar relationship with confining pressure as Berea sandstone and Carrara marble (Figure 17). For P_C up to 40 MPa, the fracture angles are low values, below 7.5°. Similar to Berea sandstone and Carrara marble, the fractures angles slightly decrease with increasing confining pressure. Above 40 MPa P_C, there is a linear increase in fracture angle as the behavior transitions to shear loading. There is a jump in fracture angle from 40 MPa to 50 MPa P_C, but this could be due to the fact that the 50 MPa test sample failed by the formation of a conjugate shear fracture (Figure 19). The behavior can be described by two linear relationships. At 90 MPa, there is a decrease in fracture angle that is apparent disagreement with the previous experiment. After unloading, the sample was intact. It was separated only with physical force, likely indicating the observed failure surface does not reflect the fracture face formed at P_C.

The deformed samples of Indiana limestone are shown in Figure 19. All of the samples deformed at P_C equal to or greater than 40 MPa fractured in the middle of the sample. At 30 MPa P_c and below, all of the samples fractured outside of the middle of the neck except for the sample deformed at 25 MPa P_c, which fractured in the middle. The location of the non-centered fractures occurred at roughly one third of the neck length, similar to what was observed in the Berea sandstone and Carrara marble samples. The experiment at 25 MPa P_c was performed with additional preparations to correct for suspected load-axis misalignment effects. The failure strength, fracture angle, and

a)

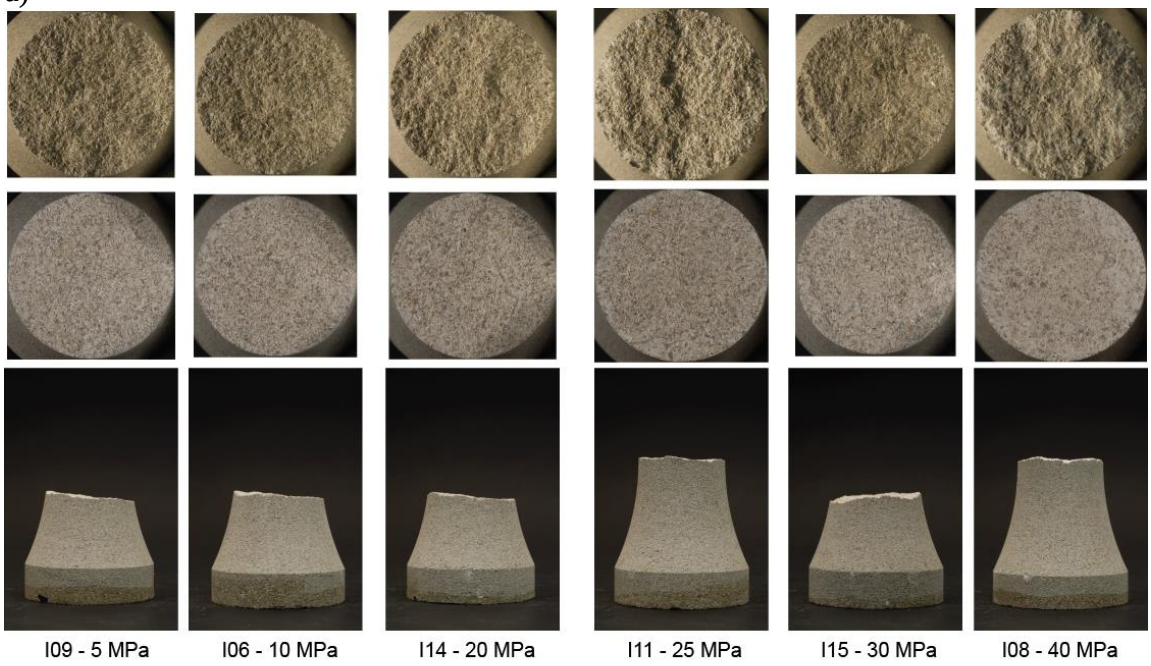

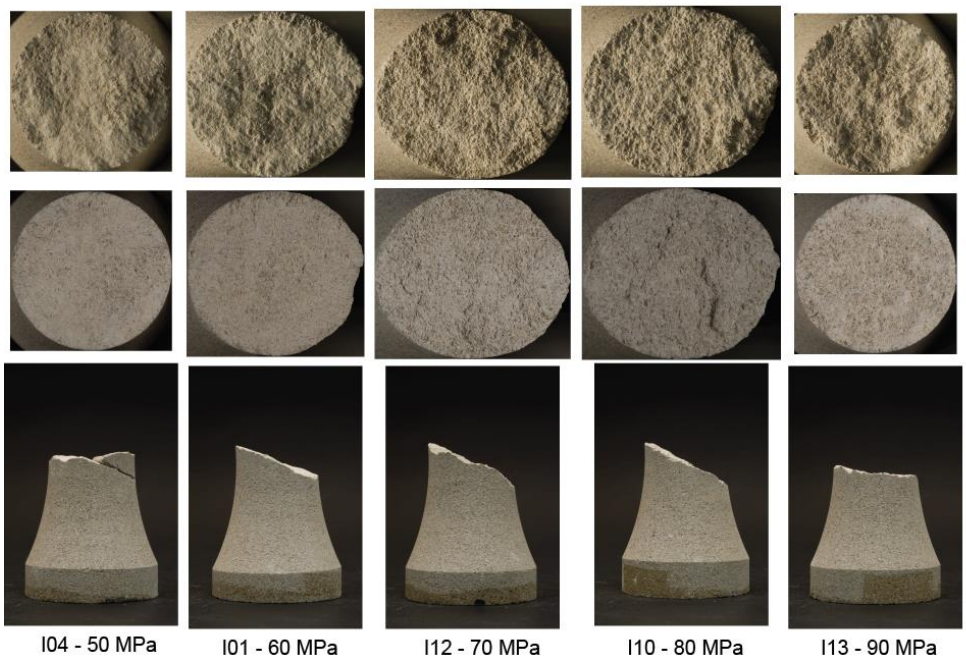

Figure 19. Sample pictures. Photographs of the fracture face and profile for a) Indiana limestone, b) Kansas chalk. Samples are annotated with confining pressure. For each sample, top picture is the fracture face lit from the side, the middle picture is evenly lit, and the bottom picture is a profile.

b)

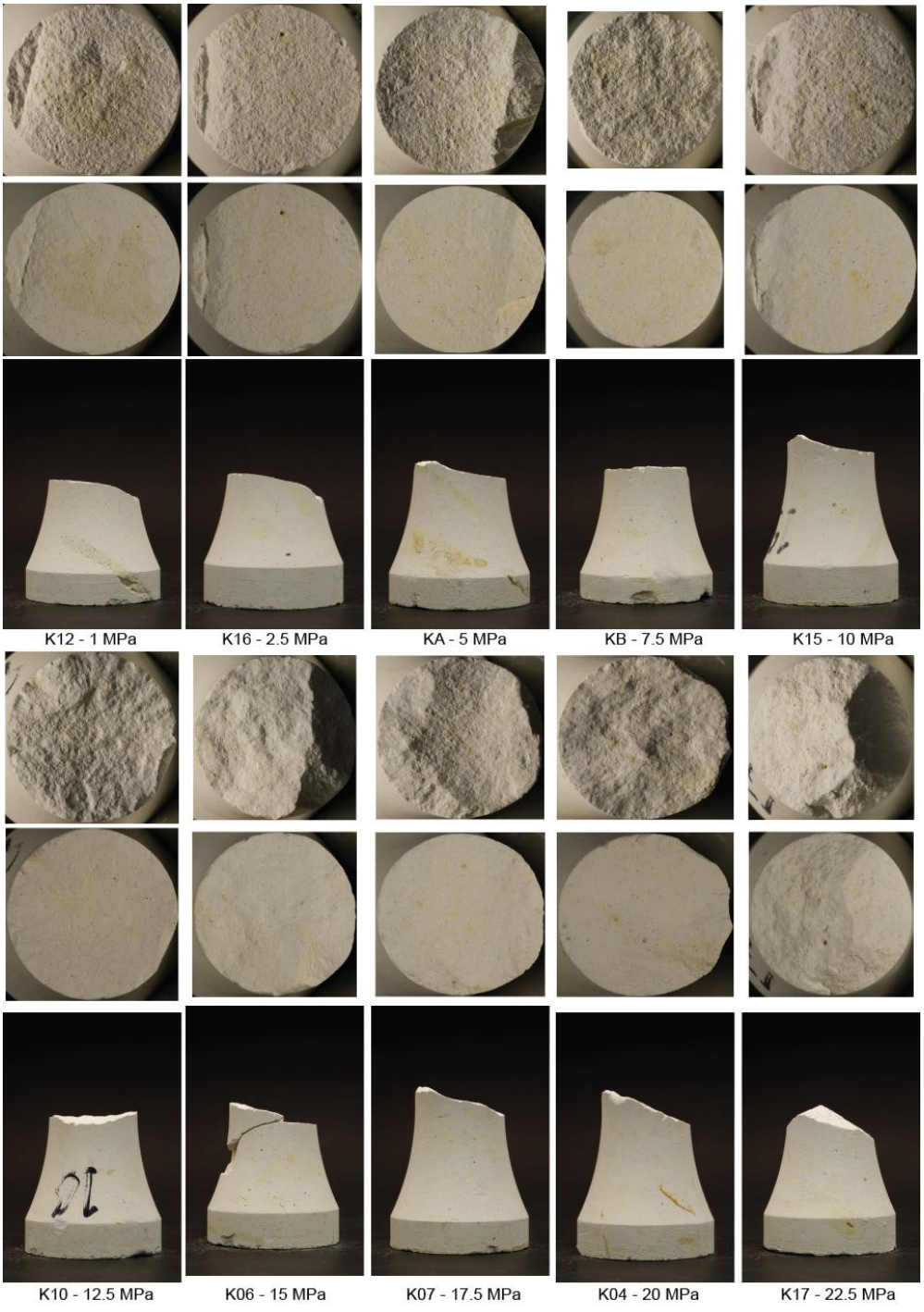

Figure 19. Continued.

overall behavior are similar to the other experiments, suggesting that only the localization point is sensitive to the loading column effects. The faces of the sample show a transition from a rough extension fracture to gouge covered shear fractures. At 5-30 MPa P_c, the surface of the sample shows a very rough fracture, with no gouge patches or other shear indicators. Starting at 40 MPa P_c, shear deformation becomes apparent as there is moderate development of gouge, and the grains of Indiana limestone become less noticeable as they are sheared. All of the samples failed by a single fracture, except for the experiment at 50 MPa P_c, which failed by conjugate fracture.

3.3.2.2. Kansas Chalk

Kansas chalk has a UCS that is a tenth of the UCS of Berea sandstone, so the chalk represents an extremely weak rock in the context of this work. Kansas chalk demonstrates similar relationships between mechanical behavior and confining pressure as the other rock types, but at even lower stress levels. For Kansas chalk, differential stress and axial strain increase with increasing P_C (Figure 18). At 1 MPa P_C, the sample is very weak, the apparent stiffness is very low, and there is negligible strain prior to fracture. (Table 6). With increasing P_C there is an increase in failure strength, apparent stiffness, and inelastic strain prior to fracture. Starting at 5 MPa P_C, samples noticeably yield prior to failure, and there is also a small stress drop post failure. At 22.5 MPa P_c, the sample decreases in strength and apparent stiffness from 20 MPa P_c. The response of the sample is mechanically ductile.

Figure 16 shows the axial stress versus confining pressure at failure for Kansas chalk; the relationship is similar to the other rock types from this study. At the lowest confining pressure, the sample fails in tension with a negative axial stress. Similar to the other rock types, the tensile stress of the material increases with increasing confining pressure, and the sample at 7.5 MPa P_C has the largest negative axial stress at failure. At P_C greater than 7.5 MPa, there is a linear increase in axial stress with P_C. The behavior can be described by two linear relationships, as is the case for the other rock types.

All of the samples fail by the development of a through going fracture. The relationship between fracture angle and P_C is similar to that of the other rock types. At 12.5 MPa P_C and lower, samples display fracture angle of roughly 5-7° (Figure 17). Only the experiment at 7.5 MPa P_c is different with a smaller fracture angle of 2°. At 12.5 MPa P_C and higher, there is a linear increase in fracture angle with increasing P_C. Similar to the other rock types, the behavior can be described by two linear relationships.

Figure 19 shows the deformed samples of Kansas chalk. All of the samples fractured in the middle of the neck except for the two at the lowest P_C tested, 1 MPa and 2.5 MPa. These samples fracture at roughly one third of the neck, the same location as the other rock types. For experiments up to 10 MPa P_C, one side of the fracture curves toward the end of the sample, intersecting the side at a location at one third of the length of the neck. At 1 MPa P_C, the fracture is rough with no shear indicators. At 10 MPa P_C, the fracture face does not have any gouge development, but is slightly smoother than the lower pressure experiments. With increasing confining pressure, shear indicators become apparent as does smoothing of the fracture faces. At 15 MPa P_c, the profile

view of the sample shows that the sample is cut by conjugate fractures. On the straight fracture segment, there are smooth raised patches interspersed on the rough fracture face. At 22.5 MPa P_c, the sample failed by the formation of at least four conjugate fractures. The top half of the sample remained intact, while the lower half of the sample broke into several chips in the vicinity of the fracture. The face of the intact end shows the fracture surface is smooth.

3.4. Discussion

3.4.1. Material Comparison

The experiments on Berea sandstone and Carrara marble performed in this study agree quite well with the previous work on the same materials [*Bobich*, 2005; *Ramsey and Chester*, 2004]. The observed trends in inelastic strain and fracture morphology match the previous microstructural observations and agree well with previous classification of failure mode [*Bobich*, 2005; *Ramsey and Chester*, 2004; *Rodriguez*, 2005]. The experimental results from Indiana limestone and Kansas chalk are consistent overall with the results from Berea sandstone and Carrara marble. Taken together, all four rock types display two distinct fracture regimes: an extension fracture regime, and a hybrid-shear fracture regime. For each rock type, the two fracture regimes are defined on the basis of a bilinear failure criteria in stress space (σ_1 - σ_3) and on the basis of a bilinear relationship of fracture orientation as a function of stress (P_C). Notably, the transition point from extension fracture to hybrid-shear fracture in the bilinear failure

criteria, and in the bilinear fracture orientation relationship, approximately coincide in stress space for each rock type.

Figure 20a depicts the failure strengths for the four rock types in Q-P space. The strength data from all the four rock types fall along the same trend, with the exception of four specific tests at the highest P_C for the two weakest rocks. The three highest P_C experiments for Indiana limestone and the highest P_C experiment for Kansas chalk display a ductile mechanical response (Figure 18). Additionally, the P_C conditions for these experiments exceeds published values of the grain crushing pressure, P^*, for Indiana limestone and Kansas chalk (Table 5). Thus, the experimental data represent a high-pressure deformation regime characteristic of porous rocks, that of shear enhanced compaction, which is not failure by a macroscopic fracture but by a distributed cataclastic flow process. Accordingly these four experiments are not included in subsequent analyses.

The general similarity in the fracture behavior of the different rocks is consistent with the hypothesis that fracture at low mean stress states, including those of mixed compressive and tensile stress, scales with rock strength and is largely independent of rock characteristics such as composition, grain size and porosity. Accordingly, we consider scaling the strength and fracture-orientation criteria by some basic measure of rock strength. This is somewhat analogous to scaling the elliptical cap model for high mean-stress, shear-enhanced compaction of sandstones by the crushing pressure, P^*. Although T_O is a logical scaling parameter, in practice this is deemed a poor choice due to the difficulty in measuring this value accurately, accordingly, we propose scaling by

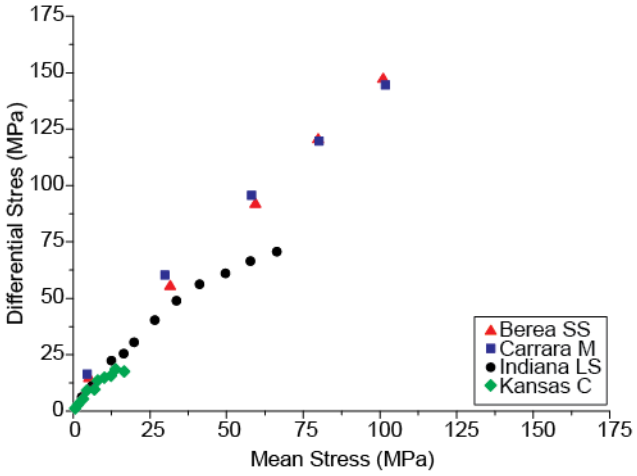

Figure 20. Q-P plot. Failure strengths for Berea sandstone, red triangles, Carrara marble, blue squares, Indiana limestone, black circles, and Kansas chalk, green diamonds, plotted as differential stress versus mean stress.

the unconfined extensional strength, UES. The UES is given by the magnitude of σ_1 at failure in triaxial extension for the specific condition of $\sigma_3 = 0$. Here, the UES is determined for each rock type from the intercept of the σ_1 axis with a best-fit line to the fracture-stress data in the hybrid-shear fracture regime. Note that the UES lies at about the midpoint of the failure envelope for this regime, close to the hybrid-shear transition (*Ramsey & Chester, Rodriguez*), and is thus well defined by the experimental data. Except for Indiana limestone, the UES is higher than the UCS for the rock types (Table 7).

The T_O for the four rock types is determined as the intercept of the σ_3 axis with a best-fit line to the fracture strength data in the extension fracture regime. In general, T_O is small in an absolute sense, as well as relative to typical sample-to-sample strength variations. Accordingly T_O is not a very accurate measurement, particularly for the weaker rocks. As such, the ratio of UES and T_O is expected to display variability and large uncertainty. For the four rock types herein, the ratio ranges from approximately 18 to 60, but the two stronger rocks with much better data would suggest a ratio of approximately 20 is most representative.

Figure 21a shows the failure strengths for the four rocks in normalized σ_1 versus σ_3 space, where both stress components are normalized by the UES for each rock. The normalized values are consistent with a universal, bi-linear failure envelope, in which the tensile stress at failure increases with σ_1 (or P_C) up to σ_1 = UES/2, followed by a change to linearly increasing σ_3 (increasingly compressive) with increasing σ_1. Similarly, Figure 21b shows that the fracture angles as a function of σ_1 normalized by UES also are

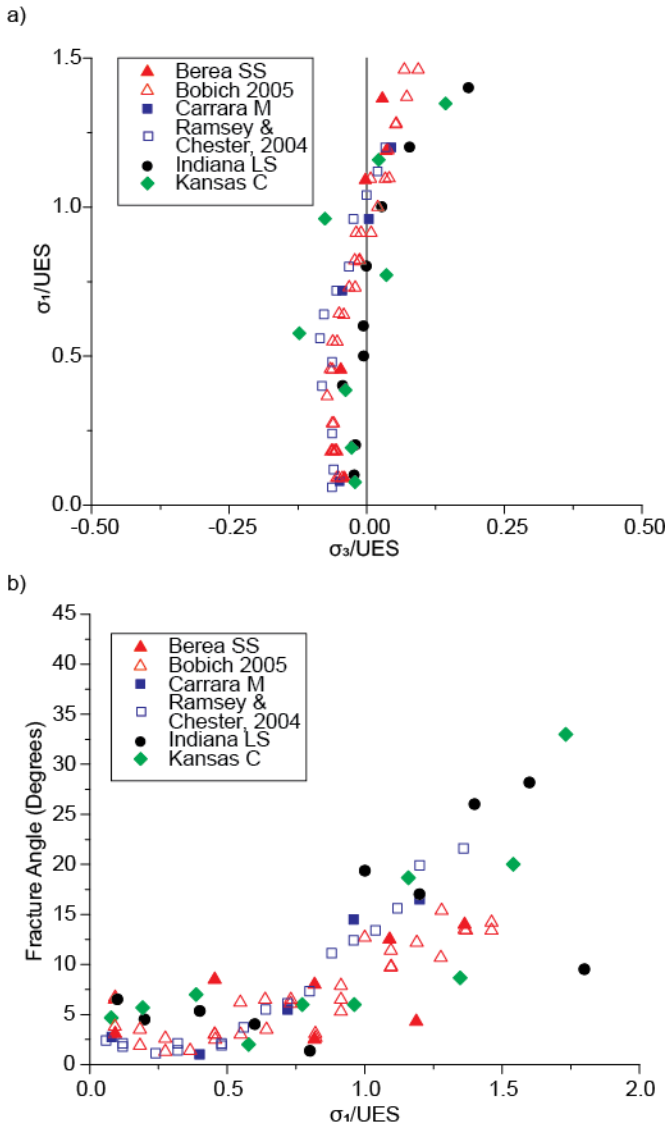

Figure 21. Normalized comparisons. a) Failure strengths plotted in σ_1 - σ_3 space, normalized by UES of the material, for Berea sandstone (red triangles), Carrara marble (blue squares), Indiana limestone (black circles), and Kansas chalk (green diamonds). Previous work as open symbols. b) Measured fracture angles in degrees plotted against normalized σ_1.

consistent with a universal bi-linear relationship. In this case the transition in the fracture angle relationship also occurs at approximately σ_1 = UES/2, from a relatively constant low-angle fracture orientation at low stress to a linearly increasing fracture angle at higher stress.

Fracture orientations for the porous materials have significant scatter as illustrated best by the numerous and the repeat experiments on Berea sandstone. In contrast, Carrara marble shows very well defined and consistent fracture angles, likely due to its nearly isotropic, monomineralic, and uniform structure. Accordingly, the behavior of Carrara marble is used as a guide in characterizing the fracture angle results. As such, the transition between the two different behaviors occurs at σ_1 = UES/2, and the correlation with the changes in failure strength behavior and the fracture angle relationship is quite good.

On the basis of the detailed analysis of failure regimes of Carrara and Berea in previous work (Ramsey & Chester, Bobich, Rodriguez), it is clear that failure at σ_1 < UES/2 is by extension fracture, failure at σ_1 > UES/2 is by hybrid fracture, and failure at σ_1 > 1.25*UES is by shear fracture. If these relationships are indeed universal, then the fracture modes for Indiana limestone and Kansas chalk can be predicted. Failure by extension fracture should be observed in Indiana limestone at P_C values of 5 - 25 MPa, and in Kansas chalk at P_C values of 1 - 7.5 MPa. This is in agreement with the low fracture angles observed, little to no inelastic strain prior to failure, and rough fracture faces (Figure 17, Figure 18, Figure 19). Failure by hybrid fractures should be observed for Indiana limestone at P_C values of 30 - 50 MPa, and for Kansas chalk at P_C values of

10 - 15 MPa. This is in agreement with the increasing amounts of inelastic strain before failure, the emergence of shear indicators on fracture faces, and the increase in fracture angle at the higher confining pressures (Figure 17, Figure 18, Figure 19). For Indiana limestone and Kansas chalk, the highest confining pressure in the hybrid regime both failed by the development of a conjugate fracture. The only other conjugate fracture observed in this study is the highest confining pressure experiment of Kansas chalk (Figure 19). Failure by shear fracture should be observed for Indiana limestone at P_C values of 60 - 90 MPa, and for Kansas chalk at P_C values of 17.5 - 22.5 MPa. These samples have significantly higher inelastic strain prior to failure, have angled fractures, and have shear indicators on the fracture faces (Figure 17, Figure 18, Figure 19). The highest confining pressure for Kansas chalk, 22.5 MPa, and the three highest confining pressure values for Indiana, 70, - 90 MPa, probably represent a transition to a higher pressure deformation mechanism beyond shear failure. These samples were mechanically ductile, deviate from the linear trend observed in Q-P space, and exceed the grain crushing pressure observed in literature (Table 5, Figure 20).

3.4.2. Comparisons against Failure Criterions

Previous work on Berea sandstone and Carrara marble has demonstrated that the conventional approaches to defining the extension to shear transition, the Griffith and modified Griffith criterions, are inadequate at predicting the fracture orientations and failure strengths [*Bobich*, 2005; *Ramsey and Chester*, 2004; *Rodriguez*, 2005]. Neither criterion is able to predict the behavior of the new material either, as Indiana limestone

and Kansas chalk show the same relationship with confining pressure for failure strength and fracture orientation as Berea sandstone and Carrara marble. The conventional criteria do not account for the intermediate principal stress, and are unable to differentiate between triaxial extension and triaxial compression stress states. Figure 22a shows the predictions for the modified Griffith criterion for fracture orientation and the measured values for the four rock types plotted against confining pressure normalized by UES. This demonstrates that the conventional criterion is not capable of predicting the universal trend observed in experiments. The conventional criterion predicts a jump in fracture angles from 0° to 22.5° as the sample transitions from extension fracture to hybrid fracture. Observations demonstrate that the transition is a linear increase from 0°, and low angle fractures are not only possible but also expected. Figure 22c shows the failure strength predictions for the Griffith and modified Griffith criterions against normalized experimental observations in normalized σ_1 - σ_3 space. The Griffith criterion assumes a set UCS to T_0 ratio, so the criterion can be based on either value. Based off of T_0, the criterion under predicts the failure strengths. Based off of the UCS, the criterion under predicts the failure strengths in compression, but over predicts the values in tension. The modified Griffith is more accurate where it is a best fit failure envelope in compression, but still over predicts the values in tension. Figure 22b also demonstrates that the UCS to T_0 ratios for the conventional criterions are inaccurate. The ratios are 8:1 and 10:1 for UCS:T_0 for the Griffith and modified Griffith, respectively, which are too small for the observations. The experiments also demonstrate that the ratio varies

depends on rock strength, which neither conventional criterion is capable of recreating (Table 7).

The Griffith criterion is a theoretical criterion derived on the basis of the propagation of a flaw in an otherwise homogeneous material. An alternative approach would be to use an experimentally derived failure criterion. Menetrey and Willam, 1995, extended the Hoek Brown criterion for rock masses to include effects of the intermediate principal stress to predict the behavior seen biaxial concrete testing. The formula is based on ξ, the hydrostatic stress invariant, ρ, the deviatoric stress invariant, and θ, the deviatoric polar angle.

$$F(\xi,\rho,\theta) = [A_f\rho]^2 + m\left[B_f\rho r(\theta,e) + C_f\xi\right] - c = 0,$$

where

$$A_f = \frac{\sqrt{1.5}}{UCS},\ B_f = \frac{1}{\sqrt{6}UCS},\ C_f = \frac{1}{\sqrt{3}UCS},\ m = \sqrt{3}\frac{UCS^2 - {T_0}^2}{UCS * T_0}\frac{e}{e+1},\ \xi = \frac{1}{\sqrt{3}}P,\ \rho = \sqrt{2J_2},$$

$r(\theta = 0, e) = \frac{1}{e}$ for the extensional meridian, $r\left(\theta = \frac{\pi}{3}, e\right) = 1$ for the compression meridian, and e, the eccentricity of the deviatoric space in the Haigh-Westergaard coordinate space, is $0.5 \leq e \leq 1$. For concrete, e values fall between 0.5 and 0.6 [*Menetrey and Willam*, 1995]. The input parameters for the failure criterion is material's UCS, T_0, and e. Figure 23 compares the three variable concrete model against failure strengths from the triaxial extension experiments presented in this study as well as triaxial compression experiments on the same rock types from previous work. The curves are based on experimental values of UCS and T_0. There is no assumed relationship between UCS, T_0 and *e*, so the value of *e* is determined by best-fitting the concrete function for

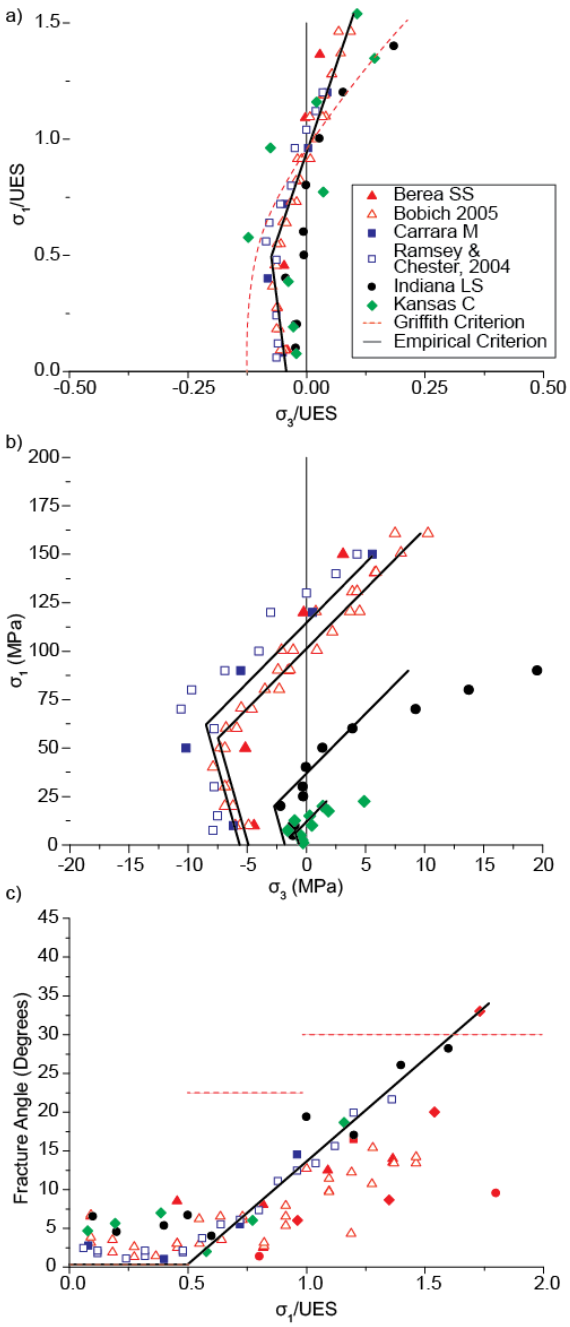

Figure 22. Comparisons against predictions for Griffith criterion. Experimental resulsts normalized by unconfined extensional strength for Berea sandstone, red triangles, Carrara marble, blue squares, Indiana limestone, black circles, and Kansas chalk, green diamonds. Previous work represented by open symboles, predictions for Griffith with dashed red curves. Solid black curves are an empirically fit failure envelope. a) Failure strength in normalized σ_1 - σ_3 space. b) Failure strength in σ_1 - σ_3 space. c) Fracture angles versus normalized σ_1.

Rock Type	UCS (MPa)	UES (MPa)	To (MPa)	UES:To
Berea Sandstone	100	110	4.8	22.9
Carrara Marble	85	125	7	17.9
Indiana Limestone	53	47	0.85	55.3
Kansas Chalk	8.5	13	0.22	59.1

Table 7. Rock properties measured in experiments.

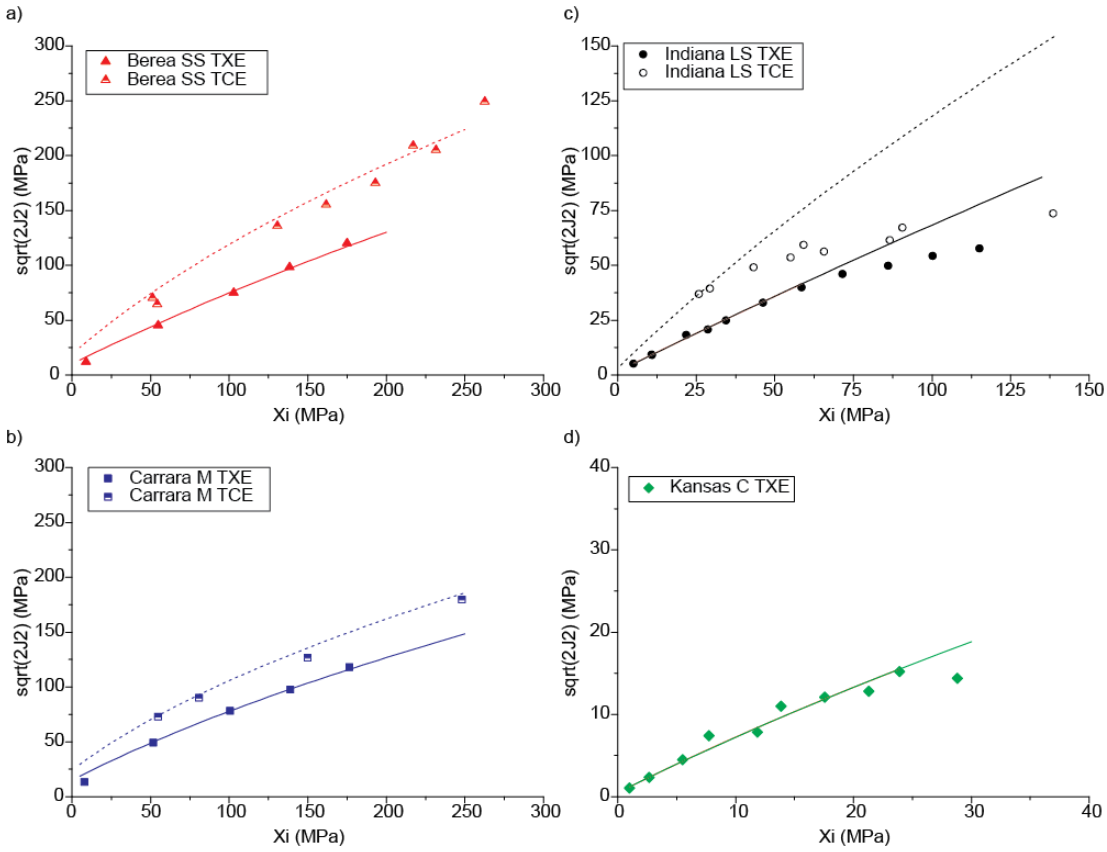

Figure 23. Comparisons of the failure strengths from this study and previous work against predictions from the three variable concrete model. Triaxial extension experiments are closed symbols, triaxial compression experiments are open symbols. The dashed curves are the predictions from the three variable concrete model for a triaxial compression stress state; the solid curves are the predictions for a triaxial extension stress state. (a) Results for Berea sandstone. (b) Results for Carrara marble. (c) Results for Indiana limestone. (d) Results for Kansas chalk.

triaxial compression and triaxial extension data with a Levenberg – Marquardt iteration algorithm. For Indiana limestone and Kansas chalk, the acceptable fits were achieved only when the mechanically ductile samples were ignored. The three variable model accurately predicts the first-order failure strengths for the extension to shear fracture transition in triaxial extension, as well as the shear behavior in triaxial compression from previous work. For Berea sandstone and Carrara marble, the criterion slightly over predicts the lowest mean stress experiment in triaxial extension, but accurately predicts the other experiments in triaxial extension. The failure envelopes are parabolic, which captures the changes in differential stress with increasing mean stress. The three variable concrete model accurately predicts the failure strengths for Indiana limestone. Similarly, the failure envelope over predicts all but the lowest mean stress in triaxial compression. The failure criterion is capable of describing Coulomb like failure in different stress states, but not the elliptical CAP seen in porous materials. Figure 24 compares the failure strengths of the four rock types from this study against predictions from the Menetrey and Willam, 1995, concrete model in σ_1 versus σ_3 space. The model does an adequate job predicting the failure strengths. For Berea sandstone and Carrara marble, the model adequately predicts the hybrid and shear behavior, but, similar to the Griffith and modified Griffith criterions, is not capable of predicting the behavior for tensile stresses. The model has a parabolic shape, and cannot capture the increase in tensile strength with increasing confining pressure.

The three variable concrete model generalizes other failure criterions often included in numerical simulators: Huber-Mises, Drucker-Prager, Rankine, Mohr-

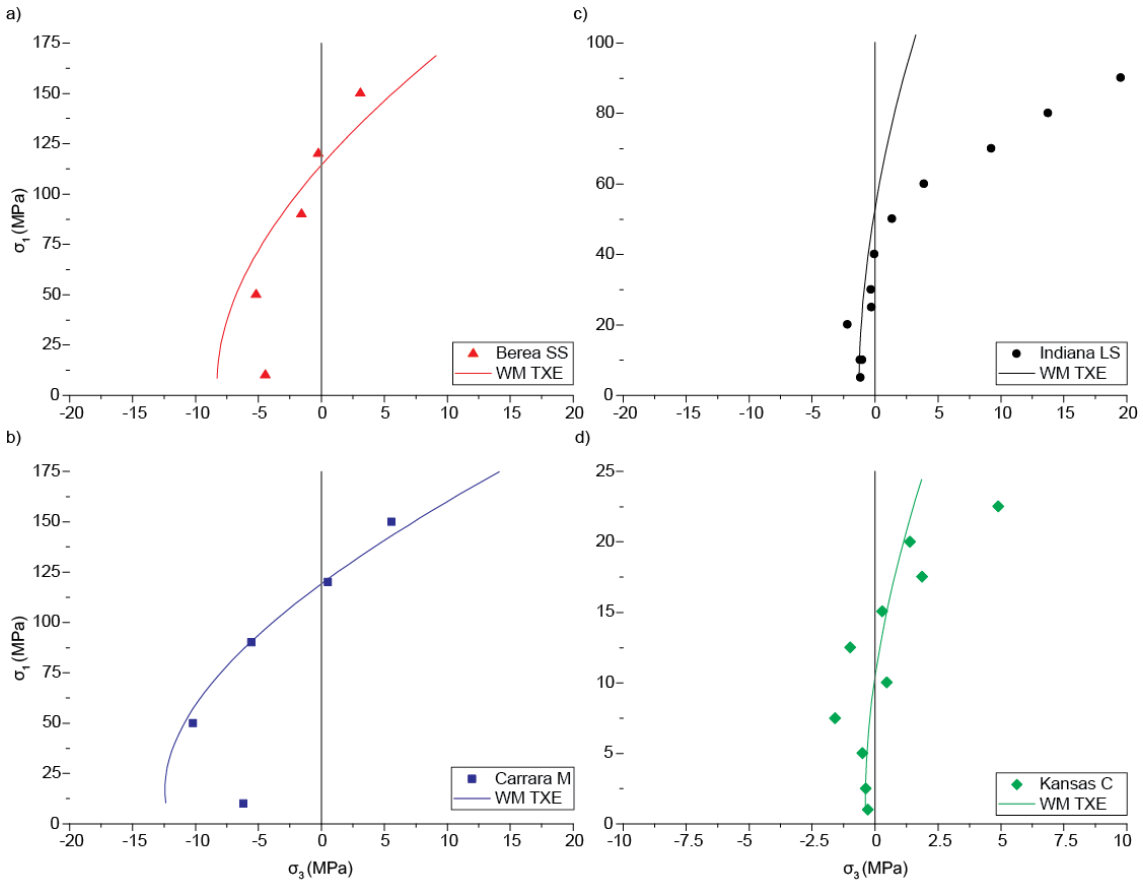

Figure 24. Failure strengths of the four rock types compared to Willam and Menetry, 1995, concrete model in σ_1 - σ_3 space. Experimental results are solid symbols, model predictions for TXE stress states are solid lines. a) Berea sandstone. b) Carrara marble. c) Indiana limestone. d) Kansas chalk.

Coulomb, and Parabolic Leon failure criterions. Figure 25 compares the results for Berea sandstone against predictions from different extensions of the three variable concrete model. The three variable concrete model is the most accurate of the possible criterions. The Mohr-Coulomb extension can predict the tensile stress values, but not the mixed stress cases in triaxial extension. The triaxial compression prediction greatly overestimate the failure strengths. The Rankine model is accurate for predicting the mixed stress cases, but over predicts the failure strengths in triaxial compression. It is more accurate than the Mohr Coulomb criterion. Both the Huber-Mises and Drucker-Prager extensions ignore immediate principal stress effects. The Drucker-Prager over predicts the failure strengths compared to triaxial extension and compression. The Huber-Mises extension predicts a constant value, over predicting tensile stresses and under predicting compressive stresses. Only the three variable model predicts a parabolic shape to the failure envelope, the other derivations predict linear envelopes that do not capture the changes that occur at higher mean stresses. The three variable concrete model was derived for easy incorporation in numerical simulators, and has the basis to be a very powerful tool for geomechanics. The model could be quite useful in simulating a number of industry related geomechanics problems, from the wellbore scale to reservoir scale. The limitations on the model would be the inability to predict fracture angles or compaction seen in porous rocks, as well as the increase in tensile strength with increasing mean stress in the extension to shear fracture transition.

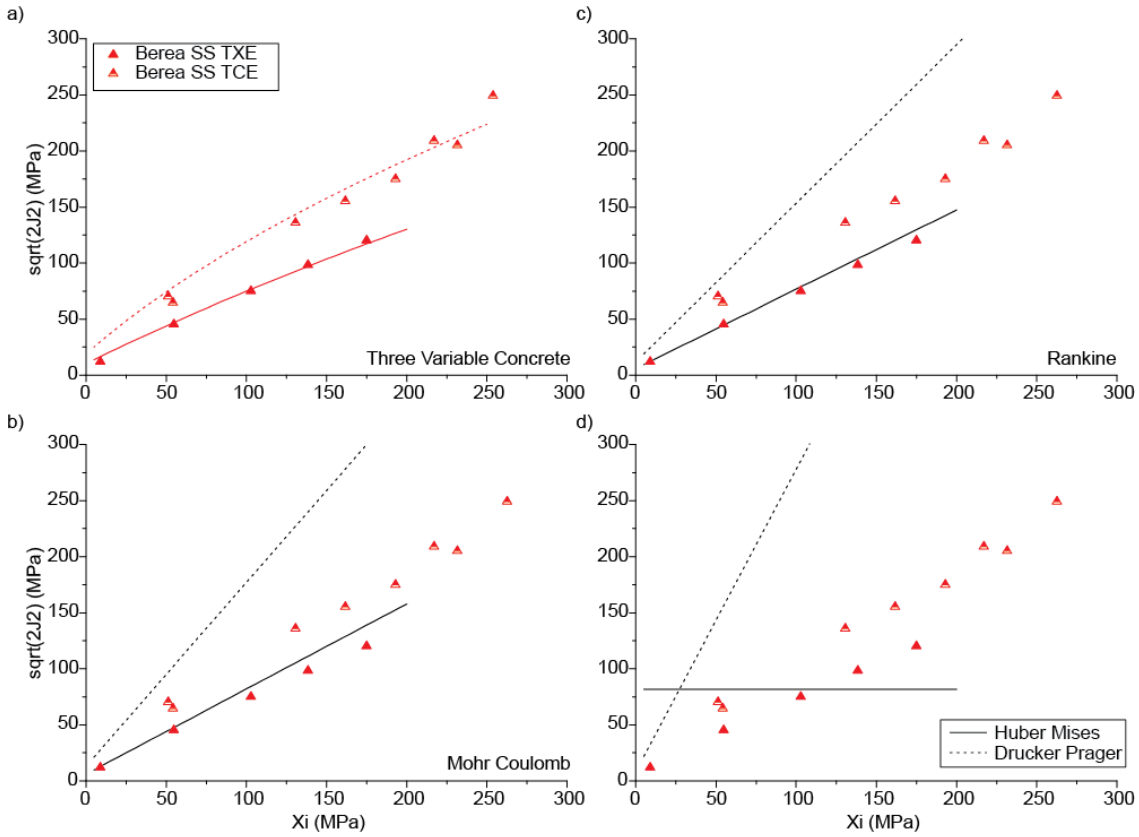

Figure 25. The failure strengths for Berea sandstone compared against different failure criterions. Triaxial extension experiments are closed symbols, triaxial compression experiments are open symbols. Predictions for the failure criterions are dashed curves for triaxial compression experiments, and solid curves are triaxial extension experiments. (a) Predictions for the three variable concrete model. (b) Predictions for the Mohr Coulomb failure criterion. (c) Predictions for the Rankine failure criterion. (d) Predictions for the Huber Mises failure criterion, solid curve, and predictions for the Drucker Prager failure criterion, dashed curve.

3.4.3. New Failure Criterion

As discussed in previous sections, the experimental data presented here can serve as a guide for predicting failure strength and fracture orientation across the extension to shear transition. The normalized comparison shows that the rocks fail by extension fracture at σ_1 values below 0.5UES, and beyond that the rocks fail as hybrid fractures up to 1.25UES, and shear fractures at higher pressures. The comparisons also show that the Carrara marble is the most consistent rock type, and the porous rocks show more scatter in the results, particularly with decreasing rock strength. The empirical envelope should be weighted towards matching the Carrara marble results as they are the best representation of the extension to shear transition, with different segments above and below 0.5UES. Figure 22a shows the empirical failure envelope compared to the normalized results. The failure envelope is given by the following equations:

$$\frac{\sigma_1}{UES} = -20.9 * \frac{\sigma_3}{UES} - .92, 0 \leq \frac{\sigma_1}{UES} \leq 0.5 * UES,$$

$$\frac{\sigma_1}{UES} = 6.17 * \frac{\sigma_3}{UES} + .92, 0.5 * UES < \frac{\sigma_1}{UES}.$$

The fracture orientation can similarly be split into two segments, with an emphasis on matching Carrara marble. For tensile failure, the angles are a constant low value. These can be approximated as 0° in an ideal environment. For the hybrid to shear behavior, the fracture angles form a straight line. The fracture orientations are given by the following equations:

$$\alpha = 0, 0 \leq \frac{\sigma_1}{UES} \leq 0.5 * UES,$$

$$\alpha = 26.5 * \frac{\sigma_1}{UES} - 13.29, 0.5 * UES < \frac{\sigma_1}{UES}.$$

The failure envelope assumes a UES:T_0 ratio of 22.7:1.

3.4.4. Investigation of Local Stress States during Hydraulic Fracturing

The observed fracture and damage behavior seen in hybrid shear fractures could have a pronounced influence on the productivity of induced hydraulic fractures. The development of the riser-tread geometry seen in hybrid fractures with some shear displacement may be a self-propping feature. It would also open a tubular pathway, increasing permeability, much like that described by Ferril & Morris (2003). Increasing amounts of cracking prior to failure would also be beneficial, as it would increase the efficiency of the induced fractures. Greater fragmentation along the main fracture would increase the surface area of the reservoir exposed to the wellbore, and reduce the transport distance of hydrocarbons through the reservoir rock to reach the higher permeability fracture path. Chips and spalls generated by the increased fracturing could also aid in maintaining fracture aperture. The increase in relative angle between the macroscopic fracture and microcracks would further the effect. It is also likely that hybrid fracture would be associated with the reactivation of pre-existing features due to the higher strength and shear displacement. The characteristics associated with hybrid failure could increase the connectivity, extent, and surface area of the induced fracture network, so it is important for field development and planning to be able to predict the behavior a priori.

The complex networks created by mixed mode fracturing should be expected during hydraulic stimulation of reservoirs. Depending on the mechanical properties of the reservoir rock, depth of burial, and tectonic stressing, the induced stress state near the tips of macroscopic hydraulic fractures may consist of mixed tensile and compressive

stress states that tend to favor hybrid fracture meshes and en echelon fracture geometries. If the reservoir contains pre-existing natural fractures or strength heterogeneities that are activated in shear modes, then the heterogeneous stress states within the volume of rock will lead to a range of stress states and mesoscale fracture modes with distributed damage.

Conventionally, the geomechanics prediction of fracture mode is performed in Mohr space using the Griffith or modified Griffith failure envelope [*Zoback*, 2007]. The failure envelope is based on the rock strength, typically UCS. The reservoir stress state is represented by a Mohr circle, and changes pore pressure during injection are represented by shifting the Mohr circle towards negative normal stresses. Failure is predicted to occur when the circle contacts the failure envelope, i.e., when the stress satisfies the failure criterion. This approach predicts the magnitude of pore pressure changed needed to induce fracturing in the reservoir, as well as the expected fracture orientation. If the orientation of preexisting fractures in the reservoir are known, then the normal and shear stresses on the fractures can be calculated using a 3 D Mohr circle and the reservoir stress state.[*Zoback*, 2007]. Combined with the frictional envelope, the pore pressure needed to reactivate these fractures can be calculated. The reactivation pressure can be compared to the fracture initiation pressure to understand the behavior of the hydraulic fracture. However, the experiments in this study have demonstrated that the failure strengths and fracture orientations predicted by the Griffith and modified Griffith criterion are inaccurate. The experimental-based failure criterion derived here cannot be translated to Mohr space easily. The increase in tensile strength with

increasing confining pressure would lead to nested circles when represented in Mohr space, preventing the standard approach to failure envelopes in Mohr space.

Failure envelopes and associated failure-surface orientations based off the experimental results from this study can be combined with local stress states associated with hydraulic fractures to predict the likelihood of mixed mode failure during hydraulic fracturing. Analytical solutions have been formulated for different crack geometries and loading systems; of particular interest to hydraulic fracturing is the stress state around an internally pressurized crack tip [*Rummel,* 1987]. In linear elastic materials, far field stress states and fluid pressure can be calculated individually and summed to find the stress concentrations for the induced fractures and wellbore. Following the analysis of F. Rummel, 1987, it can be show that the stress concentration around an internally pressured induced fracture growing from a wellbore is

$$K_I(S_{HMax}) = 2S_{HMax}\sqrt{R}(\frac{b^2-1}{\pi b^7})^{\frac{1}{2}},$$

$$K_I(S_{hmin}) = -S_{hmin}\sqrt{R}[(\pi b)^{\frac{1}{2}}(1-\frac{2}{\pi}\sin^{-1}\frac{1}{b}) + 2(b^2+1)\left(\frac{b^2-1}{\pi b^7}\right)]^{\frac{1}{2}},$$

$$K_I(p_{wellbore}) = pR^{\frac{1}{2}}[1.3\left(\frac{b-1}{1+b^{\frac{3}{2}}}\right) + 7.8(\frac{\sin\frac{b-1}{2}}{2b^{\frac{3}{2}}-1.7}),$$

$$K_I\left(p_{fracture}\right) = pR^{\frac{1}{2}}[(\pi b)^{\frac{1}{2}}\left(1-\frac{2}{\pi}\sin^{-1}\frac{1}{b}\right)],$$

where

$$b = 1+\frac{a}{R},$$

where K_I is the mode 1 stress intensity factor, R is the radius of the wellbore, a, is the length of the hydraulic fracture, and p is the pressure in the wellbore and the fracture. The combined results for these equations are shown in Figure 26a, which depicts the changes in the maximum and minimum stresses at different radii from the crack tip as a function of angle around the crack, from 0 to 180 degrees, where 0 degrees is directly in front of the crack tip. This figure depicts the change in stress due to internal pressurization alone, far field stresses have been ignored. As the radius decreases, the magnitude of stress change increases. The stresses also depend on the angle. There is no stress change at 180 degrees, and the greatest change in the maximum stress is at 0 degrees. For all radii, the stress states at an angle of 0 degrees can be fit with a linear line with a slope of 1. The greatest tensile stress is actually off the crack tip, at an angle of 60 degrees for all radii. These points also fall on a linear trend with a slope of $^1/_3$. Figure 26b depicts the change of stress around a crack tip when far field stresses of 30 MPa and 10 MPa are included. The shapes of the curves change, but the stresses in front of the crack still fit a linear trend with a slope of 1, and the greatest tensile stresses are still 60 degrees off the crack tip and can be fit with a linear trend with a slope of $^1/_3$. Because the slopes of the trend lines do not change with far field stresses, they can be treated as diagnostic lines.

When combined with knowledge of the reservoir stress state, the failure envelope and the diagnostic slopes from fracture mechanics could be used to predict the expected failure mode in σ_1 versus σ_3 space (Figure 27). The necessary reservoir parameters are simply the rock properties of the target interval, as well as the reservoir stress state and

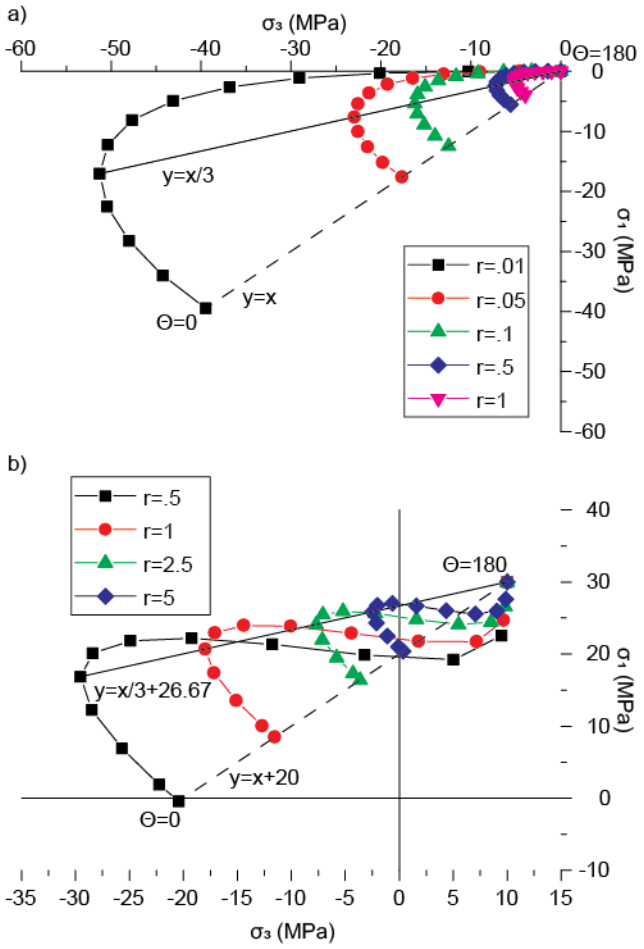

Figure 26. Stress distriburions around a pressurized hydraulic fracture in σ_1 - σ_3 space. Stresses are calculated for different radii around the crack tip, for angles from 0°, directly in front of the crack tip, to 180°. The solid lines represent the greatest stress disturbances, the dashed line represents the stress in front of the crack tip. a) Stress changes from hydraulic fracture alone, no far field stresses. b) Stress changes around a hydraulic fracture tip with far field stresses of 30 MPa and 10 MPa.

fluid pressure. The failure envelope is based off of the UCS/UES and T_0 of the material, but T_0 could also be assumed based on experimental data or relationships. The reservoir stress state would serve as the initial point, the slopes of the diagnostic lines from fracture mechanics would predict the range of the perturbed stresses associated with hydraulic fracturing. Both slopes are included, as the off crack stresses may satisfy failure criteria simultaneous with extension of the master tensile crack tip. We assume that where the diagnostic lines intersect the failure envelope represent the most likely mode of off-crack failure, either tension, shear, or mixed mode.

3.4.5. Cotton Valley Example

The workflow proposed here can be applied to a real world example of hydraulic fracturing to better understand the microseismic source type and distribution. In 1997, a consortium of oil companies and service companies conducted a series of hydraulic fracture experiments with microseismic recording in the Carthage Cotton Valley gas field in east Texas. The experiment was designed to compare conventional gel-proppant treatments with viscous cross-linked gel against the newer treated water and low proppant concentration waterfracs. The stimulation interval was the Upper Cotton Valley formation, a 250 m thick sequence of interbedded sands, siltstone, and shales. The reservoir is in a normal faulting stress state, the maximum horizontal stress is N80°E ± 5° [*Laubach*, 1988]. Two wellbores were stimulated for the experiment. Wellbore 21-10, was stimulated twice, stimulations A and B, at depths 2615-2696m and 2757-2838m.

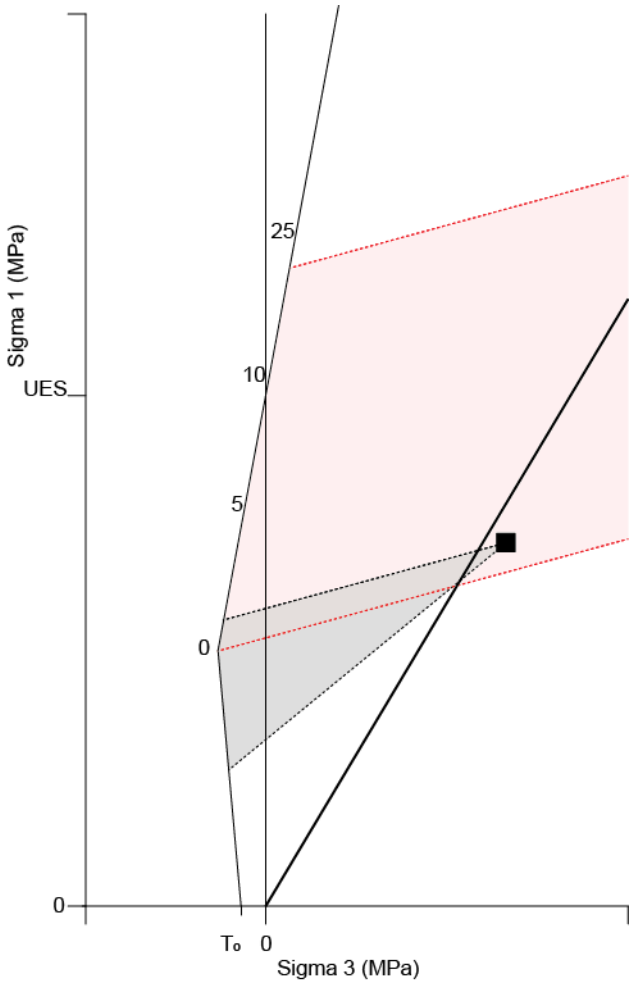

Figure 27. Methodology for predicting hydraulic fracture behavior, in σ_1 - σ_3 space. The thin black line represents the failure envelope scaled for the material's UES. The failure envelope is annotated with the expected fracture angles. The thick black line reprents the fricitional envelope for μ=0.6. The black square represents the reservoir stress state. The dashed black lines and grey polygon represent the stress changes associated with hydraulic fracturing from fracture mechanics. The dashed red lines and polygon represent stress states expected to fail in mixed mode.

The second wellbore, 21-09, was stimulated three times, C, D, and E, at depths of 2607-2643m, 2663-2687m, and 2746-2763m [*Rutledge et al.*, 2004]. At these reservoir intervals, the vertical stress is 63-66 MPa, the minimum horizontal stress is 33-38 MPa, and the reservoir pore pressure is 26.5-32 MPa [*Fischer and Guest*, 2011]. A and B were gel proppant fracs, C, D, and E were waterfracs. Located microseismic events showed a narrow band of vertical seismicity subparallel to the maximum horizontal stress direction (Figure 28a) [*Rutledge et al.*, 2004; *Sileny et al.*, 2009]. In stimulation events B and E, fracture sets, open a distance away from the main fracture in the reservoir trend at a greater angles, between 20-30°. In stimulation B, a separate fracture trend opens off the main fracture at an angle of 10°. In stimulation E, jogs have been identified in the main fracture path. Analysis of microseismic sources show that both double couple, and non-double couple sources are active in the stimulation (Figure 28a) [*Sileny et al.*, 2009]. In stimulation B, workers have identified single couple sources with no double couple components in the isolated fractures that opened up away from the main fracture path, which has been interpreted as the opening of tensile fractures in the reservoir [*Sileny et al.*, 2009]. In the main fracture path, the authors identified large double couple and isotropic explosive components, which they interpreted as typical tensile hydraulic fracture with reactivation of fractures off the main path. In the fracture that grew at an angle to the main fracture trend, the authors identified large isotropic and conjugate double couple components, which they identified as a Hill fracture mesh of interconnected shear fractures and tensile fractures (Figure 28b). In stimulation E,

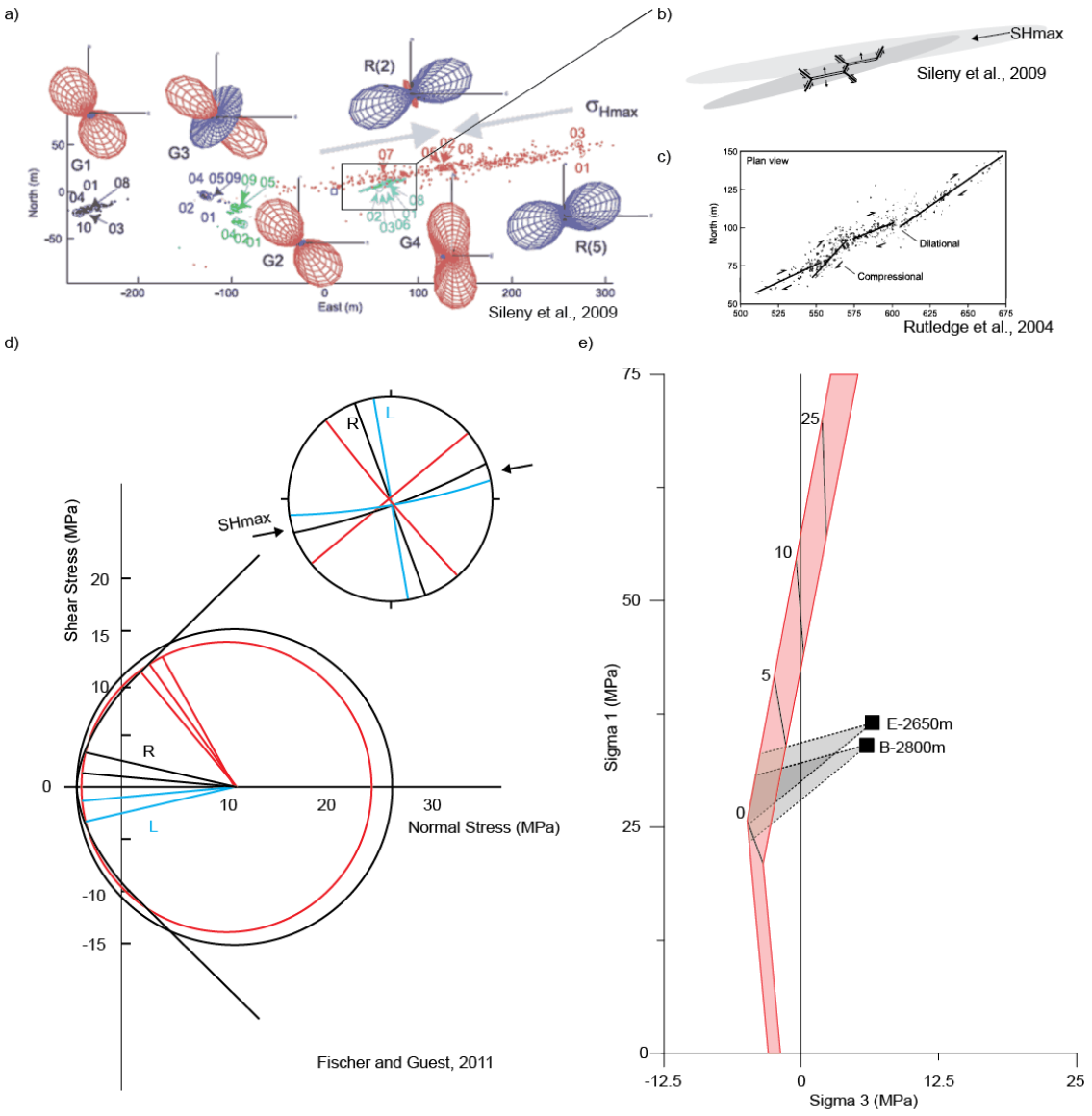

Figure 28. Predictions for the Carthage Cotton Valley hydraulic stimulation. a) Distribution of microseismic events in map view from the stimulation interval B with source types, from Sileny et al., 2009. b) Interpretation of Hill type fracture mesh during stimulation, from Sileny et al., 2009. c) Interpretation of step over in hydraulic fracture path, from Rutledge et al., 2004. d) Geomechanical analysis of Cotton Valley from Fischer and Guest, 2011. e) Geomechanical analysis of Cotton Valley based on experimentally derived failure envelope.

workers have interpreted the opening of an interconnected tensile shear fracture mesh in the jog in the fracture path (Figure 28c) [*Sileny et al.*, 2009].

To understand the occurrence of microseismic sources, Fischer and Guest (2011) used a geomechanics approach based on the Griffith criterion in Mohr space (Figure 28d). Based on well data, the tensile strength of the reservoir is at least 2.3 MPa. The authors chose to base the failure envelope off the assumption that the cohesion of the rock is 9 MPa, which would correspond to a tensile strength of 4.5 MPa and a UCS around 44 MPa. They used the reservoir stress state and the net injection pressure, 37-42 MPa to determine the fracture behavior. They predicted tensile fracture and the reactivation of preexisting fractures in shear. They classified all fractures that opened at angles less than 22.5° as tensile fractures, so the fractures occurring at 10° off the maximum horizontal stress are classified at tensile failures. The fractures that are 30° off the maximum horizontal stress are classified as reactivated shear fractures. While agreeing with general observations, their predictions do not agree with the microseismic source interpretations. The fracture trend 30° off the maximum horizontal trend was interpreted as tensile fractures due to the single couple component, no double couple component was identified, but could also be preexisting fractures extended by the elevated fluid pressure [*Fischer and Guest*, 2011]. The predicted tensile fractures within 10° of the maximum horizontal stress have both double couple and non-double couple components, which has been interpreted as a mixed mode fracture mesh. The limitation in their analysis is the conventional failure envelope. Experiments have demonstrated that fractures oriented at 10° result from failure in the hybrid regime, which would be

consistent with the microseismic observations [*Sileny et al.*, 2009]. The strength of the reservoir might be too low as well. A UCS of 44 MPa is less than Indiana limestone, which seems too low for a tight gas reservoir sandstone.

The failure envelope derived from these experiments can be applied to predict the hydraulic fracture behavior. Figure 28e shows the failure envelope applied to the Cotton Valley example. The failure envelope is based off of the previous UCS, 40 MPa, but includes predictions up to 60 MPa UCS. The failure envelope is contoured with the expected fracture angles based on the experimental observations. The effective reservoir stresses are shown for two of the stimulation intervals, B and E. The polygons to the left of the stress states show the expected perturbations in front of the crack tip based on the analytical fracture mechanics solutions. The stress perturbations intersect the failure envelope in the extension fracture-hybrid fracture portion of the failure envelope. This corresponds to the experiments where the tensile stress is the maximum for failure. The predicted fracture angles at these conditions are between 0° and 5°, close to the in situ observations of the main fracture trend, the offshoot fracture trend, and the jog angle. Experimental analogs for these conditions would be the Berea sandstone and Carrara marble experiments at 50 to 90 MPa P_c. These samples showed a slight indication of inelastic strain prior to failure, and previous microstructural investigation indicates the development of off crack damage prior to failure is characteristic. The fracture faces are composed of segments of extension and shear fracture (Figure 19) [*Bobich*, 2005; *Rodriguez*, 2005]. This tread-riser geometry corresponds well to the microseismic observations in stimulation intervals B and E, where the previous authors interpreted the

development of Hill type fracture meshes [*Sileny et al.*, 2009]. If the orientations of the preexisting fracture are known in the reservoir, the reservoir stress states can be converted into normal and shear stresses on the fractures to calculate the reactivation potential. The experimentally derived failure envelope explains the observations seen in the main fracture path and branches, but not the isolated fracture trends further in the reservoir, which could best be explained by reactivation of preexisting features, whose presence was not known a priori.

3.4.6. Applications to Natural Examples

In induced hydraulic fractures, the contributions of hybrid failure has been overlooked due to inaccuracies in the conventional failure criterion. Similarly, natural examples of hybrid failure have been overlooked for the same reasons. The experiments and analysis presented here show that the transition from extension to shear fracture is continuous. Extension fractures and shear fractures are common, but hybrid fractures are less so and only observed in certain locals. If extension and shear fractures occur regularly, then it should be expected that the conditions for hybrid failure between the two end members should also occur regularly. Transitional stress states are expected to be common occurrences in burial and diagenesis, extensional tectonics, metamorphisms, geothermal, and volcanic provinces.

During basin formation, sediments are deposited and progressively buried as deposition continues. Typically, the sediment types change as water levels fluctuates, usually alternating between sands and mud/shales sequences. As depth increases, the

sediments compact, expelling water. The mud/shale layers compact faster than the sand sequences, increasing pore pressure in the sand layers. As the mud/shale compact, the permeability decreases until the layers are capable of sealing and further increasing pore pressure. In these systems, the pore pressure can reach high enough levels to create hydraulic fractures, especially when combined with an extensional stress state[*Cosgrove*, 2001; *Mourgues et al.*, 2011]. Cosgrove, 2001, mapped sedimentary dikes and sills in the Mercia mudstones of the Bristol Channel basin, England. These dikes represent the transport of sands into bounding mud layers during hydraulic fracturing, allowing the preservation of these features. The authors tied the fractures to extensional pulses during basin formation. What would have started as tensile hydraulic fractures at shallow depths would have transitioned to hybrid fractures as burial depth increases. The authors do not identify any hybrid features, but the example of satin spar veins in Cosgrove, 2001, Fig. 5d, have a similar morphology to mixed mode fracture meshes. With increasing depth, the expected failure mode should transition to shear failure, resulting in conical sand intrusions [*Bureau et al.*, 2013; *Mourgues et al.*, 2012; *Mourgues et al.*, 2011].

Mourges et al., 2011, developed a model to predict the stress states and reservoir properties where hydraulic fractures, extension shear fractures, and compressional shear conical fractures would occur based on the Griffith failure envelope. The experimental envelope presented here would suggest that the extension shear regime would be more common than predicted. Conical sand intrusions are imageable in seismic, but vertical hydraulic fracture with little shear displacement are extremely difficult to image [*Bureau*

et al., 2013]. Hybrid fracture would have a very steep orientation based on the experimental results from this study, and would also be difficult to resolve seismically.

Mixed mode fractures have been identified as arising from alternation weak and strong layers in a sedimentary sequence [*Ferrill et al.*, 2012; *Gross and Engelder*, 1995; *Sibson*, 1996]. In the Monterrey formation, California, authors have identified an interconnected extension and shear fracture mesh, where extension fractures are limited to the stronger dolostone unites, and shear fractures are limited to the weaker mudstone units [*Gross and Engelder*, 1995; *Sibson*, 1996]. Similarly, Ferrill et al., 2012, have identified changes in fracture type due to mechanical differenced in layered stratigraphy in the Hidden Valley fault zone at the Canyon Lake Gorge, Texas. The weaker layers failed in shear, and the stronger layers failed in hybrid-shear fractures. For the intervals that failed in mixed mode, the fault surface is covered with slickensides and interspersed with patches of euhedral crystal faces, very similar in morphology to the fracture faces from the experiments presented here, see Ferrill et al., 2012, (Figure 19). The authors postulate that the limited slip on the fault preserved these features, whereas further shear displacement would have overprinted them, a possible reason hybrid examples are limited. In addition to stress contrasts between neighboring lithologies, changing rock properties could create hybrid fractures [*Davatzes et al.*, 2003; *Petrie et al.*, 2014]. Davatzes et al., 2003, demonstrate how changing rock properties create a mechanisms that could result in hybrid fractures. In the Chimney Rock fault array, Utah, the first generation of ENE striking normal faults formed by the coalescence of deformation bands, indicating weak, porous rocks. The next generation of WNW striking normal

faults formed by splay joint linkage into a through going fault, indicating an increase in rock strength. Microstructural observations show that the sandstone was lithified with quartz cementation post deformation bands and pre jointing, altering the rock properties. While not observing hybrid features, they do demonstrate a mechanisms that could create hybrid features due to diagenesis at comparatively the same stress state. Petrie et al., 2014, linked the variation of extension, extension-shear, and shear fractures in Paleozoic and Mesozoic seal analogs to changes in rock properties and stress states using the Griffith criterion. Strong lithologies failed in tension; weak lithologies failed in shear; and moderate lithologies failed in extension shear. Based on calculations, the failure type changes with depth, depending on rock strength. The moderate lithologies transition from extension to hybrid at 1.5km depth, and the strong lithologies transition at depths greater than 3.5km [*Petrie et al.*, 2014]. With the failure envelope presented here, the depth predictions for the transitions would shift to shallower depths with a greater contribution of hybrid mechanisms. Variations in pore pressure could also create hybrid fracture meshes. Elevated fluid pressures can shift the state of stress from shear to tension, and at depth the transition would be to formation of hybrid fractures. Hill type fracture mesh has been observed in outcrops in gold quartz lodes exposed in large-scale mines in Australia, New Zealand, and Alaska [*L D Miller et al.*, 1992; *L D Miller et al.*, 1994; *Sibson and Scott*, 1998]. These systems are tight rocks, where the preexisting faults have become misoriented to the in situ stress state. During greenschist metamorphisms, fluid was generated in the systems that increase the pore pressure and decrease the effective stress. The size of the gold deposits indicate that large volumes of

fluids circulated through the systems [*Sibson and Scott*, 1998]. Sibson, 1990, termed the behavior fault valve behavior, because the faults are generally locked due to unfavorable stress states for slip without large pore pressures that can create hydraulic fractures and slip along the faults. The interconnected tensile shear fracture meshes represent the key permeability pathways in these otherwise tight systems. The conditions necessary to create fracture meshes could also apply to petroleum expulsion from tight source rocks. Shales are impermeable source rocks; tectonic changes often occur in the history of basins, so misorientation of features is likely; and large volumes of fluids are generated in these systems during hydrocarbon generation. Hybrid structures would be difficult to preserve in outcrop due to the high weathering rates for shales.

Mixed mode failure has been observed with volcanic activity, and the elevated fluid pressures associated with dike emplacement make it likely that hybrid failure should be expected with propagation. Investigation of the process zones around propagating dike tips at Ship Rock Dike, New Mexico, demonstrate that the crack tip induces joints in front of the tip into which the dikes propagate [*Delaney et al.*, 1986]. The dike is surrounded by parallel joints along the length of the dike, similar to the micrographs of hybrid fractures in Carrara marble at low mean stresses [*Rodriguez*, 2005]. The orientation of joints agrees with experimental analogs, suggesting that the deformational mechanisms are similar and hybrid failure should be expected. The detailed investigation of dike damage zones do not indicate mixed mode failure, but some of the step overs in the Ship Rock dike are similar to experiment forming hybrid fractures. Large scale observations of dike geometries at other locations do indicate

hybrid failure [*Angelier et al.*, 1997; *Nairn and Cole*, 1981; *Reches and Fink*, 1988]. Reches and Fink, 1988, determined the mechanisms of emplacement of the Inyo Dike, California, using observations from scientific wellbores and surface outcrops with calculations based on the Griffith criterion. At depth, wellbore observations and Mohr circle analysis indicate a single, large feeder dike emplaced by tensile failure; at the surface the dike breaks into several rotated segments emplaced by shear failure [*Reches and Fink*, 1988]. Hybrid fracture should be expected to occur in between the two stress states, if not at the surface, if one employs a more accurate failure envelope. An investigation of the Inyo Dike at shallow depths should show hybrid features, like a rotation of joints relative to the dike propagation path. Similar transitions in stress states where mapped in the axial rift zone of northeastern Iceland, where tensile failure occurs at the surface and transitions to normal faults at depth [*Angelier et al.*, 1997]. At shallow depths, hybrid failure should be active. In the Faroe Islands, Scotland, workers have mapped three distinct dikes: T-type, N-type, and D-type. T type dikes are single planar fractures; N-type dikes resemble conjugate normal faults with an angle of 40° between them; and D-type dikes resemble conjugate strike slip faults with an angle between them less than 35°. T-type dikes formed in tension, N-type and D-type dikes failed in extension-shear, based on the conjugate angle and predictions from the Griffith criterion [*Angelier et al.*, 1997]. The experiments presented here suggested that the conjugate angles of 40° would be shear failure, and angles between hybrid dikes would be smaller. Difficulty in identifying hybrid dikes could stem from the small conjugate angles that would be difficult to distinguish from natural variability. Basalt dikes in the Tarawera

Rift, New Zealand, also demonstrate hybrid features [*Nairn and Cole*, 1981]. The dikes form a series of left stepping en echelon dikes, where the surface expression forms a riser-tread geometry similar to morphology of hybrid fracture in Carrara marble experiments, Nairn and Cole, 1981, Fig 4, Rodriguez, 2005, Fig 13. The Tarawera dikes show the same damage development expected in hybrid failure. In the extension fracture segments there is a single continuous dike. In the shear linking segments there is a series of short, en echelon dikes that form at an angle to the shear connector orientation, similar to the microcrack development in Carrara marble, Rodriguez 2005, Fig 18.

Field observations confirm that hybrid structures do exist, and investigations of failure processes suggest that they are similar to the processes in the experiments presented here. Fracture orientation, morphology, and damage development all translate to natural examples. The experimental results indicate that the conventional approach for understanding mixed stress states is inadequate, and has led to an underappreciation of the systematics of fracture modes. The stress states that could create hybrid failure are common occurrences in several tectonic settings, and more examples of hybrid failure should be expected. The structures could be difficult to preserve due to healing, overprinting, or outcrop exposure issues, but the relationships presented here could lead to easier identification of these structures, leading to a better understanding of natural stress states and rock properties.

3.5. Conclusions

Experiments were conducted on four different rock types, Berea sandstone, Carrara marble, Indiana limestone, and Kansas chalk, in order to investigate the extension to shear fracture transition. Experiments have demonstrated that there is a characteristic, universal behavior in this transitional stress state. All rock types show the same trends with increasing mean stress. Differential stress at failure, inelastic strain prior to failure, and apparent stiffness all increase with increasing mean stress. The experiments show that the tensile strength of the material increases with increasing mean stress, until the behavior begins to transition to shear behavior. Normalized comparisons show that the transition begins at 0.5UES. There is similar behavior for the fracture orientations as well. Below σ_1 values of 0.5UES, the angles are a constant low value. Above σ_1 values of 0.5UES, there is a linear increase in fracture angle. Below σ_1 values of 0.5UES, the samples are failing in tension. σ_1 values between 0.5UES and 1.25 UES exhibit hybrid failure, and above σ_1 values of 1.25UES the samples fail in shear. The fracture faces reflect this transition as well. Tensile fracture faces are rough, shear fractures are gouge covered, and hybrid failures have rough fracture faces with interspersed patches of gouge.

Comparisons against the Griffith and modified Griffith criterions show that the conventional approaches to defining the extension to shear transition are not capable of matching experimental observations. The Griffith based criterions are not able to predict the observed failure strengths, fracture orientation, or UCS:T_0 ratios. The three variable concrete model is able to predict the failure strength in triaxial compression and

extension stress states, but is not capable of predicting fracture orientations or tensile behavior. Extensions of the criterion to standard criterions are not as accurate as the generalized form.

The experiments presented here can be used as a basis for an empirical failure envelope. The envelope is broken into two segments above and below σ_1 values of 0.5UES to predict the distinctive behavior seen in failure strength and fracture angles. The failure envelope can be combined with fracture mechanics predictions of stress perturbations around an internally pressurized crack tip growing off a wellbore to better understand hydraulic fracture behavior. The approach is better able to predict the microseismic sources and distributions seen in the Carthage Cotton Valley stimulation than the conventional approach based on the Griffith criterion.

The behavior seen in the experiments here suggest that hybrid failure is an underappreciated phenomena due to shortcomings in the conventional Griffith criterion. It is likely that hybrid failure is a common occurrence in burial and diagenesis, volcanisms, and tectonics with large fluid pressures associated with metamorphism or hydrocarbon generation.

4. AN EXPERIMENTAL INVESTIGATION INTO LOCALIZATION PHENOMENA IN THE TENSILE TO SHEAR TRANSITION

4.1. Introduction

Recent advancements and observations in the past few years have highlighted the need for a greater understanding of the behavior of geomaterials at tensile and low mean stresses. The development of induced hydraulic fracturing and long wellbores in previous uneconomic foundations has fundamentally changed the U.S. energy landscape [*Lafollette et al.*, 2012; *U.S.E.I.A.*, 2012]. The common understanding of induced fractures predicts that the resultant geometries should be planar wings [*Fjaer*, 2008]. Physical and seismic observations demonstrate that in many cases, the induced fracture networks form a large, interconnected network [*Cipolla et al.*, 2008; *Rutledge et al.*, 2004; *Sileny et al.*, 2009; *N. R. Warpinski et al.*, 2005; *N. R. Warpinski et al.*, 1993]. Because the success of unconventional reservoirs is entirely dependent on the induced fracture permeability, it is vital to understand the resulting networks of tensile and shear fractures [*Cipolla et al.*, 2008]. Similarly, recent observations of tectonic tremors also highlight the need for a greater understanding of the behavior of rocks at mixed stress states. Typically associated volcanic and geothermal activity [*Hill*, 1977; *A D Miller et al.*, 1998; *Shelly and Hill*, 2011; *Shelly et al.*, 2013a], nonvolcanic tremors and low frequency earthquake events were identified on deep faults in Japan and subsequently in the San Andreas Fault, Cascadia, and the Alpine Fault [*Beeler*, 2012; *Chamberlain et al.*, 2014; *Obara*, 2002]. These tremors are located at deep depths along faults, well below

the seismic-aseismic transition [*Shelly et al.,* 2007; *Sibson,* 1986]. These events have been tied to the presence of fluids, either transient fluid pressure changes or the presence of near supra-lithostatic fluid pressures [*Chamberlain et al.,* 2014; *Ide et al.,* 2007; *Shelly et al.,* 2013a; *Shelly et al.,* 2013b]. It is believed that the elevated fluid pressures decrease the normal stress, allowing brittle failure and slip along faults in an otherwise ductile aseismically slipping zone [*Daub et al.,* 2011]. Tremors do not pose significant seismic hazard, but are of particular interest in understanding the mechanisms and rates of stress transfer from the ductile crustal roots to the seismogenic upper crust. Source analysis from microseismic events from induced hydraulic fractures [*Busetti et al.,* 2014; *Rutledge et al.,* 2004; *Sileny et al.,* 2009], and from events in volcanic and tectonic tremors [*Foulger et al.,* 2004; *Julian et al.,* 1998; *A D Miller et al.,* 1998; *Shelly et al.,* 2013a; *Shelly et al.,* 2013b], identify that both tensile and shear sources are active concurrently. Both examples highlight the importance of the behavior of rocks at low mean stresses. Experiments conducted on different rock types to create a generalized failure envelope are presented in the previous chapter; here we present a subset of the results on Berea sandstone and Carrara marble for a comparison to published plasticity theory in order to test if published theory can be used a predictive and quantitative tool.

Fluid-pressure assisted fracturing can produce mesh and other large, interconnected and complex networks consisting of both extension and shear fractures in various metamorphic, magmatic and tectonic systems [*Hill,* 1977; *Sibson,* 1990; 1996; *Sibson and Scott,* 1998]. Tensile stresses are usually limited to the very shallow crust, where planar joints occur, and deeper in the crust where geothermal, volcanic, and

metamorphic processes create abnormally higher fluid pressures that can exceed the minimum principle stress [*Brace*, 1964; *Sibson*, 1990]. Hill (1977) first proposed a mechanical model to explain the high permeability channels needed to convey large volumes of fluid associated with earthquake swarms arising in geothermal and volcanic provinces, a honeycomb mesh of interlinked shear fractures and extension fractures. Evidence from outrcrops in gold mines and dike damages zones, as well as non-double-couple seismic sources from earthquake swarms in geothermal provinces confirm Hill's model, demonstrating that both tensile and shear fractures are present in a large interconnected fracture mesh [*Foulger et al.*, 2004; *A D Miller et al.*, 1998; *Sibson and Scott*, 1998].

Localization of rock and geomaterials is associated with peak stress, and a number of workers have developed a theoretical framework based on bifurcation analysis [*Haimson and Rudnicki*, 2010; *Issen*, 2002; *Issen and Challa*, 2008; *Issen and Rudnicki*, 2001; *Ottosen and Runesson*, 1991; *Rudnicki and Rice*, 1975]. Originally developed for shear bands, the formula was later extended to predict the occurrence of localized compaction bands in porous sandstones observed in the field and laboratory settings [*Holcomb and Olsson*, 2003; *Olsson and Holcomb*, 2000; *Rudnicki*, 2004; *Wong et al.*, 2001]. The theory predicts that localization can be understood as an instability in the macroscopic constitutive description of inelastic deformation of the material [*Rudnicki and Rice*, 1975]. The theory is based on the first two invariants of the stress tensor, the mean stress and the octahedral shear stress. Localization is predicted to occur when the value of the hardening modulus of the material reaches a critical value. The

theory also predicts the fracture angle based on material properties, stress states, and plastic behavior of the sample. The failure strength predictions did not originally include any way to correct for the intermediate principal stress, and a later formulations accounted for this by incorporating the third invariant of the stress tensor, the Lode angle [*Haimson and Rudnicki*, 2010; *Rudnicki*, 2013]. The theory has be extensively tested for shear and compaction bands in axisymmetric triaxial compression [*Baud et al.*, 2006; *Besuelle et al.*, 2000; *Herrin*, 2008; *Rudnicki*, 2004], but there are limited studies in axisymmetric triaxial extension and polyaxial stress states [*Chemenda et al.*, 2011; *Nguyen et al.*, 2011]. Previous work calculated the dilatancy factor in the tensile to shear transition on a synthetic rock analog material, but did not compare the results against predictions from the localization theory framework of Rudnicki and Rice, 1975, RR. To the authors' knowledge, no studies have attempted to measure and compare the behavior of natural rocks against the predictions of the RR framework for the tensile to shear stress states.

Experimental investigations into the extension to shear fracture transition are limited. There has been recent work on Berea sandstone, Carrara marble, and analog rock material; and earlier work on porous and crystalline rock types such as Westerly granite, greywacke sandstone, quartzite, diabase, and dolomite [*Bobich*, 2005; *Brace*, 1964; *Chemenda et al.*, 2011; *Nguyen et al.*, 2011; *Schock and Louis*, 1982]. The work on Berea sandstone and Carrara marble demonstrated a smooth transition from extension to shear fracture with a gradual change in fracture angle [*Bobich*, 2005; *Ramsey and Chester*, 2004]. The failure envelope demonstrates that as the sample transitions from

pure extensional failure, where the tensile strength of the sample increases with the addition of a compressive load. Sample behavior transitions to a Coulomb regime, with a linear dependence of failure strength on compressive stress. Mesoscopic and microscopic investigations of Carrara marble samples deformed in the transitional regime show that the fracture morphology and damage accumulation vary systematically with mean stress [*Rodriguez*, 2005]. Extension fractures formed in tension display rough faces perpendicular to the tensile axis. In the transitional regime, the fractures form a failure consisting of en echelon opening mode segments connected by shear segments. With increasing mean stress, the surface roughness on the fracture faces decreases in the direction of shear, indication a transition to shear failure. In the transitional regime, there is an increase in off crack damage with increasing mean stress. Tensile fractures have almost no off-crack damage, while shear fractures have extensive off-crack damage [*Rodriguez*, 2005].

In this chapter, we describe two suites of experiments on Berea sandstone and Carrara marble deformed in axisymmetric triaxial extension across the tensile to shear transition. The tests reproduce the failure strength and fracture behavior seen in previous work. The samples are instrumented with strain gages to capture the mechanical behavior at localization. The strain gage data is used to calculate the bifurcation parameters in the RR framework. The deformation band type and fracture angles from the experiments are compared to the predictions localization theory.

4.2. Theoretical Predictions of Localization

Rudnicki and Rice, 1975, and other workers have developed a theoretical framework, bifurcation analysis, to predict strain localization, deformation band orientation, and strain type based on instability analysis in the constitutive description of inelastic behavior [*Ottosen and Runesson*, 1991; *Rudnicki and Rice*, 1975]. This analysis depends on the three stress invariants, τ and σ_{oct}, and the Lode angle, θ_L.

$$\tau = \sqrt{3/2}\,\tau_{oct}$$

$$\tau_{oct} = \left\{[(\sigma_1 - \sigma_2)^2 + (\sigma_2 - \sigma_3)^2 + (\sigma_3 - \sigma_1)^2]^{1/2}\right\}/3$$

$$\sigma_{oct} = (\sigma_1 + \sigma_2 + \sigma_3)/3$$

$$3\theta_L = \arcsin\left(\frac{\sqrt{27}J_3}{2\tau^3}\right) d$$

The Lode angle is a function of the second and third stress invariants, where the third invariant is $J_3=\det(s_{ij})$. The Lode angle is convenient to use for experimental comparisons as the quantity is constant for a given load path. For axisymmetric compression experiments, the Lode angle is 30°; for axisymmetric extension experiments, the Lode angle is -30°; for pure shear experiments the Lode angle is 0° [*Holcomb and Rudnicki*, 2001]. The classic formulation relies on τ and σ_{oct}; the effects of the Lode angle have been neglected in the past due to limitations in experimental geometries, but recent work has shown its importance in the predicting behavior. True triaxial experiments on siltstone show that the fracture angle predictions are improved with the inclusion of the Lode angle into the constitutive model [*Haimson and Rudnicki*,

2010]. Similar experiments on porous sandstone show that effect of the Lode angle decreases with increasing mean stress, suggesting the effect is limited to dilatant processes [*Ingraham et al.*, 2013]. The yield condition and plastic potential are given by the equations:

$$F(\tau, \sigma_{oct}, \theta_L) = 0$$

$$G(\tau, \sigma_{oct}, \theta_L) = 0$$

The formulation is based on non-associated flow, where the normal to the yield surface is not in the same direction as the plastic potential, meaning the dilatancy factor, β, does not equal the slope of the yield surface, μ.

$$-3\beta = \frac{dG/d\sigma_{oct}}{dF/d\tau}$$

$$-3\mu = \frac{dF/d\sigma_{oct}}{dF/d\tau}$$

Subsequently, this means that the ratio of increments of τ and σ_{oct} do not equal the ratio of the increments of the plastic volume strain to the plastic shear strain, $d\gamma^p$. The fracture angle, θ, is given by

$$\theta = (\pi/4) + (1/2)\arcsin(\alpha),$$

where

$$\alpha = \frac{-(1+\upsilon)\cos\varphi\frac{\left(dF/d\sigma_{oct} + dG/d\sigma_{oct}\right)}{dF/d\tau} + (1-2\upsilon)\sin(\varphi+\theta_L)/\sqrt{3}}{\cos(\varphi+\theta_L)},$$

where

$$tan\varphi = \frac{dF/_{\theta_L/\tau}}{dF/_{d\tau}}.$$

Failure is predicted to occur when the plastic hardening modulus, h, reaches the critical value, $h_{cr.}$

$$h = d\tau/_{d\gamma^p},$$

$$\frac{h_{cr}}{G_{shear}} = \frac{(1-\upsilon)}{9(1-\upsilon)}(\beta-\mu)^2 - \frac{1}{2}(1-\upsilon)[N+\frac{1}{3}(\beta+\mu)]^2,$$

where G_{shear} is the shear modulus, υ is the Poisson's ration, and N is the negative of the intermediate principal deviatoric stress divided by τ [*Haimson and Rudnicki*, 2010]. Although this theoretical framework has promise for predicting failure mode under mixed stress states better than the Griffith criteria, there are no published values for any of these parameters for natural rock in the tensile to shear transition. Recent work reported value of β across the tensile to shear transition for an analog rock material, titanium dioxide TiO_2 [*Nguyen et al.*, 2011].

4.3. Methods

4.3.1. Sample Description

Two different rock types used in this study, Berea Sandstone and Carrara marble. Berea sandstone samples were taken from a single block from the Cleveland Rock Quarry in Ohio. Previous studies on samples from this local have shown that the grain size, porosity, and mineralogy are comparable to other published measurements for Berea [*Bobich*, 2005; *Menendez et al.*, 1996; *Zhang et al.*, 1990b]. In general, the samples consist of subangular, well-sorted grains composed of 75-80% quartz, 20-25%

feldspar, and lesser amounts of dolomite, rutile, zircon, kaolinite, and some secondary minerals [*Menendez et al.*, 1996; *Zhang et al.*, 1990b]. Dolomite grains and cement (up to 400μm) are distributed throughout the granular mass. Porosity measurements attained from mass differences between dry samples and samples saturated with alcohol or distilled waters range from 16-19%. The Schwawrtz-Saltykov method was used to determine the grain size distribution from measurements of grain diameter in plane petrographic sections; the mean diameter is 185 μm [*Hillard and Lawson*, 2003; *Zhang et al.*, 1990b]. Bedding laminae, with spacing around 0.5 mm, are defined by concentration of mafic minerals visible on the hand sample scale. Previous studies on Berea have shown that the laminations influence fracture behavior [*Herrin*, 2008]. Samples were cored parallel to the laminations to minimize bedding effects on fracture orientation.

Carrara marble samples were taken from a single block from the Lorano Bianco Carrara marble of Italy. This marble is nearly pure calcite and has less than 1% porosity, with a weak crystallographic preferred orientation. The grain sizes range from 250-355 μm [*Rodriguez*, 2005]. The undeformed marble has occasional thin mechanical twins and sporadic, intragranular, cleavage microfractures that are a few microns in length [*Fredrich et al.*, 1989; *Pieri et al.*, 2001; *Rodriguez*, 2005]

The tests utilized a specialized sample geometry, the notch-cut, or ‘dogbone’ geometry. This particular sample geometry has been used in previous studies across the tensile to shear transition and has shown to produce consistent and reproducible results as compared to other sample geometries in the same stress field. To create the dogbone

geometry, the samples are ground on a microlathe mounted on a stationary surface grinder to create the neck of the sample. Two inch diameter cores are mounted on the microlathe with the cylindrical axis perpendicular to the grinding wheel. The samples are ground down slightly, to a 1.995 inch diameter to ensure that the samples are perfectly round and the axis is true to the microlathe. To cut the neck, the microlathe is turned parallel to the grinding wheel. The diameter of the grinding wheel determines the radius of curvature of the neck, 88 mm. After the neck is finished, the sample is cut to length, and the ends are ground perpendicular to the axis. The final dimensions of the sample are 102 mm in length, 47 mm diameter at the shoulder, and 30 mm diameter at the neck.

The samples are instrumented with strain gages glued in the center of the neck of the samples. The sample geometry creates a stress concentration in the neck of the sample, allowing the strain gages to be placed in the optimal location to capture the mechanical behavior at localization. The strain gages used in the tests were Micro Measurements constantan grids encapsulated in polymide with 350 ohm resistance. The grid pattern was an overlaid and stacked orthogonal rosette measuring 10.7 mm square. The small size of the grid aided in placing the gage in the center of the neck with the opposing curvatures from the cylindrical axis of the sample and the radius of curvature of the dogbone. The gages were aligned with the vertical axis to measure the axial and radial strains. Two gages were used per sample. For Berea sandstone, gages were affixed parallel and perpendicular to bedding laminations. For Carrara marble, gages were affixed parallel and perpendicular to the fast P wave velocity direction. The

different rock types required different surface preparations to affix the gages. To prevent the strain gage from deforming into the pore space of Berea sandstone during hydrostatic loading, the surface was first coated and wiped flush with a layer of Ultra Cal 30, a weak gypsum cement. The surface was cleaned with M Prep Conditioner A, a mild phosphoric acid compound, and shortly thereafter with M Prep Neutralizer 5A, an ammonia based material. The gages were affixed using with M Bond 200, a room temperature, quick cure adhesive requiring thumb pressure to set. A thin layer of M Coat A, an air drying solvent thinned polyurethane, was applied to protect the surface of the gage. For the Carrara marble, the surface was initially abraded with 400 grit silicon carbide paper and M Prep Conditioner A, and wiped clean. The surface was cleaned with M Prep Conditioner A and M Prep Neutralizer 5A, and the gages were affixed as before. The gages were wired with 30 AWG wire wrap wire. Because of the jacketing procedure, the wire had to be routed out underneath the jacketing and out through a pore pressure port in the top piston. To protect the wires during loading, a groove was machined into the shoulder and top of the samples. To prevent confining pressure, P_c, from pinching the jacket on the edges of the groove, the wire were placed in the groove and the groove was filled with a quick cure epoxy.

Maintaining jacket integrity pre and post failure while still transmitting the stresses from the confining medium necessitated a three layer jacketing procedure. The first layer was a 0.2 mm thick latex sheeting wrapped directly onto the sample. Previous studies have shown that the latex jacketing is extremely weak and does not affect the mechanical behavior of the sample while protecting from the next layer, placticene

modeling clay [*Bobich*, 2005; *Ramsey and Chester*, 2004]. The clay was used to fill the void in the sample created by the dogbone; the clay is extremely weak under pressure, transmitting the confining pressure to the neck of the sample while mechanically decoupling the jackets. The clay also prevents the edges from the shoulders from cutting the jackets. The assembly was isolated from the confining fluid by a layer of heat shrink polyolefin tubing sealed at the endcaps with nickel-chrome tie wires. The tie wires were coated with a layer of flexible UV cure epoxy for additional protection.

4.3.2. Experimental Procedure

Experiments were conducted at Sandia National Laboratories at the geomechanics research laboratory using a 1 MN load frame. The machine has independent confining and pore pressure systems, as well as electrical feedthroughs for sample instrumentation. Isopar, an isoparaffinic fluid solvent, was used as the confining medium. Experiments were performed at an axial strain rate of 10^{-5} per second. Axial stress was measured with an external load cell. Because of the arrangement of the sample assembly, the axial stress and confining pressure were independent. The sample was initially loaded with a 1 MPa axial stress before confining pressure was added. The axial stress was increased as the confining pressure was increased to maintain a 1 MPa differential stress on the sample. This small load ensured that the sample assembly remained in contact with the piston during the hydrostatic loading. When the desired confining pressure was reached, the axial stress was decreased and the piston was reversed at a constant rate while the confining pressure was held constant. The

confining pressure was the greatest principal stresses, and the axial stress was the least principal stress. Due to the difference in areas between the shoulders and necks of the samples, a tensile stress can be generated in the neck of the sample. Confining pressure values were chosen to investigate characteristic behavior observed in the previous work of Bobich, 2004, and Ramsey and Chester, 2004. Values of 10 - 150 MPa P_c were used. Samples were deformed dry and vented to the atmosphere.

In this paper we adopt the convention that compressive stress and contractive strains are positive. We will note the maximum and minimum principal stresses by σ_1 and σ_3, respectively. The mean stress, $(\sigma_1 + \sigma_3) / 3$, is denoted by P, and the differential stress, $\sigma_1 - \sigma_3$, by Q. Volume strain, ε_v was calculated from the axial strain, ε_a, and radial strain, ε_r, as $\varepsilon_v = \varepsilon_a + 2\varepsilon_r$.

4.4. Results

4.4.1. Berea Sandstone

For the five experiments on Berea sandstone, all samples fail by the development of a through going fracture. Differential stress and axial strain increase with increasing confining pressure (Figure 29a). At 10 MPa P_c, the sample exhibited negligible plastic strain before failure. At this lowest pressure, the sample is loaded in pure tension, reflected by the soft response of the sample. With increasing effective pressure and larger shear components of loading, the values for Young's Modulus, E, increased, Table 8. At 50 MPa P_c, the sample still displays little to no plastic strain before failure. At 90 MPa P_c, the sampler is stiffer, and begins to accumulate plastic strain before

failure. At 120 and 150 MPa P_c, the samples are stronger and accumulate noticeable plastic strain as the curves plateau before failure. For the samples deformed at effective pressures of 120 and 150 MPa, there is a sharp and well defined stress drop at failure, this behavior is not seen at the lower confining pressures of 10, 50, and 90 MPa. This response is typical of shear failure in the Coulomb regime. The axial stress at failure for the five effective pressures tested is shown in Figure 30; the relationship is not linear or intuitive. At the lowest confining pressure of 10 MPa, the sample fails in tension with a negative axial stress. With increasing P_c at 50 MPa, the tensile strength of the sample actually increases and the sample fails at a larger magnitude negative axial strain. As the samples transition to the shear regime, the axial stress reduces in magnitude. At 90 MPa P_c, the axial stress is at a lower magnitude negative value, and at 120 MPa P_c, the axial stress is 0 MPa. At 150 MPa P_c, the sample fails in shear and the axial stress is positive. From 50 to 150 MPa P_c, there is a linear increase in axial stress. The relationship between differential stress at failure and mean stress is direct. Figure 31 shows that there is a smooth increase in the magnitude of differential stress with increasing mean stress.

All of the samples fail by the development of a through going fracture, but the orientation and morphology vary greatly across the effective pressure range. The relationship between fracture angle and effective pressure is similar to that of the axial stress at failure and effective pressure (Figure 30, Figure 32). At 10 MPa P_c, the sample fail by a single fracture oriented 5° off the horizontal plane. At 50 MPa P_c, the fracture angle decreases. The smallest fracture angle corresponds with the highest tensile

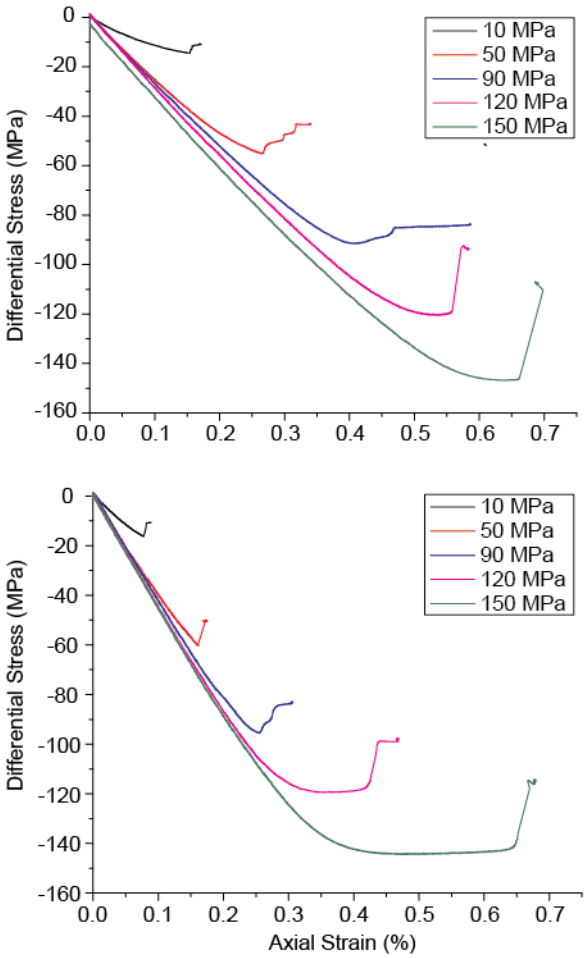

Figure 29. Experimental results. Results from triaxial extension experiments on Berea sanstone and Carrara marble for effective pressures of 10 (black), 50 (red), 90 (blue), 120 (pink), and 150 (green) MPa. Differential stress versus axial strain measured externally. a) Berea sandstone. b) Carrara marble.

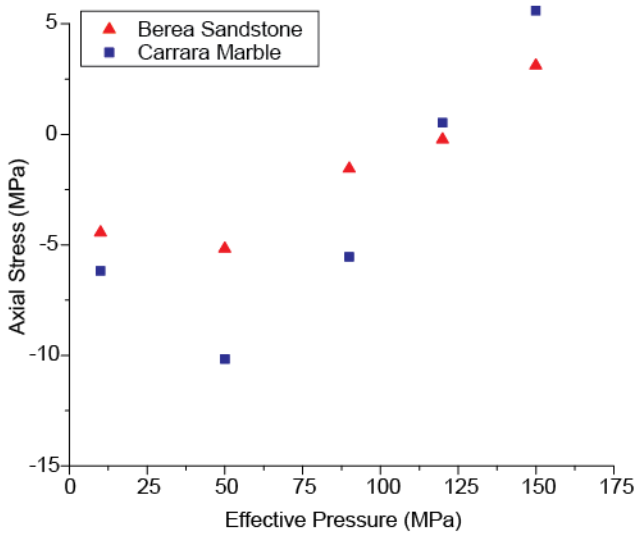

Figure 30. Failure stengths. Failure strengths for Berea sandstone, red triangles, and Carrara marble, blue squares, in axial stress versus confining pressure space.

Berea	Parallel	Perpendicular	Average	Parallel	Perpendicular	Average	Parallel	Perpendicular	Average		
Pc (MPa)	Young's Modulus (Gpa)			Poisson's Ratio			Beta			Mu	Fracture Angle
10	24.72		24.72	0.11		0.11	1.50		1.50	0.89	6.5
50	32.05	29.17	30.61	0.05	0.05	0.05	1.13	1.42	1.28	0.82	8.5
90	30.20	29.56	29.88	0.11	0.05	0.08	0.59	1.37	0.98	0.78	8.0
120	32.61	29.26	30.94	0.12	0.10	0.11	0.78	1.08	0.93	0.77	12.5
150	31.63	31.50	31.57	0.13	0.08	0.10	1.05	0.98	1.01	0.71	14.0

Carrara											
Pc (MPa)	Young's Modulus (Gpa)			Poisson's Ratio			Beta			Mu	Fracture Angle
10	75.91	58.55	67.23	0.21	0.21	0.21	1.22	1.66	1.44	1.00	2.8
50	74.07	73.96	74.01	0.25	0.26	0.25	1.10	1.26	1.18	0.86	1.0
90	73.32	71.24	72.28	0.25	0.24	0.25	0.94	1.07	1.00	0.68	5.5
120	75.40	73.23	74.31	0.26	0.27	0.26	0.84	0.84	0.84	0.65	14.5
150	73.89	75.61	74.75	0.26	0.27	0.26	0.72	0.73	0.73	0.66	16.5

Table 8. Results for Berea sandstone and Carrara marble.

strength. Starting at 90 MPa P_c, there is an increase in fracture angle with increasing effective pressure. From 50 to 150 MPa P_c, there is a linear increase in fracture angle with effective pressure.

The deformed samples of Berea sandstone are shown in Figure 33a. All of the samples fracture in the middle of the sample, through the strain gages, except for the lowest confining pressure tested. In general, the latex jacketing is sufficient to prevent the extrusion of plasticene clay post failure, preserving the morphology of the newly formed fracture face. The faces of the sample show a characteristic distribution of gouge, with a larger proportion of gouge with increasing effective pressure. The profile view of the sample deformed at 10 MPa P_c demonstrates that the sample fractured out of the middle of the sample, at roughly one third of the neck. The surface of the sample shows a very rough fracture, with no gouge patches or shear indicators. At 50 MPa P_c, the profile view of the sample demonstrates that the sample fractures in the middle of the neck, at the expected location. The fracture cuts across on of the strain gages, indicating that the gages are ideally placed to capture localization as it occurs. The face of the fracture displays a rough texture, with only a hint of gouge. The topography of the fracture face suggests the initiation of en echelon fracture geometry. At 90 MPa P_c, the profile of the sample shows the fracture occurred in the center of the neck. There are distinct patches of gouge on the sample face, as well as the development of a ramp flat ramp geometry. At 120 MPa P_c, the profile of the sample displays a sharp fracture though the center of the sample, cutting one of the strain gages. The sample face has a higher proportion of gouge, now distributed across the face of the sample. At 150 MPa

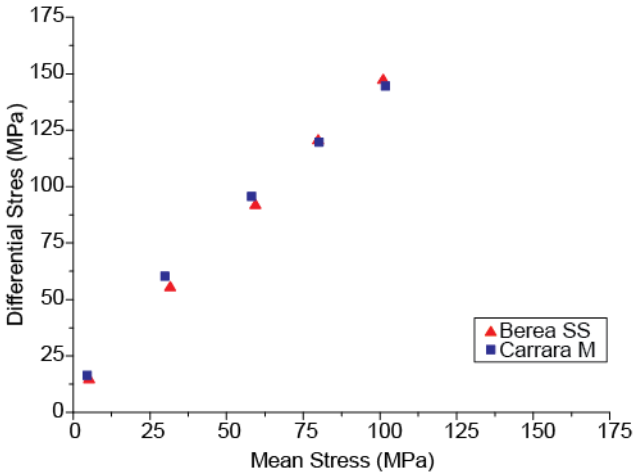

Figure 31. Q-P space. Failure strengths for Berea sandstone, red triangles, and Carrara marble, blue squares, plotted in Q-P space.

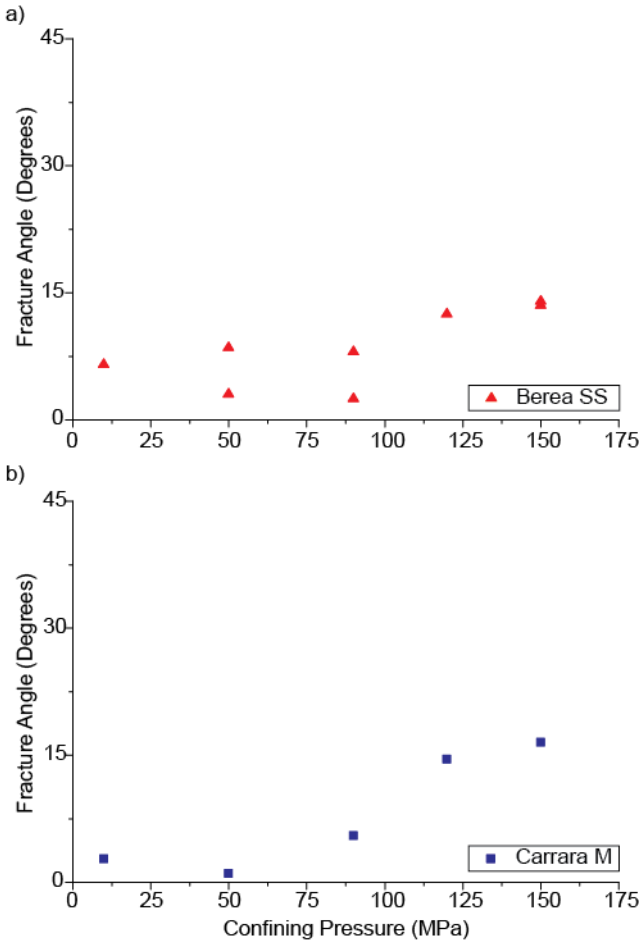

Figure 32. Changes in fracture angle with confining pressure. Results from a) Berea sandstone and b) Carrara marble.

Figure 33. Photographs of the fracture face and profile for a) Berea sandstone, b) Carrara marble. Samples are annotated with confining pressure. For each sample, top picture is the fracture face lit from the side, the middle picture is evenly lit, and the bottom picture is a profile.

a)

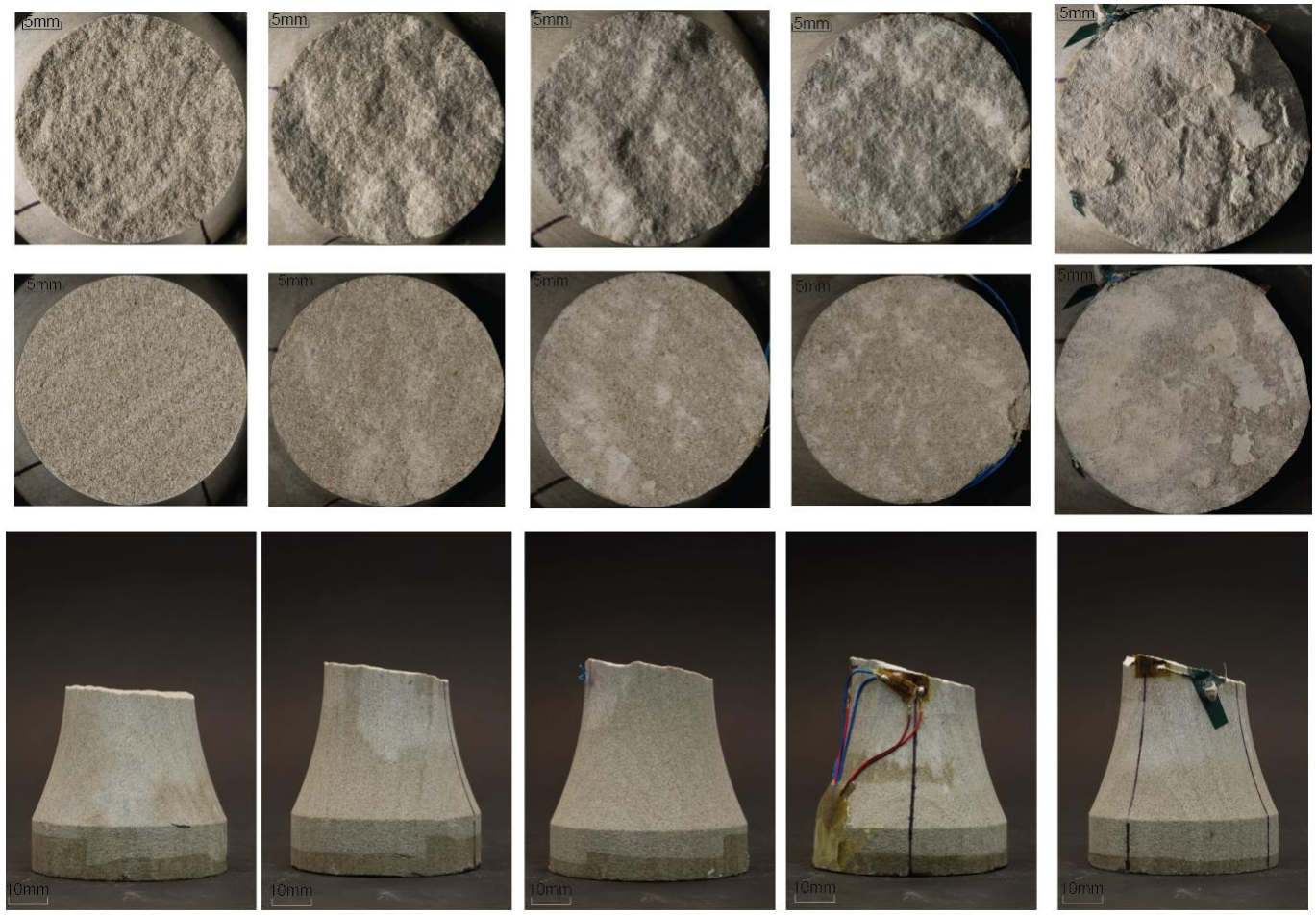

b)

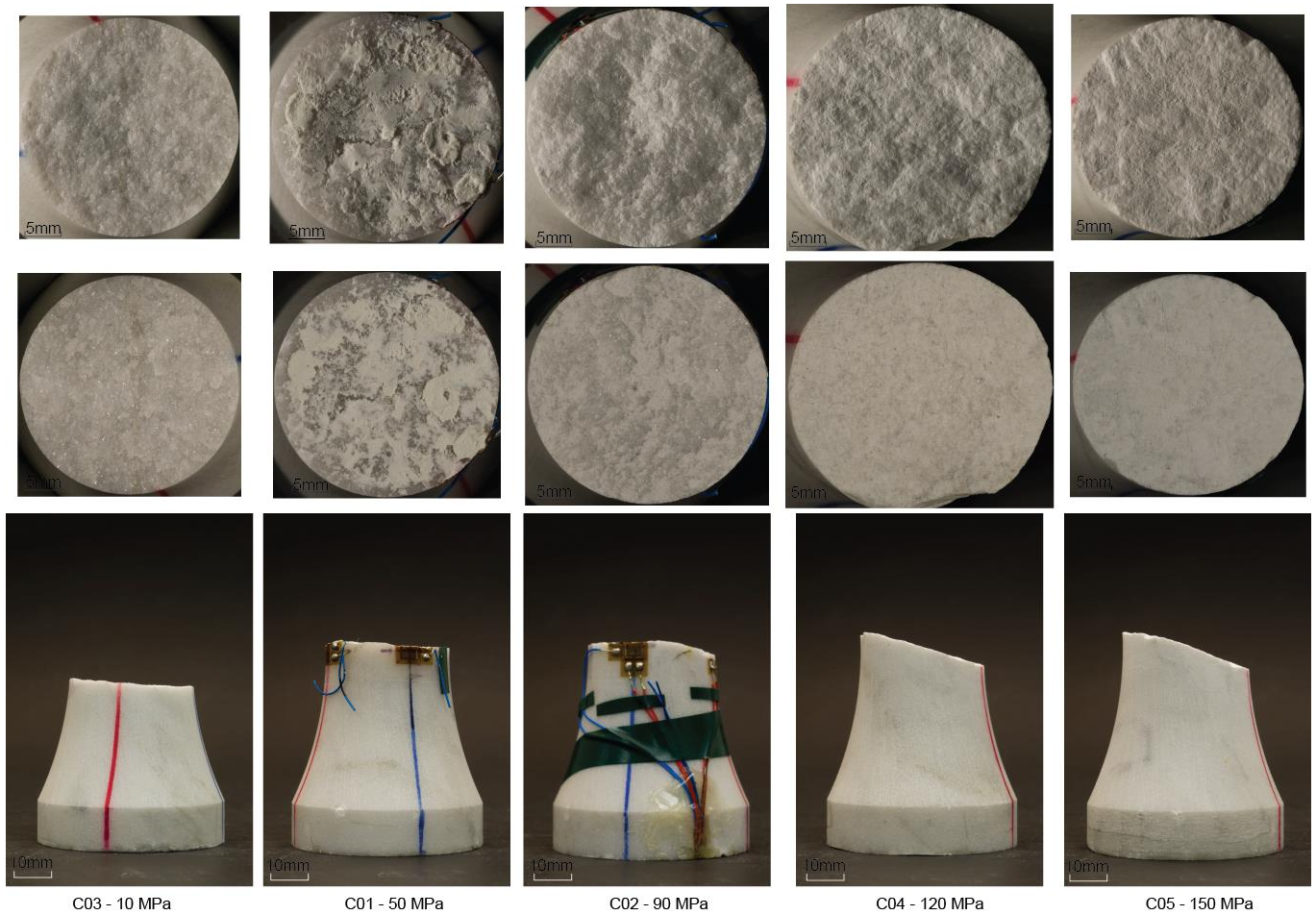

Figure 33. Continued.

P_c, the fracture occurs in the middle of the neck and cut one of the strain gages. Clay intruded into the jacket after failure, so the sample surface is not preserved. The intruded clay is coated with gouge, and removal from the fracture face shows that face is smooth, indicating shear failure.

The mechanical data from the strain gages is shown in Figure 34. Due to the placement of the strain gages on the neck at the minimal sample diameter, the gages measure the localized response of the sample where the stress concentration is the highest. The responses for the strain gages differ from the external measurements as the local responses have slightly higher measured strain, and the onset of inelastic deformation is much clearer in the strain gages. The strain gages placed parallel to bedding had lower Young's modulus and higher strain at failure than the gages placed perpendicular to failure, but this effect is minimized with increasing P_c. The lateral response of the sample is much stiffer than the axial responses, and the lateral strains display less inelastic damage than the axial strains. For the lowest P_c of 10 MPa, the sample was very soft. The strain gage response shows an appreciable development of inelastic axial strain as compared to the externally measured axial strain. The lateral strain is stiffer than the axial strain, but still displays an early yield point at roughly half the failure strength. Unlike the rest of the experiments, at 10 MPa P_c, the strain measured by strain gage is slightly less than the total strain measured by the external displacement. At 50 MPa P_c, the sample is stiffer and stronger. The sample noticeably yields at roughly two thirds of the failure strength, reflected on both the axial and lateral strains. The behavior measured by the strain gage demonstrates the accumulation of

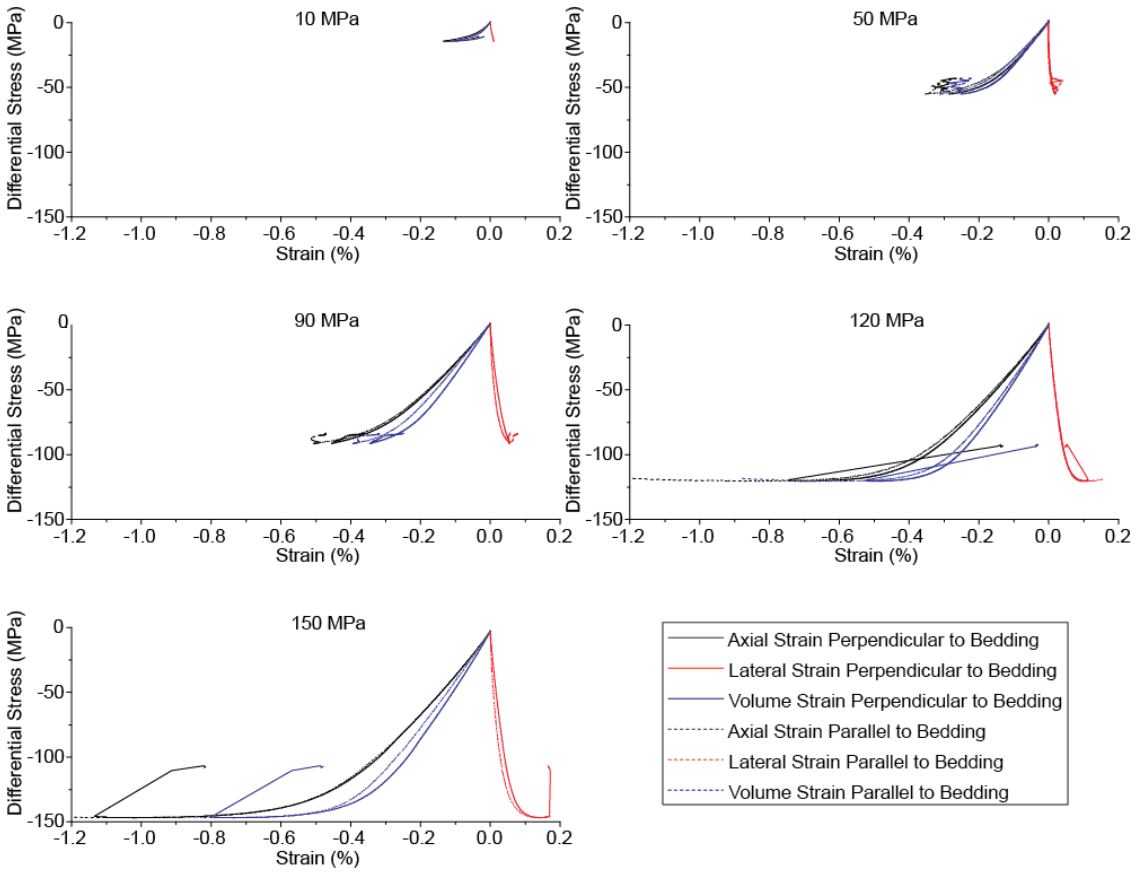

Figure 34. Strain gage results for Berea sandstone. Differential stress versus axial (black), lateral (red), and volume strain (blue) for Berea sandstone. Solid curves represent strain gages perpendicular to bedding, dashed curves represent strain gages parallel to bedding. a) 10 MPa. b) 50 MPa. c) 90 MPa. d) 120 MPa. e.) 150 MPa.

inelastic strain before failure. At 90 MPa P_c, the behavior is similar to the previous experiment. There is strain softening post failure on the lateral strain measured parallel to bedding. At 120 MPa P_c, the sample yields and slightly stain softens before failure, on both the axial and lateral strains. At 150 MPa P_c, the sample yields and behaves plastically, particularly the axial and volume strain. The lateral strain component displays pronounced accumulation of inelastic damage and strain softening post yielding and prior to fracture formation.

The data from the strain gages is used to differentiate the elastic and plastic response of the sample, and this is used to derive the necessary parameter for the bifurcation analysis to predict localization. The slope of the yield surface is determined using the local slope from a best fit linear relationship for the nearest two neighbors for a given failure strength plotted in square root J2 versus mean stress space. Figure 35 displays the derived beta and mu values for Berea sandstone. The points are annotated with the value of the effective pressure for the experiments. For Berea sandstone, the data does not have a clear trend. The points have a positive mu and beta values. Mu decreases with increasing P_c, but there is not a clear relationship for beta. The beta value for the 50 MPa P_c experiment is the lowest magnitude, while the 90 MPa P_c experiment has the highest magnitude. The values for the 10, 120, and 150 MPa P_c experiments are the intermediate values. There is a clear trend when Beta values are plotted against mean stress, Figure 36. While there is scatter to the data, there is a linear relationship of beta values with increasing mean stress.

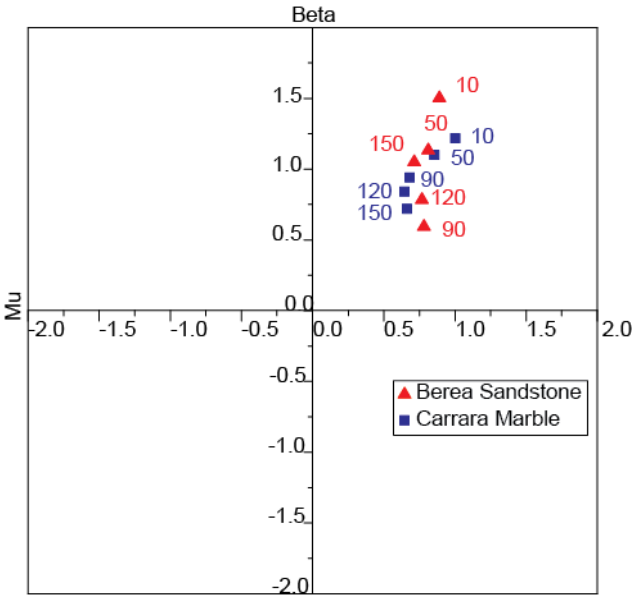

Figure 35. Beta mu diagram. Beta versus mu for Berea sandstone, red triangles, and Carrara marble, blue squares. Results are annotated with experimental confining pressures.

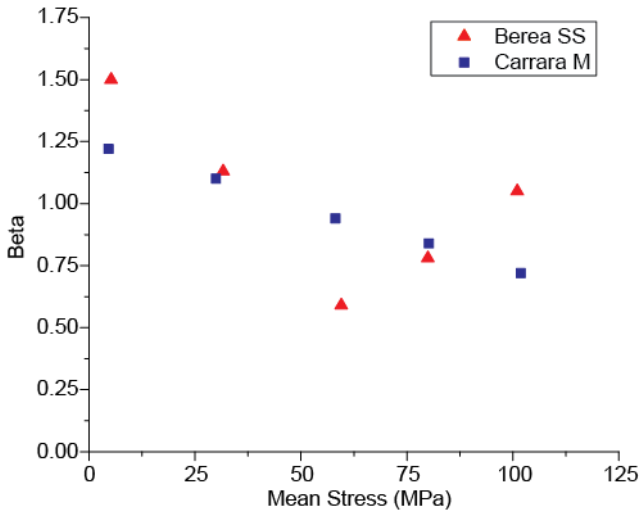

Figure 36. Changes in beta with mean stress. Beta versus mean stress for Berea sandstone, red triangles, and Carrara marble, blue squares.

4.4.2. Carrara Marble

The results for Carrara marble are similar to Berea sandstone. For the five experiments on Carrara marble, all samples fail by the development of a through going fracture. Differential stress and axial strain increased with increasing P_c (Figure 29b). At 10 MPa P_c, the sample exhibit very little plastic strain before failure and have a lower Young's Modulus compared to the other experiments at higher effective pressures, Table 8. At 50 MPa P_c, the sample is stiffer, but still displays little to no plastic strain before failure. At 90 MPa P_c, there is still negligible plastic strain before failure. At 120 and 150 MPa P_c, the samples are stronger and accumulate noticeable plastic strain as axial stress plateaus before failure, indicating the onset of limited crystal plasticity. Previous microstructural observations confirm the presence of twinning at these effective pressures [*Rodriguez,* 2005]. The axial stress at failure for the five effective pressures tested is shown in Figure 30; the relationship is similar to Berea sandstone. At the lowest P_c of 10 MPa, the sample fails in tension with a negative axial stress. With increasing P_c the tensile strength increases before the sample transitions to shear failure with positive axial stress. From 50 to 150 MPa P_c, the increase in axial stress is linear. The relationship between differential stress at failure shows smooth increase in the magnitude of stress with increasing mean stress (Figure 31). All of the samples fail by the development of a through going fracture, but the orientation and morphology vary greatly across the effective pressure range. The relationship between fracture angle and confining pressure is similar to that of the axial stress at failure and effective pressure (Figure 30, Figure 32). At the lowest P_c, the sample fails by a low angle tensile fracture.

With increasing P_c, the fracture angle decreases slightly before increasing as the sample transitions to shear failure. From 50 to 150 MPa P_c, there is a linear increase in fracture angle with effective pressure.

The deformed samples of Carrara marble are shown in Figure 33b. All of the samples broke in the middle of the sample, through the strain gages, except for the experiment deformed at 10 MPa P_c. The latex jacketing prevents the extrusion of plasticene clay post failure for the majority of the samples, preserving the morphology of the newly formed fracture face. The faces of the sample show the same characteristic distribution of gouge, with an increase in gouge with increasing effective pressure that was demonstrated in the Berea sandstone samples. The profile view of the sample deformed at 10 MPa P_c demonstrates that the sample fractured out of the middle of the sample, at roughly one third of the neck, the same location as the Berea sandstone sample. The surface of the sample shows a very rough fracture, with no gouge patches or shear indicators. The rough surface of the fracture reflects the crystallographic faces and cleavage planes of the calcite grain. At 50 MPa P_c, the profile view of the sample demonstrates that the sample fractures in the middle of the neck. The fracture cuts across both of the strain gages. Plascticene modeling clay extrudes into the fracture after failure, making it difficult to determine the amount of gouge on the fracture face. At 90 MPa P_c, the profile of the sample shows the fracture occurred in the center of the neck, cutting both of the strain gages. The fracture face shows patches of gouge arranged in lineaments across the sample, in an en echelon fracture geometry. At 120 MPa P_c, the profile of the sample displays a sharp fracture though the center of the sample, cutting

one of the strain gages. The sample face has a higher proportion of gouge, almost entirely covering the face of the sample. At 150 MPa P_c, the fracture occurs in the middle of the neck and cut one of the strain gages. The fracture face is entirely covered with gouge, and the face is a continuous smooth surface.

The mechanical data from the strain gages for Carrara marble is shown in Figure 37. The strain gages are in an optimal position to capture the behavior as localization occurred due to the geometry of the sample. The behavior measured by the strain gages is similar to the behavior measured externally, except that the strain gages have slightly higher measured strains. At 10 MPa P_c, the sample fails very suddenly, without any appreciable accumulation of inelastic strain. On the gage placed parallel to the fast P wave velocity direction on the sample, there is a lower Young's Modulus and the axial strain displays slight strain softening before failure. The same behavior can be seen on the corresponding lateral component, where there is a reduced modulus and a small increment of strain softening not seen on the other gage. At 50 MPa P_c, the samples failed suddenly with little accumulation of inelastic damage. The strain gage parallel to the fast P wave velocity direction displayed a more noticeable yield and accumulated 0.01% inelastic axial strain prior to failure. This behavior can be observed on the corresponding lateral strain as well, but the effects are muted compared to the axial strain. At 90 MPa P_c, the strain gages accumulates inelastic strain prior to peak strength, and strain softens post peak strength. There is a good agreement between the two strain gages prior to failure. After failure, the gage placed perpendicular to the fast P wave velocity direction is not cut by the fracture, but rather continues to deform post failure.

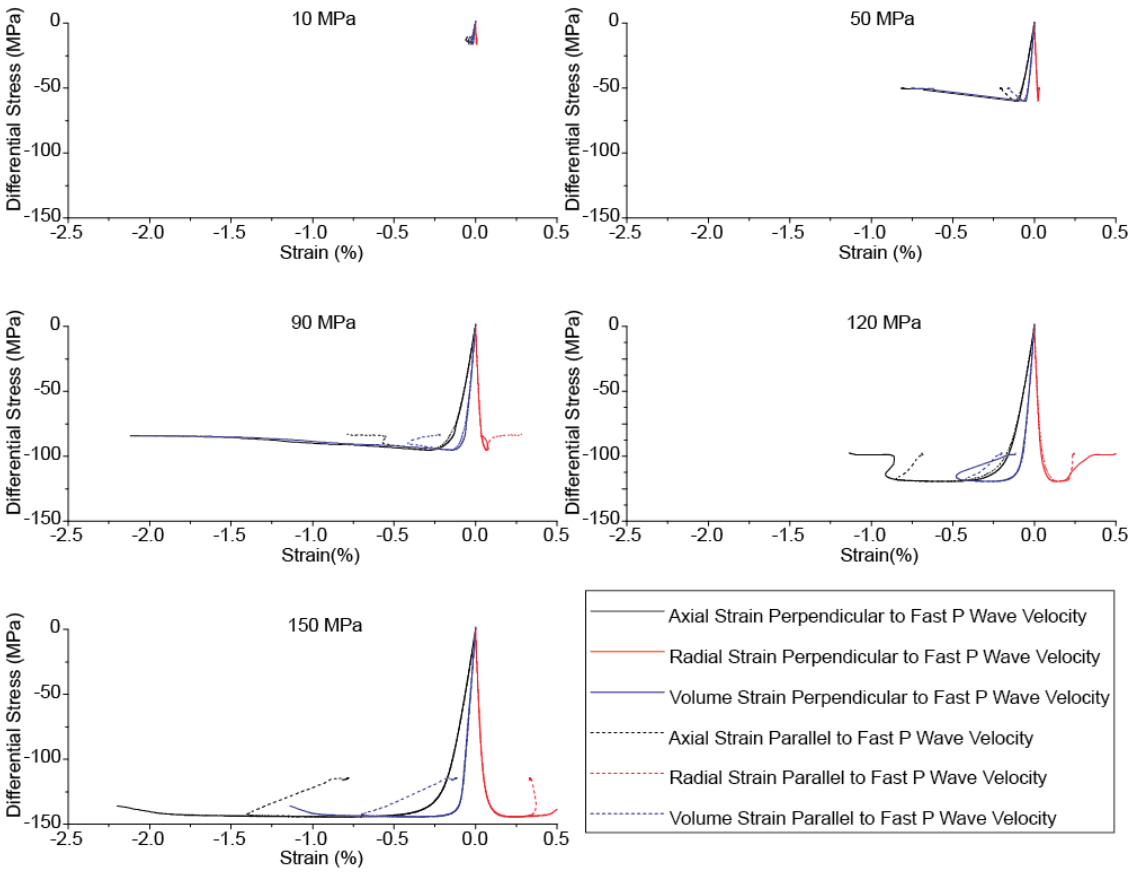

Figure 37. Strain gage results for Carrara marble. Differential stress versus axial (black), lateral (red), and volume strain (blue) for Berea sandstone. Solid curves represent strain gages perpendicular to fast P wave velocity direction, dashed curves represent strain gages perpendicular to fast P wave velocity direction. a) 10 MPa. b) 50 MPa. c) 90 MPa. d) 120 MPa. e.) 150 MPa.

The two lateral strain components agree through failure, the samples yield and strain soften post peak strength, for a total inelastic strain of less than 0.05%. At 120 MPa P_c, the strain gages measure twice the axial strain measured by the external measurements. The lateral strains also noticeably strain for an additional 0.1% after yielding and prior to failure, at nearly constant stress. At 150 MPa P_c, the strain gages again measure twice the axial strain compared to the external measurements. The strain gage perpendicular to the fast P wave is not cut by the fracture, and continued to strain post failure. The behavior of the lateral strains are in good agreement with the axial components, where the gage perpendicular to the fast P wave direction continued to strain for an additional 0.1% with slight strain softening.

The beta versus mu diagram for Carrara marble is shown in Figure 35. The points are annotated with the value of the effective pressure for the experiments. The data for Carrara marble is similar to Berea sandstone, but with less scatter for beta values. The points have positive mu and beta values. There is a decrease in mu and beta values with increasing effective pressure. When beta values are plotted against mean stress in Figure 36, there is a linear relationship similar to Berea sandstone, but with less scatter.

4.5. Discussion

4.5.1. Comparisons to Previous Experimental Results

Experimental investigations investigating the behavior of geomaterials in the tensile to shear transition are limited, due to the difficulty of achieving reproducible

results in this stress field. Previous work suffers from erratic data owing to sample geometry problems, or was not able to investigate the tensile field due to load frame complications. Recent work on Berea sandstone and Carrara marble is able to demonstrate the behavior from the tensile to shear transition with greater accuracy and reproducibility than other studies [*Bobich*, 2005; *Ramsey and Chester*, 2004]. Microstructural investigations of deformed samples from Carrara marble demonstrated key characteristics associated with this transition in stress states: a characteristic fracture morphology, increasing off fault cracking, and decreasing surface roughness [*Rodriguez*, 2005]. The confining pressures in this study follow the conditions from previous experimental work, with the goal of expanding on previous results and microstructural efforts with mechanical behavior at localization from the strain gages adhered to the neck. Confining pressures chosen for Berea sandstone and Carrara marble correspond to characteristic behavior: 10 MPa P_c corresponding the tensile failure, 50 MPa P_c corresponding to the greatest tensile strength, 90 MPa P_c corresponding to tensile hybrid behavior, 120 MPa P_c corresponding to shear hybrid behavior, and 150 MPa P_c corresponding to shear behavior.

Figure 38 compares the failure strength for Berea sandstone from this study against previous work by Bobich, 2005. The results presented here agree well with the previous work, following the same envelope with similar failure strengths: the tensile strength increases with increasing effective pressure before a linear transition to shear behavior. The results from this study are systematically weaker than the results from Bobich, 2005. The differences in strength could be attributed to differences from the

different blocks of Berea sandstone used in the two studies. The strain gage application could have also had an effect; the Ultracal 30 and adhesive could have created minor stress concentrations in the neighboring regions. Figure 39 compares the fracture angles for Berea sandstone from this study against previous work by Bobich, 2005. The fracture angle measurements from this study are in agreement with the previous work. Due to the porous and heterogeneous nature of Berea sandstone, the measurements are scattered. The data show that at low P_c, the fracture angles are very low values, less than 5 degrees. Over 50 MPa P_c, both sets of data can be fit the same trend to describe the linear increase in fracture angle with increasing effective pressure.

The failure strengths and fracture angles for Carrara marble from this study are in excellent agreement with previous results from Ramsey and Chester, 2004. Figure 40 compares the failure strengths for Carrara marble against previous results. The failure strengths reported here are within 1 MPa for the conditions tested here, despite using a different block of material and an altered experimental setup. The results from this study reinforce the shape of the failure envelope; the tensile strength increases with increasing P_c, before a linear transition to shear behavior. Figure 41 compares the measured fracture angles for Carrara marble against previous results from Ramsey and Chester, 2004. There is excellent agreement between the two data sets. Because Carrara marble is a monominerallic, crystalline material, the fracture angle is well defined. The data from both studies on Carrara marble demonstrate that at low effective pressures, the fracture angles are very low, less than 3 degrees. Over 50 MPa P_c, there is a linear increase in fracture angle with increasing effective pressure.

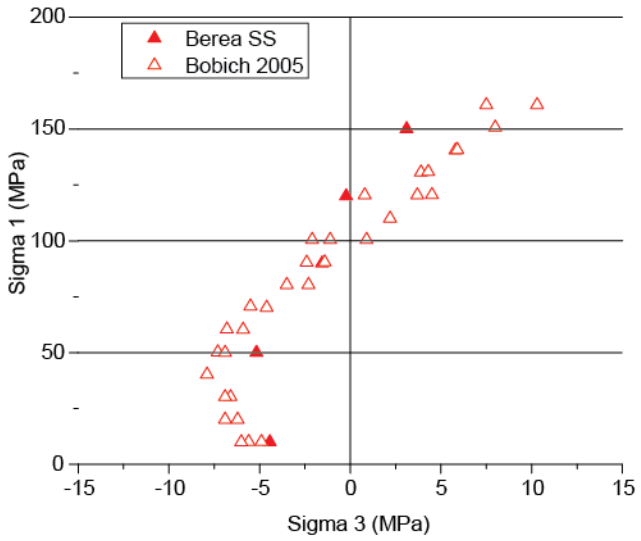

Figure 38. Failure strength comparison to previous work for Berea sandstone. Failure strengths from this study, solid symbols, compared to previous work, open symbols in σ_1 - σ_3 space.

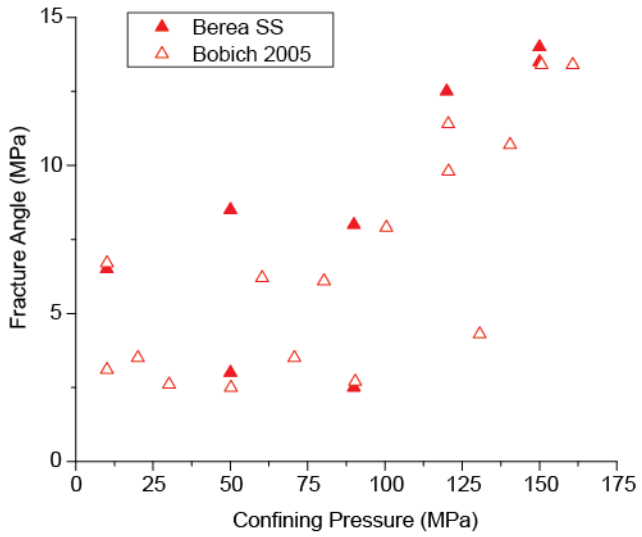

Figure 39. Fracture angle comparison to previous work for Berea sandstone. Fracture angles from this study, solid symbols, compared to previous work, open symbols in plotted against confining pressure.

4.5.2. Comparisons against Analog Materials

Bifurcation analysis based on localization theory has been tested extensively for geomaterials in the compressional stress states, with good success [*Baud et al.*, 2006; *Besuelle*, 2001; *Herrin*, 2008]. The approach is able to predict the fracture angles, as well as the mode of failure for dilation, shear, and compaction bands. Previous work has focused on defining the behavior of shear and compaction bands, but to date, no studies on natural rocks have focused on the behavior of dilation bands. There is previous work utilizing a synthetic rock analog, titanium dioxide, TiO_2, to investigate the behavior of dilation bands and shear bands in both triaxial compression and triaxial extension [*Chemenda et al.*, 2011; *Nguyen et al.*, 2011]. The work on TiO_2 uses a different geometry and loading procedure than this study. The authors use a different variation of the dogbone geometry, with a constant diameter neck and a fillet transition to the sample shoulders. The constant radius neck allows them to instrument the neck section with linear voltage displacement transducers to calculate the necessary parameters for bifurcation analysis. To generate tensile force, the piston pulls the top platen against the upper transition of the sample neck. While creating a neck with a constant diameter to measure parameters, the geometry and loading procedure create stress concentrations at the fillet between the neck and the shoulder that localizes failure at this transition point, outside of the instrumented area. Observations of the fractured samples show that the majority of their samples failed at this transition point.

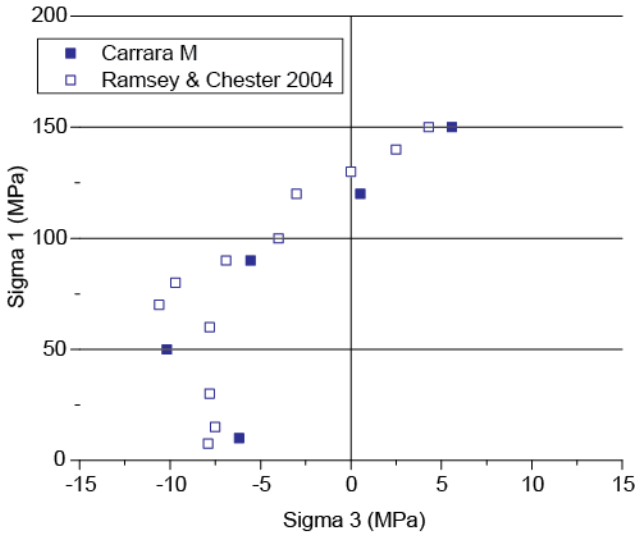

Figure 40. Failure strength comparison to previous work for Carrara marble. Failure strengths from this study, solid symbols, compared to previous work, open symbols in σ_1 - σ_3 space.

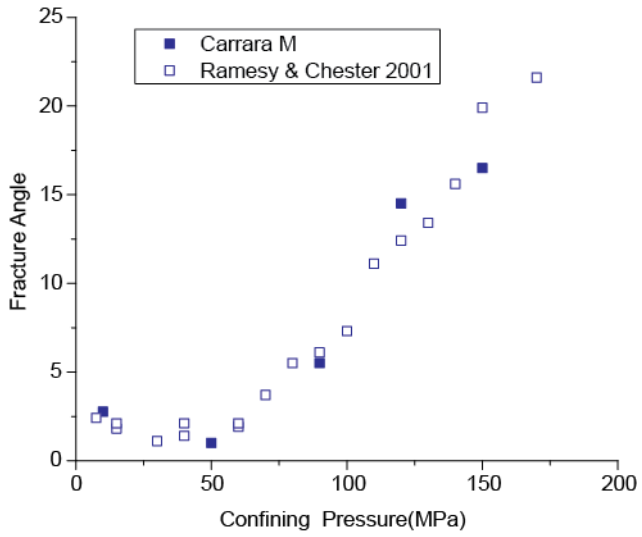

Figure 41. Fracture angle comparison to previous work for Carrara marble. Fracture angles from this study, solid symbols, compared to previous work, open symbols in plotted against confining pressure.

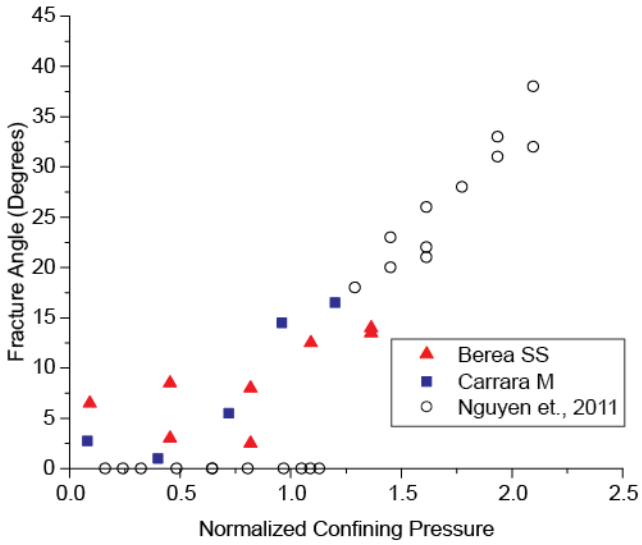

Figure 42. Fracture angle comparison to different materials. Fracture angles versus normalized confining pressure for Berea sandstone, red triangles, Carrara marble, blue squares, and titanium dioxide from *Nguyen et al.*, [2011], open circles.

Figure 42 compares the measured fracture angles from Nguyen et al., 2011, against to the measured values for Berea sandstone and Carrara marble from this study. To facilitate comparison, the confining pressure for each experiment is normalized by the material's unconfined compressive strength, derived from the triaxial extension stress state. The fracture angles agree in the tensile and shear regimes, but not the hybrid regime. In the tensile field, the analog material fractures at a consistent 0° angle, most likely due to a much finer grain size and more homogenous nature compared to the natural materials. For shear fractures, the analog material fracture angle increase at the same rate with increasing P_c as natural materials. For the hybrid fractures, the analog material does not see the gradual transition seen in natural material. The fracture angles jump from 0° to 18°; there are no low angle fractures observed. This is likely due to the sample geometry employed the analog material; the stress concentration at the transition between the neck and shoulder localizes failure and dominates the fracture behavior until the stress is compressive enough to fail in a pure shear mode.

The failure strengths observed in the analog material do not agree with the failure strengths observed in Berea sandstone and Carrara marble, Figure 43. The stresses for each material are normalized by their respective tensile strength to facilitate comparison between the different strength materials. Both Berea sandstone and Carrara marble show a slight increase in tensile strength with increasing P_c, and this is not seen in the analog material. The tensile strength remains constant with increasing effective pressure for the analog material. For the natural materials, the slopes change to a positive value at around 7-8 times the value of T_0. This slope change occurs at a slightly higher value for

the analog material, but the subsequent shear behavior is different. The natural materials have a much steeper slope than the analog material. Despite continuously increasing P_c, there is noticeable gap in axial strength for the analog material as it transitions from tensile to shear behavior, at the same stress state where there is disagreement in the fracture angles. Figure 43 compares the calculated beta values from experiment on the analog material by Nguyen et al., 2011, against the values calculated for Berea sandstone and Carrara marble for this study. For the analog material, the beta values are positive; the values are initially constant before decreasing in value with increasing mean stress. The authors also do not report any beta values in tension. This study demonstrates a positive beta values with a higher magnitude than TiO_2. With increasing mean stress, there is a decrease in beta for the natural materials. The combined data demonstrates a linear decrease with increasing mean stress for the experiments conducted here and the higher mean stress experiments on TiO_2. The lowest mean stress values for TiO_2 do not agree with the results from the natural materials. A possible reason behind the disagreement between the two materials could be sample geometry. The constant diameter dogbone affects the fracture angle and location, Figure 42, and this in turn could affect beta values. Because the fracturing occurs at the transition between the shoulder and the neck of the samples, the displacement transducers are not measuring behavior as localization occurs, unlike the strain gage measurements from this study. Additionally, beta values measured from this study are at lower comparative mean stresses than Nguyen et al., 2011. The lowest mean stress where beta is calculate for

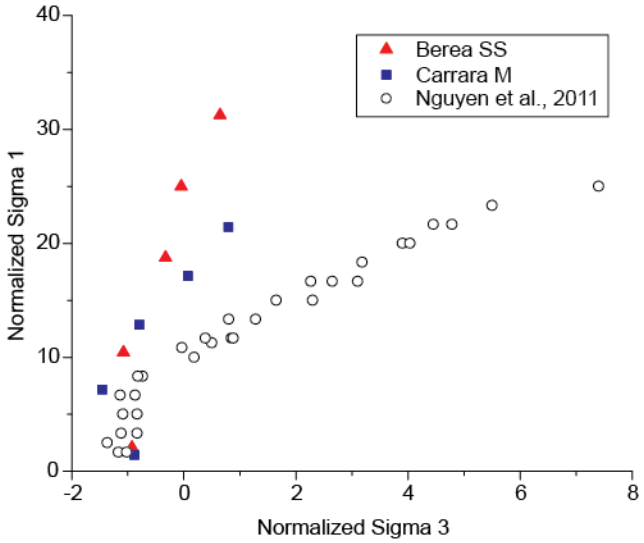

Figure 43. Failure strength comparison to different material. Failure strengths of Berea sandstone, red triangles, Carrara marble, blue squares, and titanium dioxide from *Nguyen et al.*, [2011], open circles in normalized σ_1 - σ_3 space.

TiO_2 corresponds to the end of the transitional behavior for Berea sandstone and Carrara marble, where there is disagreement in fracture angle and failure strength).

4.5.3. Comparisons against Theory

The derived parameters of beta and mu can be used to compare the experimental results for Berea sandstone and Carrara marble against predictions from localization theory formulated by Rundnicki and Rice, 1975, and others. The measured fracture angles from experiments are compared to predicted values using Equation 9, Figure 44. The measured angles are low values for the two lowest confining pressures tested, that subsequently show a linear increase in fracture angle for the highest confining pressures tested The predicted angles do not match the measured values. The predicted values are much higher than the measured values, 10 to 25°, for all confining pressures tested. The predicted values do not match the trends displayed by the measured values, either. The predicted values for Carrara marble show a linear increase for the three highest confining pressures, but do not display the constant values at the lowest confining pressures tested. The predicted values for Berea sandstone do not match the trend from measured values. The predicted values show a sharp increase in fracture angle with increasing confining pressure, then a decrease in fracture angle at the two highest confining pressures tested, the opposite of the measured values. The mismatch for the predicted fracture angles reflects the variability in the determined values of beta and mu.

The theory can also be used to predict the type of failure, dilation, shear, or compaction, for given values of beta and mu. Issen and Challa, 2008, derived band

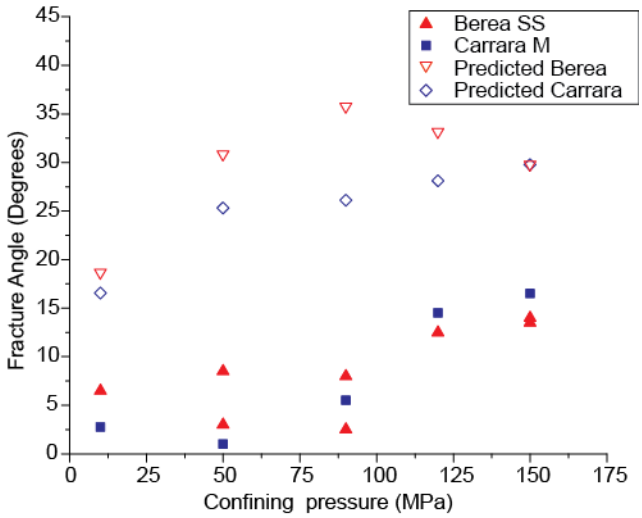

Figure 44. Measured fracture angles versus predictions from localization theory. Fracture angles for Berea sandstone, red triangles, and Carrara marble, blue squares, plotted against confining pressure. Experimental values are solid symbols, predictions are open symbols.

types for triaxial extension stress states for different yield surface models describing the behavior of porous rocks. They derived a two yield surface model based on a linear Coulomb envelope for shear bands and elliptical CAP for compaction bands, and a single yield surface where one smooth envelope describes the behavior in both regimes. Figure 45 compares the beta and mu values from the experiments on Berea sandstone and Carrara marble against the predicted band types for the one yield-surface analysis from Issen and Challa, 2008. Mechanical responses and physical observations of fracture faces indicate that samples deformed at 10 and 50 MPa P_c form dilation bands, samples deformed at 150 MPa P_c form shear bands, and samples at intermediate values of 90 and 120 MPa P_c form hybrid fractures. Figure 45a compares the experimental results against the predictions of the one yield surface model. The model predict dilation bands for Berea sandstone at 10 and 50 MPa P_c, and for Carrara marble at 50 MPa P_c. The model predicts shear bands for Berea sandstone at 150 MPa P_c, and for Carrara at 90 and 120 MPa P_c. These predictions agree with the experimental observations. There is no band type predicted for Berea sandstone at confining pressures of 90 and 120 MPa P_c, and Carrara marble at confining pressures of 10 and 150 MPa; the model does not predict the experimental values could occur.

Figure 45b compares the experimental results against the predictions of the two-yield surface model. The model correctly predicts dilation bands fore Berea sandstone and Carrara marble at 10 MPa P_c. The model also correctly predicts shear bands for Berea sandstone at 150 MPa P_c, and Carrara marble at 90 and 120 MPa P_c. The model predicts shear bands for both rocks at 50 MPa P_c; observations would suggest that at this

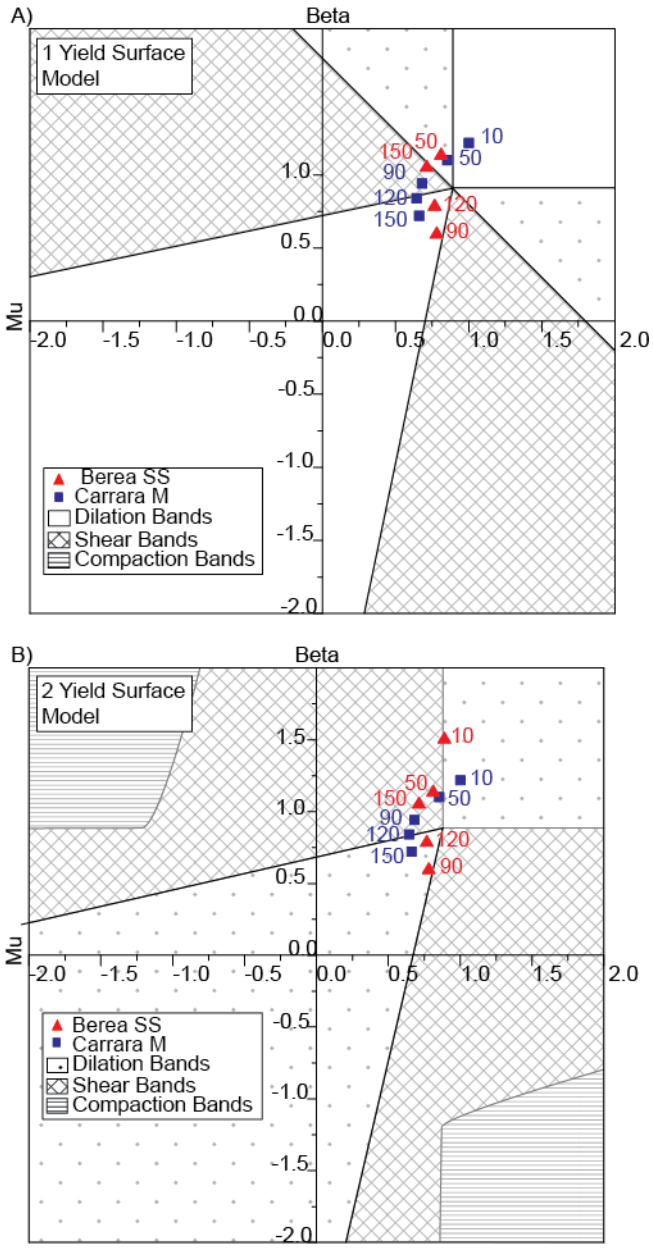

Figure 45. Beta mu plots for different yield surface models. Beta versus mu for Berea sandstone, red triangles, and Carrara marble, blue squares. Values annotated with experimental conditions. Results are compred to predicted band types from *Issen and Challa*, [2008] derived for triaxial extension stress state. Dilation bands, stippled, shear bands, cross hatched, and compcation bands, lined. a) Predictions for one yield surface model. b) Predictions for two yield surface model.

condition the rocks are a tension dominated failure, with little shear component. The values are close to the dilation shear band transition though. The model incorrectly predicts dilation band for Berea sandstone at 90 and 120 MPa P_c, and Carrara marble at 150 MPa P_c. Out of the two models, the two yield surface is the more accurate model in predicting band types. However, neither model is accurate at the highest confining pressures tested; the decreasing beta and mu values seen in Berea sandstone and Carrara marble suggest that the model would not be able to predict shear bands at higher confining pressures than those of this study.

4.6. Conclusion

Despite the contrasting lithology, the mechanical responses of Berea sandstone and Carrara marble are similar. Failure strength, stiffness, and inelastic strain prior to failure increase with increasing P_c. In sigma 1 versus sigma 3 space, the axial stress decreases with increasing P_c up to 50 MPa, then increases linearly. Differential stress increases linearly with increasing mean stress. The fracture orientations for the two rock types are similar as well, a constant low value for the two lowest confining pressures tested, and then a linear increase after 50 P_c. Physical observation of the fracture faces qualitatively demonstrate the modes of fracture active in the through going deformation band. The failure strengths and fracture orientations recorded here agree very well with the previous experiments of *Ramsey,* [2001] and *Bobich,* [2004], but not of *Nguyen et al.,* [2011].

The strain gages successfully recorded the mechanical behavior in the local area where failure occurs for all the samples tested. Beta and mu values are calculated for the first time for natural materials in this stress state. Beta and mu are positive, and decrease with increasing confining pressure. The values for Carrara show a linear decrease; the values for Berea follow the same trend but with more scatter.

The beta and mu values allowed an investigation of bifurcation analysis for the first time in this stress state for geomaterials. The framework derived by Rudnicki and Rice, 1975, is not able to predict the observed fracture orientations. A later derivation by Issen and Challa, 2008, is able to predict some of the observed deformation band types. Out of the published models, the model based on two yield surfaces is more accurate.

5. SUMMARY

Experiments were conducted on five different materials, loose quartz sand, Berea sandstone, Carrara marble, Indiana limestone, and Kansas chalk. Experimental conditions ranged from isostatic loading to triaxial extension, room temperature to 200° C, and time durations from several minutes to several months. The study was designed to better elucidate naturally occurring phenomena through experimental rock deformation.

The experiments on quartz sand demonstrate that the theory of parallel consolidation curves developed by Bjerrum, 1967, for normally consolidated clay rich soils, can be employed to describe the behavior observed in this study on quartz sand. The plastic consolidation curves for St. Peter sand can be described by a series of parallel envelopes with two different slopes separated by the critical pressure, P^*. P^* decreases with increasing temperature and decreasing plastic volume-strain rate. Individually, increases in temperature and decreases in strain rate result in modest reductions in P^*. However, the combined effects of temperature and strain rate are substantial. The Bjerrum model allows creep experiments to interpret P^* at even lower strain rates that would be prohibitive in consolidation experiments. Predicted values of P^* for geologic strain rates are less than half of the results from the room temperature standard laboratory strain rate experiment. Burial depths corresponding to the predicted P^* values correlate with porosity reduction trends seen in nature, particularly offshore Norway. This demonstrates that typical experiments greatly over predict the strength of

granular material, and temperature and strain rate effects must be considered when extrapolating to in situ conditions.

Triaxial extension experiments have demonstrated that there is a characteristic, universal behavior in this transitional stress state for failure strength, damage evolution, and fracture angle. All rock types show the same trends with increasing mean stress. Differential stress at failure, inelastic strain prior to failure, and apparent stiffness all increase with increasing mean stress. The experiments show that the tensile strength of the material increases with increasing mean stress, until the behavior begins to transition to shear behavior

Comparisons against the Griffith and modified Griffith criterions show that the conventional approaches to defining the extension to shear transition are not capable of matching experimental observations. The Griffith based criterions are not able to predict the observed failure strengths, fracture orientation, or UCS:T_0 ratios. The three variable concrete model is able to predict the failure strength in triaxial compression and extension stress states, but is not capable of predicting fracture orientations or tensile behavior. Extensions of the criterion to standard criterions are not as accurate as the generalized form.

The experiments presented here can be used as a basis for an empirical failure envelope. The envelope is divided into two segments above and below σ_1 values of 0.5UES to predict the distinctive behavior seen in failure strength and fracture angles. The failure envelope can be combined with fracture mechanics predictions of stress perturbations around an internally pressurized crack tip growing off a wellbore to better

understand hydraulic fracture behavior. The approach is better able to predict the microseismic sources and distributions seen in the Carthage Cotton Valley stimulation than the conventional approach based on the Griffith criterion.

For the study of bifurcation analysis, the strain gages successfully recorded the mechanical behavior in the local region where failure occurs for all the samples tested. Beta and mu values are calculated for the first time for natural materials in this stress state. Beta and mu are positive, and decrease with increasing confining pressure. The values for Carrara show a linear decrease; the values for Berea follow the same trend but with more scatter.

The beta and mu values allowed an investigation of bifurcation analysis for the first time in this stress state for geomaterials. The framework derived by Rudnicki and Rice, 1975, is not able to predict the observed fracture orientations. A later derivation by Issen and Challa, 2008, is able to predict some of the observed deformation band types. Out of the published models, the model based on two yield surfaces is more accurate.

REFERENCES

Angelier, J., F. Bergerat, O. Dauteuil, and T. Villemin (1997), Effective tension-shear relationships in extensional fissure swarms, axial rift zone of northeastern Iceland, *J. Struct. Geol.*, *19*(5), 673-685, doi:10.1016/s0191-8141(96)00106-x.

Atkinson, B. K. (1982), Subcritical crack propagation in rocks: theory, experimental results and applications, *J. Struct. Geol.*, *4*(1), 41-56.

Augustesen, A., M. Liingaard, and P. V. Lade (2004), Evaluation of Time-Dependent Behavior of Soils, *International Journal of Geomechanics*, *4*(3), 137-156, doi:10.1061/(asce)1532-3641(2004)4:3(137).

Baud, P., V. Vajdova, and T. F. Wong (2006), Shear-enhanced compaction and strain localization: Inelastic deformation and constitutive modeling of four porous sandstones, *J. Geophys. Res.-Solid Earth*, *111*(B12), 17, doi:B12401 10.1029/2005jb004101.

Baud, P., W. L. Zhu, and T. F. Wong (2000), Failure mode and weakening effect of water on sandstone, *J. Geophys. Res.-Solid Earth*, *105*(B7), 16371-16389.

Beeler, N. (2012), Re-estimated effects of deep episodic slip on the occurrence and probability of great earthquakes in Cascadia: Delayed failure, *Bull. Seismol. Soc. Am.*

Bernabe, Y., and W. Brace (1990), Deformation and fracture of Berea sandstone, *The brittle-ductile transition in rocks*, 91-101.

Besuelle, P. (2001), Compacting and dilating shear bands in porous rock: Theoretical and experimental conditions, *J. Geophys. Res.-Solid Earth*, *106*(B7), 13435-13442, doi:10.1029/2001jb900011.

Besuelle, P., J. Desrues, and S. Raynaud (2000), Experimental characterisation of the localisation phenomenon inside a Vosges sandstone in a triaxial cell, *Int. J. Rock Mech. Min. Sci.*, *37*(8), 1223-1237, doi:10.1016/s1365-1609(00)00057-5.

Bjerrum, L. (1967), Engineering geology of Norwegian normally-consolidated marine clays as related to settlements of buildings, *Geotechnique*, *17*(2), 83-118.

Blackwell, D. D., P. T. Negraru, and M. C. Richards (2006), Assessment of the enhanced geothermal system resource base of the United States, *Natural Resources Research*, *15*(4), 283-308.

Bloch, S., R. Suchecki, J. Duncan, and K. Bjorlykke (1986), Porosity prediction in quartz-rich sandstones: Middle Jurassic, Haltenbanken area, offshore central Norway, *AAPG Bull.*, *70*(CONF-860624-).

Bobich, J. K. (2005), Experimental analysis of the extension to shear fracture transition in Berea sandstone, Texas A&M.

Brace, W. F. (1964), Brittle fracture of rocks, in *State of stress in the Earth's crust*, edited by W. R. Judd, pp. 111-180, American Elsevier, New York.

Bureau, D., R. Mourgues, J. Cartwright, M. Foschi, and M. Abdelmalak (2013), Characterisation of interactions between a pre-existing polygonal fault system and sandstone intrusions and the determination of paleo-stresses in the Faroe-Shetland basin, *J. Struct. Geol.*, *46*, 186-199.

Busetti, S., W. Jiao, and Z. e. Reches (2014), Geomechanics of hydraulic fracturing microseismicity: Part 1. Shear, hybrid, and tensile events, *AAPG Bull.*, *98*(11), 2439-2457.

Chamberlain, C. J., D. R. Shelly, J. Townend, and T. A. Stern (2014), Low-frequency earthquakes reveal punctuated slow slip on the deep extent of the Alpine Fault, New Zealand, *Geochemistry, Geophysics, Geosystems*, *15*(7), 2984-2999.

Chemenda, A. I., S. H. Nguyen, J. P. Petit, and J. Ambre (2011), Mode I cracking versus dilatancy banding: Experimental constraints on the mechanisms of extension fracturing, *Journal of Geophysical Research: Solid Earth*, *116*(B4), B04401, doi:10.1029/2010jb008104.

Chester, F. M. (1994), Effects of temperature on friction - Constitutive -equations and experiments with quartz gouge, *J. Geophys. Res.-Solid Earth*, *99*(B4), 7247-7261.

Chester, F. M., J. S. Chester, A. K. Kronenberg, and A. Hajash (2007), Subcritical creep compaction of quartz sand at diagenetic conditions: Effects of water and grain size, *J. Geophys. Res.-Solid Earth*, *112*(B6), 15, doi:B06203 10.1029/2006jb004317.

Chester, J. S., F. M. Chester, and A. K. Kronenberg (2005), Fracture surface energy of the Punchbowl fault, San Andreas system, *Nature*, *437*(7055), 133-136, doi:10.1038/nature03942.

Chester, J. S., S. C. Lenz, F. M. Chester, and R. A. Lang (2004), Mechanisms of compaction of quartz sand at diagenetic conditions, *Earth and Planetary Science Letters*, *220*(3-4), 435-451, doi:10.1016/s0012-821x(04)00054-8.

Choens, R. C., and F. M. Chester (2014), Characterizing Damage Evolution and Yield Surfaces for Berea Sandstone Under Triaxial Loading as a Function of Effective Pressure, in *48th US Rock Mechanics/Geomechanics Symposium*, edited, American Rock Mechanics Association, Minneapolis, Minnesota.

Churcher, P., P. French, J. Shaw, and L. Schramm (1991), Rock properties of Berea sandstone, Baker dolomite, and Indiana limestone, in *SPE International Symposium on Oilfield Chemistry*, edited, Society of Petroleum Engineers.

Cipolla, C. L., N. R. Warpinski, M. J. Mayerhofer, E. Lolon, and M. C. Vincent (2008), The relationship between fracture complexity, reservoir properties, and fracture treatment design, in *SPE Annual Technical Conference and Exhibition*, edited, Society of Petroleum Engineers, Denver, Colorado, USA, doi:10.2118/115769-ms.

Cosgrove, J. W. (2001), Hydraulic fracturing during the formation and deformation of a basin: A factor in the dewatering of low-permeability sediments, *AAPG Bull.*, *85*(4), 737-748.

Cox, S. F., S. S. Sun, M. A. Etheridge, V. J. Wall, and T. F. Potter (1995), Structural and geochemical controls on the development of turbidite-hosted gold quartz vein deposits, Wattle Gully mine, central Victoria, Australia, *Economic Geology and the Bulletin of the Society of Economic Geologists*, *90*(6), 1722-1746.

Daub, E. G., D. R. Shelly, R. A. Guyer, and P. A. Johnson (2011), Brittle and ductile friction and the physics of tectonic tremor, *Geophys. Res. Lett.*, *38*, doi:10.1029/2011gl046866.

Davatzes, N. C., A. Aydin, and P. Eichhubl (2003), Overprinting faulting mechanisms during the development of multiple fault sets in sandstone, Chimney Rock fault array, Utah, USA, *Tectonophysics*, *363*(1), 1-18.

David, C., T. F. Wong, W. L. Zhu, and J. X. Zhang (1994), Laboratory measurements of compaction-induced permeability change in porous rocks - Implications for the generation and maintenance of pore pressure excess in the crust, *Pure Appl. Geophys.*, *143*(1-3), 425-456.

Delaney, P. T., D. D. Pollard, J. I. Ziony, and E. H. McKee (1986), Field relations between dikes and joints - Emplacement processes and paleostress analysis, *Journal of Geophysical Research-Solid Earth and Planets*, *91*(B5), 4920-4938, doi:10.1029/JB091iB05p04920.

Dewers, T., and A. Hajash (1995), Rate Laws for Water-Assisted Compaction and Stress-Induced Water-Rock Interaction in Sandstones, *J. Geophys. Res.-Solid Earth*, *100*(B7), 13093-13112, doi:Doi 10.1029/95jb00912.

DiMaggio, F. L., and I. S. Sandler (1971), Material model for granular soils, *Journal of the Engineering mechanics Division*, *97*(3), 935-950.

Dove, P. M. (1995), Geochemical controls on the kinetics of quartz fracture at subcritical tensile stresses, *J. Geophys. Res.-Solid Earth*, *100*(B11), 22349-22359.

Elias, B. P., and A. Hajash (1992), Changes in quartz solubility and porosity due to effective stress: An experimental investigation of pressure solution, *Geology*, *20*(5), 451-454.

Engelder, T. (1999), Transitional–tensile fracture propagation: a status report, *J. Struct. Geol.*, *21*(8), 1049-1055.

Ferrill, D. A., R. N. McGinnis, A. P. Morris, and K. J. Smart (2012), Hybrid failure: Field evidence and influence on fault refraction, *J. Struct. Geol.*, *42*, 140-150.

Fischer, T., and A. Guest (2011), Shear and tensile earthquakes caused by fluid injection, *Geophys. Res. Lett.*, *38*, doi:L05307 10.1029/2010gl045447.

Fisher, M. K., and N. R. Warpinski (2011), Hydraulic fracture-height growth: Real data, in *SPE Annual Technical Conference and Exhibition*, edited, Society of Petroleum Engineers, Denver, Colorado, USA, doi:10.2118/145949-ms.

Fjaer, E. (2008), *Petroleum related rock mechanics*, 2nd ed., xxii, 491 p. pp., Elsevier, Amsterdam ; Boston.

Foulger, G. R., B. R. Julian, D. P. Hill, A. M. Pitt, P. E. Malin, and E. Shalev (2004), Non-double-couple microearthquakes at Long Valley caldera, California, provide evidence for hydraulic fracturing, *J. Volcanol. Geotherm. Res.*, *132*(1), 45-71, doi:10.1016/s0377-0273(03)00420-7.

Fredrich, J. T., B. Evans, and T. F. Wong (1989), Micromechanics of the brittle to plastic transition in Carrara marble, *Journal of Geophysical Research-Solid Earth and Planets*, *94*(B4), 4129-4145, doi:10.1029/JB094iB04p04129.

Freiman, S. (1984), Effects of chemical environments on slow crack growth in glasses and ceramics, *Journal of Geophysical Research: Solid Earth (1978–2012)*, *89*(B6), 4072-4076.

Gangi, A. F. (1978), Variation of whole and fractured porous rock permeability with confining pressure, *Int. J. Rock Mech. Min. Sci.*, *15*(5), 249-257.

Garlanger, J. E. (1972), The consolidation of soils exhibiting creep under constant effective stress, *Geotechnique*, *22*(1), 71-78.

Gross, M. R., and T. Engelder (1995), Strain accommodated by brittle failure in adjacent units of the Monterey formation, USA - Scale effects and evidence for uniform displacement boundary-conditions, *J. Struct. Geol.*, *17*(9), 1303-&, doi:10.1016/0191-8141(95)00011-2.

Haddadi, D. (2013), An investigation of permeability and porosity evolution of Kansas chalk under in-situ conditions, University of Stavnager.

Haimson, B., and J. W. Rudnicki (2010), The effect of the intermediate principal stress on fault formation and fault angle in siltstone, *J. Struct. Geol.*, *32*(11), 1701-1711, doi:10.1016/j.jsg.2009.08.017.

Hajash, A., and M. A. Bloom (1991), Marine diagenesis of feldspathic sand: A flow-through experimental study at 200 C, 1 kbar, *Chem Geol*, *89*(3), 359-377.

Hancock, P. (1985), Brittle microtectonics: principles and practice, *J. Struct. Geol.*, *7*(3), 437-457.

Hart, D. J., and H. F. Wang (1995), Laboratory measurements of a complete set of poroelastic moduli for Berea sandstone and Indiana limestone, *Journal of Geophysical Research: Solid Earth (1978–2012)*, *100*(B9), 17741-17751.

Hattin, D. E. (1981), Petrology of Smoky Hill Member, Niobrara Chalk (Upper Cretaceous), in type area, western Kansas, *AAPG Bull.*, *65*(5), 831-849.

He, W., A. Hajash, and D. Sparks (2003), Creep compaction of quartz aggregates: Effects of pore-fluid flow—A combined experimental and theoretical study, *Am. J. Sci.*, *303*(2), 73-93.

He, W., D. Sparks, and A. Hajash (2013), Reactive transport at stressed grain contact and creep compaction of quartz sand, *J. Geophys. Res.-Solid Earth*, *118*(2), 497-510, doi:Doi 10.1002/Jgrb.50064.

Herrin, E. A. (2008), Experimental Study of Shear and Compaction Band Formation in Berea Sandstone, Texas A&M University, College Station, Texas.

Hettema, M. H. H., P. M. T. M. Schutjens, B. J. M. Verboom, and H. J. Gussinklo (2000), Production-Induced Compaction of a Sandstone Reservoir: The Strong Influence of Stress Path, *SPE Reservoir Evaluation & Engineering*, doi:10.2118/65410-PA.

Hill, D. P. (1977), Model for earthquake swarms, *Journal of Geophysical Research*, *82*(8), 1347-1352, doi:10.1029/JB082i008p01347.

Hillard, J. E., and L. R. Lawson (2003), *Stereology and Stochastic Geometry*, Kluwer Academic Publishers, Dordrecht, The Netherlands.

Holcomb, D. J., and W. A. Olsson (2003), Compaction localization and fluid flow, *J. Geophys. Res.-Solid Earth, 108*(B6), 13, doi:2290 10.1029/2001jb000813.

Holcomb, D. J., and J. W. Rudnicki (2001), Inelastic constitutive properties and shear localization in Tennessee marble, *Int. J. Numer. Anal. Methods Geomech.*, *25*(2), 109-129.

Holtz, R. D., and W. D. Kovacs (1981), *An introduction to geotechnical engineering*, 747 pp., Prentice-Hall, Incorporated, Englewood Cliffs, New Jersey.

Ide, S., D. R. Shelly, and G. C. Beroza (2007), Mechanism of deep low frequency earthquakes: Further evidence that deep non-volcanic tremor is generated by shear slip on the plate interface, *Geophys. Res. Lett.*, *34*(3), doi:10.1029/2006gl028890.

Ingraham, M. D., K. A. Issen, and D. J. Holcomb (2013), Response of Castlegate sandstone to true triaxial states of stress, *Journal of Geophysical Research: Solid Earth*, n/a-n/a, doi:10.1002/jgrb.50084.

Issen, K. A. (2002), The influence of constitutive models on localization conditions for porous rock, *Eng. Fract. Mech.*, *69*(17), 1891-1906.

Issen, K. A., and V. Challa (2008), Influence of the intermediate principal stress on the strain localization mode in porous sandstone, *Journal of Geophysical Research: Solid Earth*, *113*(B2), B02103, doi:10.1029/2005jb004008.

Issen, K. A., and J. W. Rudnicki (2001), Theory of compaction bands in porous rock, *Phys. Chem. Earth Pt. A-Solid Earth Geod.*, *26*(1-2), 95-100.

Jaeger, J. C., N. G. Cook, and R. Zimmerman (2009), *Fundamentals of rock mechanics*, John Wiley & Sons.

Ji, Y., P. Baud, V. Vajdova, and T.-f. Wong (2012), Characterization of pore geometry of Indiana limestone in relation to mechanical compaction, *Oil & Gas Science and Technology–Revue d'IFP Energies nouvelles*, *67*(5), 753-775.

Julian, B. R., A. D. Miller, and G. R. Foulger (1998), Non-double-couple earthquakes 1. Theory, *Rev. Geophys.*, *36*(4), 525-549, doi:10.1029/98rg00716.

Karig, D. E., and M. V. S. Ask (2003), Geological perspectives on consolidation of clay-rich marine sediments, *Journal of Geophysical Research: Solid Earth (1978–2012)*, *108*(B4).

Karig, D. E., and G. Hou (1992), High-stress consolidation experiments and their geologic implications, *J. Geophys. Res.-Solid Earth*, *97*(B1), 289-300.

Karner, S. L., F. M. Chester, A. K. Kronenberg, and J. S. Chester (2003), Subcritical compaction and yielding of granular quartz sand, *Tectonophysics*, *377*(3-4), 357-381, doi:10.1016/j.tecto.2003.10.006.

Karner, S. L., J. S. Chester, F. M. Chester, A. K. Kronenberg, and A. Hajash (2005), Laboratory deformation of granular quartz sand: Implications for the burial of clastic rocks, *AAPG Bull.*, *89*(5), 603-625, doi:10.1306/12200404010.

Karner, S. L., A. K. Kronenberg, F. M. Chester, J. S. Chester, and A. Hajash (2008), Hydrothermal deformation of granular quartz sand, *J. Geophys. Res.-Solid Earth*, *113*(B5), 12, doi:B05404
10.1029/2006jb004710.

Katz, O., and E. Aharonov (2006), Landslides in vibrating sand box: What controls types of slope failure and frequency magnitude relations?, *Earth and Planetary Science Letters*, *247*(3), 280-294.

Labuz, J. F., and J. M. Bridell (1993), Reducing frictional constrain in compression testing through lubrication, *International Journal of Rock Mechanics and Mining Sciences & Geomechanics Abstracts*, *30*(4), 451-455.

Lafollette, R., W. D. Holcomb, and J. Aragon (2012), Impact of completion system, staging, and hydraulic fracturing trends in the Bakken Formation of the Eastern

Williston Basin, in *SPE Hydraulic Fracturing Technology Conference*, edited, Society of Petroleum Engineers, The Woodlands, Texas, USA, doi:10.2118/152530-ms.

Laubach, S. E. (1988), Subsurface fractures and their relationship to stress history in East Texas Basin Sandstone, *Tectonophysics*, *156*(1-2), 37-49, doi:10.1016/0040-1951(88)90281-8.

Laubach, S. E., P. Eichhubl, C. Hilgers, and R. H. Lander (2010), Structural diagenesis, *J. Struct. Geol.*, *32*(12), 1866-1872, doi:http://dx.doi.org/10.1016/j.jsg.2010.10.001.

Leonards, G. A., and R. J. Deschamps (1995), Origin and significance of the quasi-preconsolidation pressure in clay soils, in *Proceedings of International Symposium on Compression and Consolidation of Clayey Soils-IS-Hiroshima*, edited by H. Yoshikuni and O. Kusakabe, pp. 341-347, Aa Balkema, Hiroshima, Japan.

Leroueil, S. (1996), Compressibility of clays: fundamental and practical aspects, *Journal of geotechnical engineering*, *122*(7), 534-543.

Leroueil, S., M. Kabbaj, F. Tavenas, and R. Bouchard (1985), Stress-Strain Strain Rate Relation for the Compressibility of Sensitive Natural Clays, *Geotechnique*, *35*(2), 159-180.

Leroueil, S., and P. R. Vaughan (1990), The general and congruent effects of structure in natural soils and weak rocks, *Geotechnique*, *40*(3), 467-488.

Makowitz, A., and K. L. Milliken (2003), Quantification of brittle deformation in burial compaction, Frio and Mount Simon Formation sandstones, *J. Sediment. Res.*, *73*(6), 1007-1021, doi:10.1306/051003731007.

Marone, C., and C. Scholz (1989), Particle-size distribution and microstructures within simulated fault gouge, *J. Struct. Geol.*, *11*(7), 799-814.

McDaniel, R. R., and J. R. Willingham (1978), The effect of various proppants and proppant mixtures on fracture permeability, in *SPE Annual Fall Technical Conference and Exhibition*, edited, Society of Petroleum Engineers.

Menendez, B., W. L. Zhu, and T. F. Wong (1996), Micromechanics of brittle faulting and cataclastic flow in Berea sandstone, *J. Struct. Geol.*, *18*(1), 1-16.

Menetrey, P., and K. J. Willam (1995), Triaxial failure criterion for concrete and its generalization, *Aci Structural Journal*, *92*(3), 311-318.

Miller, A. D., G. R. Foulger, and B. R. Julian (1998), Non-double-couple earthquakes 2. Observations, *Rev. Geophys.*, *36*(4), 551-568, doi:10.1029/98rg00717.

Miller, L. D., C. C. Barton, R. S. Fredericksen, and J. R. Bressler (1992), Structural Evolution of the Alaska Juneau Lode Gold Deposit, Southeastern Alaska, *Can J Earth Sci*, *29*(5), 865-878.

Miller, L. D., R. J. Goldfarb, G. E. Gehrels, and L. W. Snee (1994), Genetic links among fluid cycling, vein formation, regional deformation, and plutonism in the Juneau Gold Belt, southeastern Alaska, *Geology*, *22*(3), 203-206.

Milliken, K. L., and S. E. Laubach (2000), *Brittle deformation in sandstone diagenesis as revealed by scanned cathodoluminescence imaging with application to characterization of fractured reservoirs*, 225-243 pp., Springer-Verlag Berlin, Berlin.

Milton-Tayler, D., C. Stephenson, and M. Asgian (1992), Factors affecting the stability of proppant in propped fractures: results of a laboratory study, in *SPE Annual Technical Conference and Exhibition*, edited, Society of Petroleum Engineers.

Mitchell, J. K., and K. Soga (1976), *Fundamentals of soil behavior*, Wiley New York.

Mortimer, N. (1993), Jurassic tectonic history of the Otago Schist, New-Zealand, *Tectonics*, *12*(1), 237-244.

Morton, R. A., J. C. Bernier, and J. A. Barras (2006), Evidence of regional subsidence and associated interior wetland loss induced by hydrocarbon production, Gulf Coast region, USA, *Environ. Geol.*, *50*(2), 261-274.

Mourgues, R., D. Bureau, L. Bodet, A. Gay, and J. Gressier (2012), Formation of conical fractures in sedimentary basins: Experiments involving pore fluids and implications for sandstone intrusion mechanisms, *Earth and Planetary Science Letters*, *313*, 67-78.

Mourgues, R., J. Gressier, L. Bodet, D. Bureau, and A. Gay (2011), "Basin scale" versus "localized" pore pressure/stress coupling–Implications for trap integrity evaluation, *Mar. Pet. Geol.*, *28*(5), 1111-1121.

Nairn, I., and J. Cole (1981), Basalt dikes in the 1886 Tarawera Rift, *New Zeal J Geol Geop*, *24*(5-6), 585-592.

Ng, T.-T., and R. Dobry (1994), Numerical simulations of monotonic and cyclic loading of granular soil, *Journal of Geotechnical Engineering*, *120*(2), 388-403.

Nguyen, S.-H., A. I. Chemenda, and J. Ambre (2011), Influence of the loading conditions on the mechanical response of granular materials as constrained from experimental tests on synthetic rock analoguematerial, *Int. J. Rock Mech. Min. Sci.*, *48*(1), 103-115, doi:http://dx.doi.org/10.1016/j.ijrmms.2010.09.010.

Obara, K. (2002), Nonvolcanic deep tremor associated with subduction in southwest Japan, *Science*, *296*(5573), 1679-1681.

Olsson, W. A., and D. J. Holcomb (2000), Compaction localization in porous rock, *Geophys. Res. Lett.*, *27*(21), 3537-3540.

Ottosen, N. S., and K. Runesson (1991), Discontinuous bifurcations in a nonassociated Mohr material, *Mech. Mater.*, *12*(3-4), 255-265, doi:10.1016/0167-6636(91)90022-r.

Paterson, C. J. (1986), Controls on gold and tungsten mineralization in metamorphic-hydrothermal systems, Otago, New Zealand, *Geological Society of Canada special paper*, *32*, 25-39.

Paterson, M. S., T.-f. Wong, M. S. Paterson, A. Geologist, M. S. Paterson, and A. Géologue (2005), *Experimental rock deformation: the brittle field*, Springer.

Pestana, J. M., and A. Whittle (1998), Time effects in the compression of sands, *Geotechnique*, *48*(5).

Petrie, E., J. Evans, and S. Bauer (2014), Failure of cap-rock seals as determined from mechanical stratigraphy, stress history, and tensile-failure analysis of exhumed analogs, *AAPG Bull.*, *98*(11), 2365-2389.

Pieri, M., L. Burlini, K. Kunze, I. Stretton, and D. L. Olgaard (2001), Rheological and microstructural evolution of Carrara marble with high shear strain: results from high temperature torsion experiments, *J. Struct. Geol.*, *23*(9), 1393-1413, doi:10.1016/s0191-8141(01)00006-2.

Pooladi-Darvish, M., and A. Firoozabadi (2000), Experiments and modelling of water injection in water-wet fractured porous media, *Journal of Canadian Petroleum Technology*, *39*(03), 31-42, doi:10.2118/00-03-02.

Ramm, M. (1992), Porosity-depth trends in reservoir sandstones: theoretical models related to Jurassic sandstones offshore Norway, *Mar. Pet. Geol.*, *9*(5), 553-567, doi:http://dx.doi.org/10.1016/0264-8172(92)90066-N.

Ramsey, J. M. (2003), Experimental study of the transition from brittle shear fractures to joins, Texas A&M University.

Ramsey, J. M., and F. M. Chester (2004), Hybrid fracture and the transition from extension fracture to shear fracture, *Nature*, *428*(6978), 63-66, doi:10.1038/nature02333.

Raysoni, N., and J. D. Weaver (2012), Selection of Proppants for Long-Term Stability, in *SPE Hydraulic Fracturing Technology Conference*, edited, Society of Petroleum Engineers, doi:10.2118/150668-MS.

Reches, Z. e., and J. Fink (1988), The mechanism of intrusion of the Inyo dike, Long Valley Caldera, California, *Journal of Geophysical Research: Solid Earth (1978–2012)*, *93*(B5), 4321-4334.

Roberts, J. E. (1964), Sand compression as a factor in oil field subsidence, Massachusetts Institute of Technology.

Rodriguez, E. (2005), A microstructural study of the extension-to-shear fracture rransition in Carrara marble, Texas A&M University.

Rudnicki, J. W. (2004), Shear and compaction band formation on an elliptic yield cap, *Journal of Geophysical Research: Solid Earth (1978–2012)*, *109*(B3).

Rudnicki, J. W. (2013), Failure of Rocks in the Laboratory and in the Earth, in *Mechanics Down Under*, edited, pp. 199-215, Springer.

Rudnicki, J. W., and J. R. Rice (1975), Conditions for the localization of deformation in pressure-sensitive dilatant materials, *Journal of the Mechanics and Physics of Solids*, *23*(6), 371-394, doi:http://dx.doi.org/10.1016/0022-5096(75)90001-0.

Rummel, F. (1987), Fracture mechanics approach to hydraulic fracturing stress measurements, in *Fracture mechanics of rock*, edited, pp. 217-239, Academic Press London.

Rutledge, J. T., W. S. Phillips, and M. J. Mayerhofer (2004), Faulting induced by forced fluid injection and fluid flow forced by faulting: An interpretation of hydraulic-fracture microseismicity, Carthage Cotton Valley gas field, Texas, *Bull. Seismol. Soc. Amer.*, *94*(5), 1817-1830, doi:10.1785/012003257.

Rutter, E. H., and P. H. Wanten (2000), Experimental study of the compaction of phyllosilicate-bearing sand at elevated temperature and with controlled porewater pressure, *J. Sediment. Res.*, *70*(1), 107-116, doi:Doi 10.1306/2dc40902-0e47-11d7-8643000102c1865d.

Schmoker, J. W., and D. L. Gautier (1988), Sandstone porosity as a function of thermal maturity, *Geology*, *16*(11), 1007-1010.

Schock, R. N., and H. Louis (1982), Strain behavior of a granite and a graywacke sandstone in tension, *Journal of Geophysical Research*, *87*(NB9), 7817-7823, doi:10.1029/JB087iB09p07817.

Shelly, D. R., G. C. Beroza, and S. Ide (2007), Non-volcanic tremor and low-frequency earthquake swarms, *Nature*, *446*(7133), 305-307, doi:10.1038/nature05666.

Shelly, D. R., and D. P. Hill (2011), Migrating swarms of brittle-failure earthquakes in the lower crust beneath Mammoth Mountain, California, *Geophys. Res. Lett.*, *38*, doi:10.1029/2011gl049336.

Shelly, D. R., D. P. Hill, F. Massin, J. Farrell, R. B. Smith, and T. a. Taira (2013a), A fluid-driven earthquake swarm on the margin of the Yellowstone caldera, *J. Geophys. Res.-Solid Earth*, *118*(9), 4872-4886, doi:10.1002/jgrb.50362.

Shelly, D. R., S. C. Moran, and W. A. Thelen (2013b), Evidence for fluid-triggered slip in the 2009 Mount Rainier, Washington earthquake swarm, *Geophys. Res. Lett.*, 1-7, doi:10.1002/grl.50354.

Sibson, R. H. (1986), Earthquakes and rock deformation in crustal fault zones, *Annual Review of Earth and Planetary Sciences*, *14*, 149.

Sibson, R. H. (1990), Conditions for fault-valve behavior, *Deformation Mechanisms, Rheology and Tectonics*, *54*, 15-28.

Sibson, R. H. (1996), Structural permeability of fluid-driven fault-fracture meshes, *J. Struct. Geol.*, *18*(8), 1031-1042, doi:10.1016/0191-8141(96)00032-6.

Sibson, R. H. (2004), Controls on maximum fluid overpressure defining conditions for mesozonal mineralisation, *J. Struct. Geol.*, *26*(6-7), 1127-1136, doi:10.1016/j.jsg.2003.11.003.

Sibson, R. H., and J. Scott (1998), Stress/fault controls on the containment and release of overpressured fluids: Examples from gold-quartz vein systems in Juneau, Alaska; Victoria, Australia and Otago, New Zealand, *Ore Geol. Rev.*, *13*(1-5), 293-306, doi:10.1016/s0169-1368(97)00023-1.

Sileny, J., D. P. Hill, L. Eisner, and F. H. Cornet (2009), Non-double-couple mechanisms of microearthquakes induced by hydraulic fracturing, *J. Geophys. Res.-Solid Earth*, *114*, doi:Artn B08307
Doi 10.1029/2008jb005987.

Spinler, E. A., D. R. Zornes, D. P. Tobola, and A. Moradi-Araghi (2000), Enhancement of oil recovery using a low concentration of surfactant to improve spontaneous and

forced imbibition in chalk, in *DOE Improved Oil Recovery Symposium*, edited, Society of Petroleum Engineers, Tulsa, Oklahoma, doi:10.2118/59290-MS.

Stöffler, D., D. Gault, J. Wedekind, and G. Polkowski (1975), Experimental hypervelocity impact into quartz sand: Distribution and shock metamorphism of ejecta, *Journal of Geophysical Research*, *80*(29), 4062-4077.

Syfan, F. E., and R. W. Anderson (2011), Lower Quality Natural Quartz Proppants Result In Significant Conductivity Loss and Reduction In Ultimate Recovery: A Case History, in *SPE Annual Technical Conference and Exhibition*, edited, Society of Petroleum Engineers.

Tada, R., and R. Siever (1989), Pressure solution during diagenesis, *Annual Review of Earth and Planetary Sciences*, *17*, 89.

Terzaghi, K., R. B. Peck, and G. Mesri (1996), *Soil mechanics in engineering practice*, John Wiley & Sons.

U.S.E.I.A. (2011), Review of emerging resources: U.S. shale gas and shale oil plays, edited by U. S. E. I. Administration, Washington, DC.

U.S.E.I.A. (2012), Annual energy outlook, edited by U. S. E. I. Administration.

Vajdova, V., P. Baud, and T.-f. Wong (2004), Compaction, dilatancy, and failure in porous carbonate rocks, *Journal of Geophysical Research: Solid Earth*, *109*(B5), B05204, doi:10.1029/2003JB002508.

van Noort, R., C. J. Spiers, and G. M. Pennock (2008), Compaction of granular quartz under hydrothermal conditions: Controlling mechanisms and grain boundary processes, *J. Geophys. Res.*, *113*(B12), B12206, doi:10.1029/2008jb005815.

Warpinski, N. R., R. C. Kramm, J. R. Heinze, and C. K. Waltman (2005), Comparison of Single- and Dual-Array Microseismic Mapping Techniques in the Barnett Shale, in *SPE Annual Technical Conference and Exhibition*, edited, Society of Petroleum Engineers, Dallas, Texas, doi:10.2118/95568-ms.

Warpinski, N. R., J. C. Lorenz, P. T. Branagan, F. R. Myal, and B. L. Gall (1993), Examination of a cored hydraulic fracture in a deep gas well, *SPE Production & Operations*(08), doi:10.2118/22876-pa.

Warpinski, N. R., and L. W. Teufel (1987), Influence of geologic discontinuities on hydraulic fracture propagation, *SPE Journal of Petroleum Technology*(02), doi:10.2118/13224-pa.

Wong, T. F., and P. Baud (2012), The brittle-ductile transition in porous rock: A review, *J. Struct. Geol.*, *44*, 25-53.

Wong, T. F., P. Baud, and E. Klein (2001), Localized failure modes in a compactant porous rock, *Geophys. Res. Lett.*, *28*(13), 2521-2524.

Wong, T. F., C. David, and W. L. Zhu (1997), The transition from brittle faulting to cataclastic flow in porous sandstones: Mechanical deformation, *J. Geophys. Res.-Solid Earth*, *102*(B2), 3009-3025.

Yamamuro, J. A., P. A. Bopp, and P. V. Lade (1996), One-dimensional compression of sands at high pressures, *Journal of Geotechnical Engineering*.

Yilmaz, E., A. Saglamer, and X. I. Xv Icsmge (2001), *Secondary and tertiary compression behavior of samsun soft blue clay*, 329-332 pp., A a Balkema Publishers, Leiden.

Zhang, J. X., T. F. Wong, and D. M. Davis (1990a), Micromechanics of pressure-induced grain crushin in porous rocks, *Journal of Geophysical Research-Solid Earth and Planets*, *95*(B1), 341-352.

Zhang, J. X., T. F. Wong, T. Yanagidani, and D. M. Davis (1990b), Pressure-induced microcracking and grain crushing in Berea and Boise sandstones - Acoustic emission and quantitative microscopy measurements, *Mech. Mater.*, *9*(1), 1-15.

Zoback, M. D. (2007), *Reservoir geomechanics*, xiii, 449 p. pp., Cambridge University Press, Cambridge.